FINAL REPORT ADDENDUM

Addendum to Final Report: Robust Statistics and Regularization for Feature Extraction and UXO Discrimination

SERDP Project MR-1629

MAY 2013

Laurens Beran
Lin-Ping Song
Stephen Billings
Barry Zelt
Black Tusk Geophysics Inc.

Doug Oldenburg
The University of British Columbia

This document has been cleared for public release

SERDP
DOD ▪ EPA ▪ DOE

This report was prepared under contract to the Department of Defense Strategic Environmental Research and Development Program (SERDP). The publication of this report does not indicate endorsement by the Department of Defense, nor should the contents be construed as reflecting the official policy or position of the Department of Defense. Reference herein to any specific commercial product, process, or service by trade name, trademark, manufacturer, or otherwise, does not necessarily constitute or imply its endorsement, recommendation, or favoring by the Department of Defense.

Executive Summary

This report presents research carried out under follow-on funding for SERDP project MR-1629, *"Robust Statistics and Regularization for Feature Extraction and UXO Discrimination."* We report on the following research areas:

(1) *Improving location estimation with SVD.* We have developed an inversion algorithm, termed a Temporal Orthogonal Projection Inversion (TOPI), that uses singular value decomposition (SVD) to project the data onto a subset of singular vectors. This automates channel selection for target location estimation and produces improved polarizability estimates.

(2) *Building the training data and combining different feature sets in classification.* In a published article (Beran et al., 2012), we describe our approach to generating a training data set and identifying novel TOI. Using ESTCP demonstration data sets, we show how the variable quality of estimated features affects overall classification performance. Finally, we demonstrate a technique to optimize classification performance by adapting features during target prioritization. Additional unpublished work included in this report describes a "Combined Classifier Ranking" (CCR) that simultaneously uses all available features to generate an ordered diglist.

(3) *Regularized inversion.* Improved polarizability estimates can be obtained by augmenting the data misfit with a model norm that penalizes deviations from desired model properties. Previous work looked at penalizing differences in secondary polarizabilities, here we consider a model norm that favors "smooth" (i.e monotonically decreasing) polarizability estimates. This approach significantly improves the match of recovered and reference polarizabilities for low SNR data (e.g. deep targets). We have also investigated regularized inversion for dipole location estimation. An underdetermined implementation with a sparse, L1 norm requires additional weighting to constrain model space. Better results are obtained with an overdetermined formulation that removes redundant sources by penalizing the total distance between sources.

(4) *Technology transfer.* We have written a paper providing a basic introduction to the current state of UXO detection and classification. The intended audience is the humanitarian demining and UXO community and the paper was published in the Spring 2013 issue of the Journal of Explosive Remnants of War (ERW) and Mine Action.

Acknowledgements

This work was funded by the Strategic Environmental Research and Development Program (SERDP). Data examples from Bellows Air Force Station, HI are used with permission from Mr. Rick Grabowski, U.S. Army Corps of Engineers.

Contents

Executive Summary 2
Acknowledgements 3
List of Figures 5
List of Acronyms 6
1. Introduction 7
2. Development and application of multi-feature classification methods 8
3. Regularized inversion methods for dipole parameter estimation 13
4. Regularized location estimation 21
4.1. Underdetermined location estimation 21
4.2. Overdetermined location estimation 28
5. Conclusions and recommendations for future research 33
References 34
Appendix A. Published articles 35
A.1. Temporal Orthogonal Projection Inversion Technique for EMI Sensing of UXO 35
A.2. Detecting and classifying UXO 60
A.3. Practical strategies for classification of unexploded ordnance 67

List of Figures

1 MMR size-decay feature space 9

2 Receiver operating characteristic for submitted multi-stage classifier applied to MMR data 9

3 Polarizabilities for CE-2281 (155mm at 80 cm depth) 10

4 Size-decay feature space plot showing location of recovered models for CE-2281 10

5 Receiver operating characteristic for retrospective CCR applied to MMR data 11

6 Receiver operating characteristic for classifiers applied retrospectively to Spencer MetalMapper data 12

7 Cooper Bomb No Fins at 3 feet 16

8 Cooper Bomb With Fins at 3 feet 16

9 Cooper Bomb No Fins at 4 feet 17

10 Cooper Bomb With Fins at 4 feet 17

11 Comparison of raw polarizabilities with polarizabilities estimated by fitting a sum of exponentials, and regularization for smoothness 18

12 QCZilla plot for Cooper Bomb No Fins at 4 feet 19

13 QCZilla plot for Cooper Bomb No Fins at 4 feet 20

14 Example two-object inversion results for a cued MetalMapper sounding 22

15 Source locations for underdetermined inversion of MetalMapper data 23

16 Regularized source localization with an L2 norm 23

17 Decay of forward modeling matrix G as a function of source depth 24

18 Effect of model weighting on sparse inversion 26

19 Two-object sparse underdetermined inversion example 27

20 Two-object overdetermined inversion example 28

21 Computation of the total distance between sources 29

22 Flowchart for overdetermined inversion with distance regularization 29

23 Comparison of execution times for single and multi-source implementations of forward modelling matrix **G** 30

24 Location estimation with distance regularization 31

25 Comparison of error in estimated locations for inversion of synthetic data sets with unregularized and regularized algorithms 32

List of Acronyms

CCR	Combined Classifier Ranking
cm	centimeter
EM	Electromagnetic
EMI	Electromagnetic induction
ESTCP	Environmental Security Technology Certification Program
m	meter
mm	millimeter
MMR	Massachusetts Military Reservation
MR	Munitions Response
ms	millisececond
mV	milliVolt
ROC	Receiver Operating Characteristic
SERDP	Strategic Environmental Research and Development Program
SVD	Singular Value Decomposition
SVM	Support Vector Machine
TEM	Time-domain electromagnetic
TEMTADS	Time Domain Electromagnetic Towed Array Detection System
TOI	Target of Interest
TOPI	Temporal Orthogonal Projection Inversion
UBC-GIF	University of British Columbia Geophysical Inversion Facility
UXO	Unexploded Ordnance

1. Introduction

Under SERDP MR-1629, *"Robust Statistics and Regularization for Feature Extraction and UXO Discrimination,"* we have investigated a number of techniques for improving inversion and discrimination. Methods for UXO discrimination using magnetic and electromagnetic induction data generally rely on feature vectors extracted from physics based dipole models. These feature vectors are obtained by solving an inverse problem that provides a best-fit to the observed data. Typically, this best-fit is defined as the model that minimizes the sum-of-squares of the residuals between observed and predicted data,with each residual weighted by an estimated standard deviation. Thus, there is an implicit assumption that the residuals are normally distributed (Gaussian) and that the maximum likelihood solution is the most appropriate model to extract from the data. This assumption of Gaussian statistics may not be appropriate if the residuals have outliers (due to sensor or positional glitches) or if the residuals contain significant structure (model not adequate to represent the data). In those cases, the predicted feature vectors may be significantly in error and should not be relied upon for discrimination. In addition, the maximum likelihood solution may not be the most appropriate one to recover from the available data. In the first part of the MR-1629 project we researched the statistical structure of the underlying inversion process developed methods for more accurate extraction of feature vectors from multi-time, multi-frequency and multi-component EMI data (Billings et al., 2011).

In follow-on work we proposed to investigate a number of UXO data processing problems deserving of further research. In this report, we first provide detailed descriptions of unpublished follow-on work on combining different features in classification and regularized inversion. Published articles, comprising the bulk of our follow-on work under MR-1629, are included in an appendix:

(1) L. P. Song, D. W. Oldenburg, L. R. Pasion, S. D. Billings, and L. S. Beran (2013). Temporal Orthogonal Projection Inversion Technique for EMI Sensing of UXO. IEEE Transactions on Geoscience and Remote Sensing, in preparation.
(2) L. S. Beran, B. C. Zelt, S. D. Billings (2013). Detecting and classifying UXO. Journal of Explosive Remnants of War and Mine Action, 17.1, pp. 57-62.
(3) L. S. Beran, B. C. Zelt, L. R Pasion, S. D. Billings, K. A. Kingdon, N. Lhomme, L. Song, D. W. Oldenburg (2012). Practical strategies for classification of unexploded ordnance. Geophysics, 78, pp. E41 − E46.

We conclude with a brief discussion of remaining problems to be addressed with further research.

2. Development and application of multi-feature classification methods

In a previous article (Beran et al. (2012), see appendix A.3), we advocated a classification approach that progressively reduces the dimensionality of the feature space as we proceed from high to low SNR targets in a diglist. With this method we begin our ranking with obvious TOI for which all polarizabilities are a good match to known reference polarizabilities. We then revert to using primary (or total) polarizabilities to classify items that are potential TOI with poorly constrained secondary polarizabilities. The switch between these feature sets can be defined manually by the analyst. We also proposed an automated switch based on choosing the "elbow" of the sorted decision statistic.

Here we investigate the feasibility of classification using all available feature sets simultaneously. For each target we produce a discrete ranking R_i in the diglist using the following feature sets:

(1) All polarizabilities,
(2) Primary polarizabilities,
(3) Size,
(4) Decay

For example, $R_1 = 1$ indicates that our target is ranked first in the diglist generated by matching with all polarizabilities. Here we use the convention that the diglist is ordered with likely-TOI first. We then obtain an overall ranking R_{tot} for a target by summing over the individual ranks from all feature sets

$$R_{tot} = \sum_i R_i. \tag{1}$$

Sorting the total rankings in ascending order produces a merged diglist that uses all feature sets simultaneously to classify each target. In this report we term this classification algorithm a "Combined Classifier Ranking" (CCR). To demonstrate CCR performance, we consider a number of real data sets acquired under the ESTCP demonstration program. Figure 1 shows a size-decay feature space extracted from MetalMapper data acquired at Massachusetts Military Reservation in 2012.

Our submitted diglist (figure 2) used a four-stage approach and resulted in five false negatives. For the early digs (1-183) the order was based on a weighted combination of polarizability misfit (relative to the best fitting item in the reference library) using all three polarizabilities, as well as size and decay. Optimal weights were chosen such that items flagged as likely UXO would appear as early as possible in the dig list. The second stage (184-223) was based on polarizability misfit alone (using all three polarizabilities). The third stage (224-359) was based on polarizability misfit using only the primary polarizability. The final stage (360-881) was based on decay.

The false negatives in this case are all TOI for which the recovered features deviate significantly from the expected reference polarizabilities.

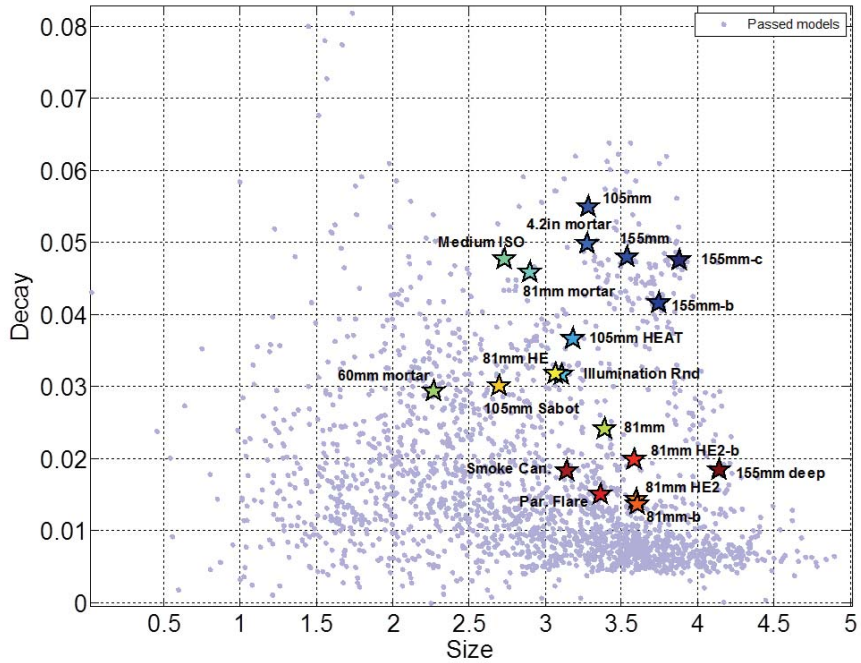

FIGURE 1. Distribution of passed models for MMR data displayed in decay(t1,t29) versus size(t1) feature space, where size(t1) is the total polarizability measured at the first time channel (t1=0.106ms), and decay(t1,t29) is size(t1)/size(t29) where t29=2.006ms. Outliers are not shown. Labelled stars represent ordnance library reference items.

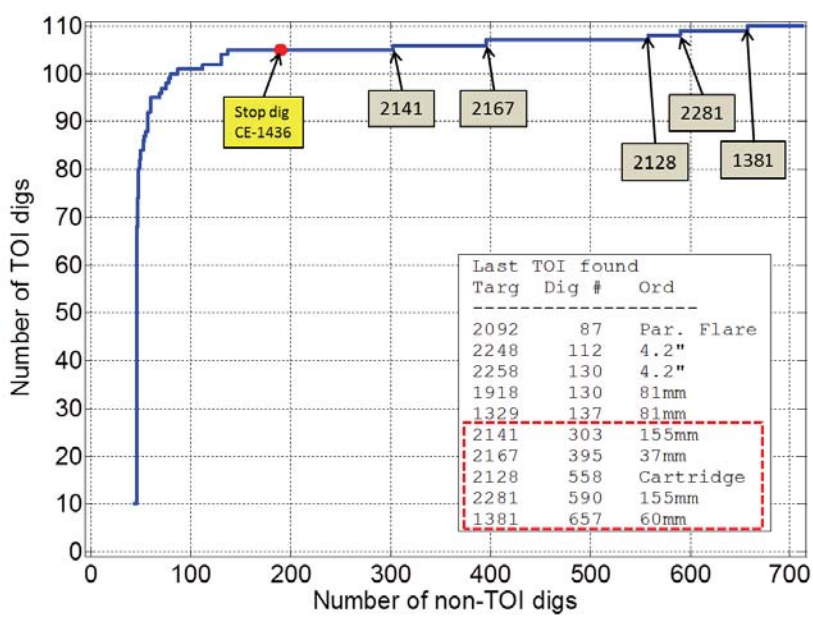

FIGURE 2. Receiver operating characteristic for submitted multi-stage classifier applied to MMR data.

For example, figure 3 shows the polarizabilities estimated via single, two, and three object inversions for target 2281, a 155mm at 80 cm depth. All models have polarizabilities that are

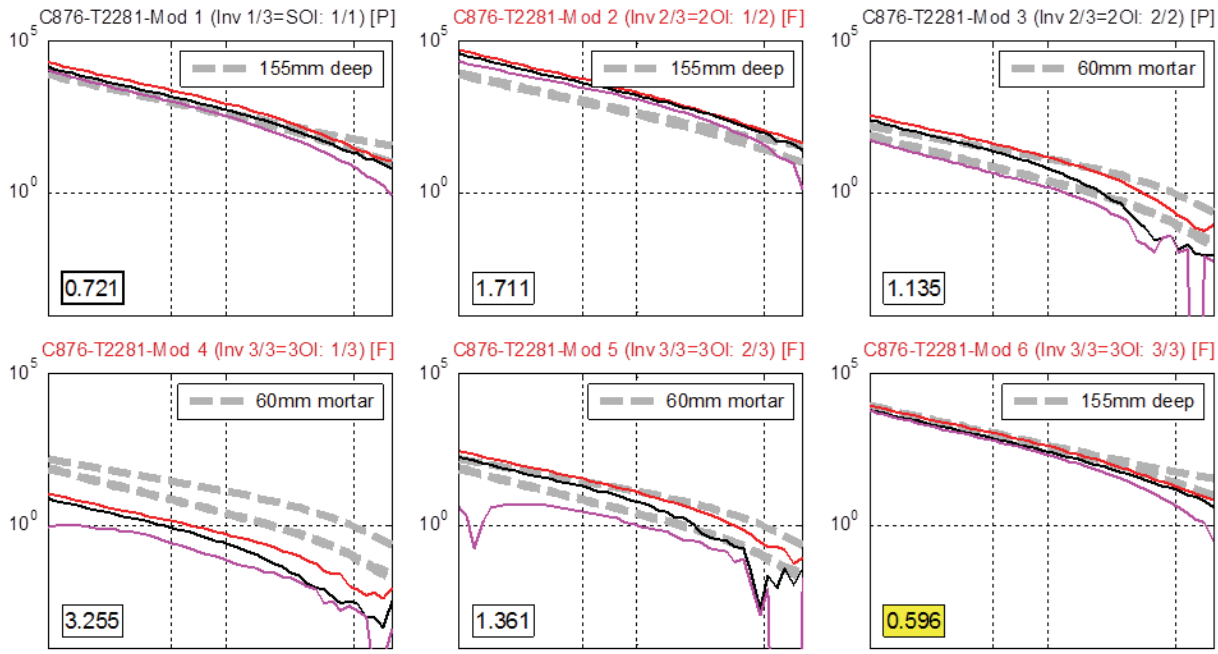

FIGURE 3. (Polarizabilities for CE-2281 (155mm at 80 cm depth). Predicted polarizabilities are red, black and magenta lines. Broken grey lines are polarizabilities for best fitting reference item. Top left: single object inversion. Top center and right: 2-object inversion. Bottom row: 3-object inversion

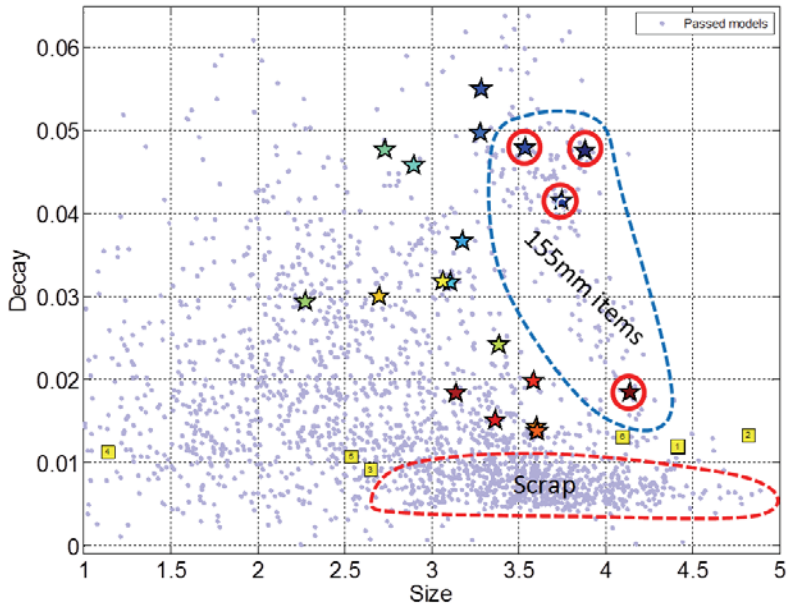

FIGURE 4. Decay-size feature space plot showing location of recovered models for CE-2281 (numbered yellow squares) in relation to passed models of all other anomalies (blue dots). Stars are reference features. Red circles are variations of the 155mm projectile. The broken blue line outlines the region occupied by most 155mm objects. The broken red line outlines a dense region of large-amplitude, fast-decaying scrap items.

far outside the expected range for this target class, this can also be visualized in size-decay space (figure 4). We therefore do not expect any automated classifier - including CCR - to identify the false negatives in a retrospective analysis.

We retrospectively applied the CCR to the same MMR feature data and obtained the ROC displayed in figure 5. Excluding the 5 outlying TOI, the CCR provides better initial performance ($\sim$ 75 false alarms for all TOI) than our submitted dig list ($\sim$ 130 false alarms for all TOI). In particular, the CCR ROC does not have the gradual turnover, or elbow, that we usually see for multi-stage classifiers when we switch from using all polarizabilities to total polarizabilities (e.g. between approximately 75 and 125 non-TOI digs in figure 2). Both diglists fail to find the same 5 outliers at the selected stop dig point.

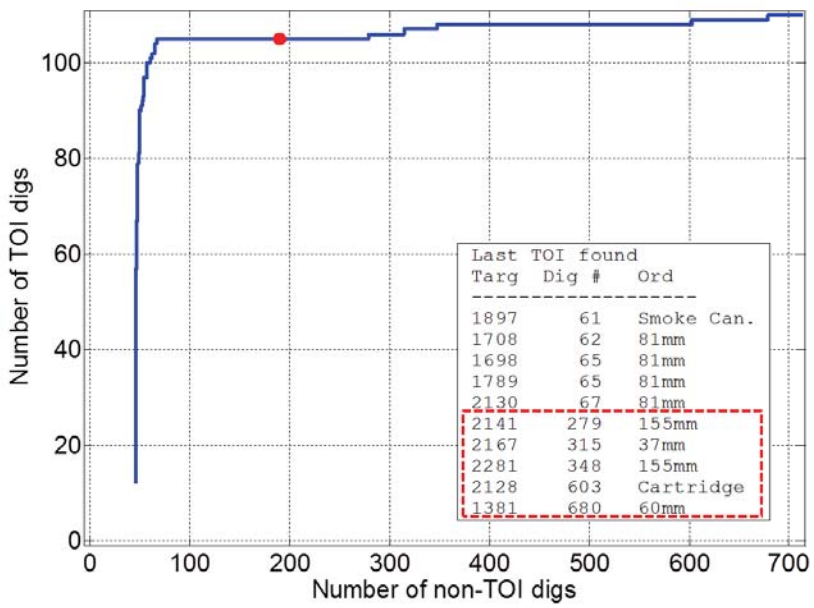

FIGURE 5. Receiver operating characteristic for retrospective CCR applied to MMR data.

Figure 6 illustrates a second example of CCR performance, in this case applied to MetalMapper data from the 2012 Spencer Range demonstration. The CCR achieves a lower false alarm rate than single stage classifiers using L1 or L123 misfit. It also outperforms our automated two stage approach, described in appendix A.3.

These initial results suggest that the CCR can produce diglists with similar, or slightly better, performance than the multi-stage approach. We have implemented the CCR in our *DigZilla* classification software and have also proposed an ESTCP project to make our classification methods accessible through UX-Analyze.

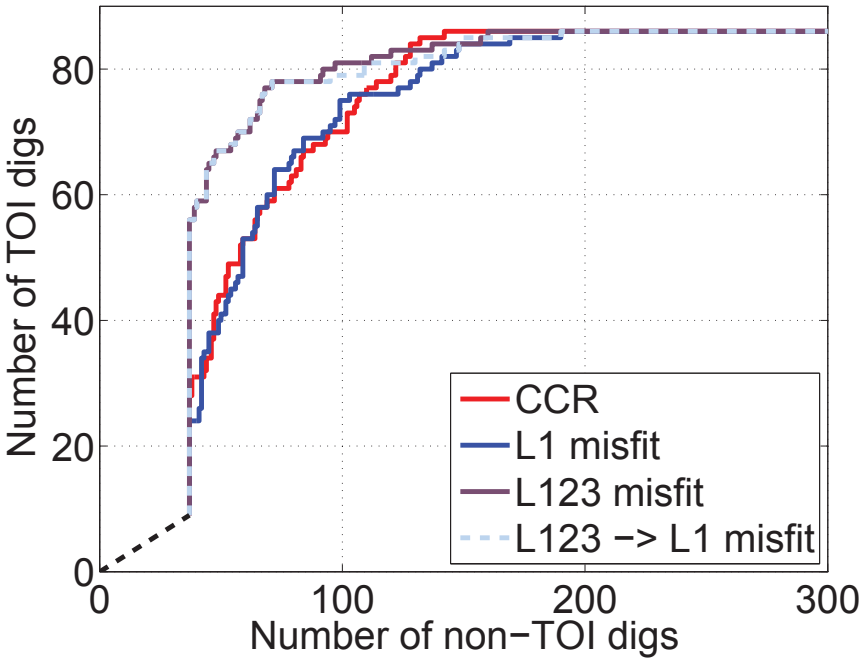

FIGURE 6. Receiver operating characteristic for classifiers applied retrospectively to Spencer MetalMapper data. The combined classifier ranking (CCR) is compared with rankings based solely on polarizability misfits with respect to reference L1 polarizabilities (denoted L1 misfit) and all (L1, L2, L3) reference polarizabilities (denoted L123 misfit). We also consider a two-stage approach that switches from L123 misfit to L1 misfit using an automated criterion (see appendix A.3).

3. Regularized inversion methods for dipole parameter estimation

In earlier work conducted under this project we investigated a number of different regularisation methods with application to inversion of TEM data with the dipole model. In Beran et al. (2012), we focused on regularizing the transverse, or secondary, polarizabilities. Equality of transverse polarizabilities is diagnostic of an axisymmetric body of revolution and so has been proposed as a useful feature to discriminate between axisymmetric UXO and non-axisymmetric metallic clutter. We showed that estimated transverse polarizabilities can sometimes be poorly constrained in an inversion of multi-static TEM data. This motivated our development of a regularized inversion algorithm that penalizes the deviation between transverse polarizabilities. We then developed an extension of the support vector machine (SVM) classifier that uses all models obtained via regularized inversion to make discrimination decisions. This approach achieved the best performance of all candidate discrimination algorithms applied to a number of real data sets.

In this section, we investigate how regularization can be used to mitigate the jitter (noise) in polarizabilities estimated from low SNR data. Our development is motivated by practical experience with a large scale MetalMapper survey conducted at the Bellows Air Force Station on Oahu, Hawaii in 2012-2013. The principal concern at the site was the removal of potentially hazardous Cooper bombs down to a maximum clearance depth of four feet.

To determine if Cooper bombs could be reliably classified down to a four foot depth range, MetalMapper data were collected at various standoffs over an inert Cooper bomb, both with and without fins. The left columns of figures 7 to 10 show polarizabilities extracted over Cooper bombs with and without fins at 3 and 4 feet below the sensor, respectively. Each figure contains results from three orthogonal target orientations: horizontal east and north, and vertical. For the Cooper bombs at 3 feet, the recovered polarizabilities are relatively smooth, although there are a number of channels where noise causes some distortion in the expected values, particularly for the secondary polarizabilities. The MetalMapper data for the Cooper bombs at 4 feet are significantly lower SNR and the recovered polarizabilities are extremely noisy. While the polarizabilities at each channel do tend to vary about the expected values, it is difficult to unambiguously identify each item as a Cooper bomb.

The standard inversion algorithm implemented in UXOLab splits the inverse problem into a nonlinear step for target location estimation and a linear step, at a fixed location, for recovery of the polarisability matrix. The six unique elements of the polarisability matrix are recovered independently one time-channel at a time. The polarizability estimates are only linked during a final joint diagonalization process which solves for the best fitting set of principal axis polarizabilities and orientations applicable to all time-channels. For low SNR anomalies (such as the 4 ft deep Cooper bombs) the recovered polarizabilities tend to be quite noisy (non-monotonic) because there is no explicit functional dependence between the values recovered at adjacent time-channels.

There are a number of possible approaches that could be pursued to ensure that the recovered polarizabilities are smooth, including:

(1) Parameterize the polarizability decay (e.g. by using the Pasion-Oldenburg parameters) and directly solve for those parameters during the inversion process;
(2) Smooth the recovered polarizabilities after an inversion, either by a moving average or by fitting a smooth function (e.g. a sum of exponentials);
(3) Impose a smoothness constraint on the recovered polarizabilities through regularisation.

Here we proceed using this last method. When solving parametric inverse problems, it is often sufficient to minimize a data norm quantifying the misfit between observed and predicted data

$$\phi_d = \|\mathbf{W}_d(\mathbf{d}^{obs} - \mathbf{d}^{pred})\|^2 \tag{2}$$

with $\mathbf{d}^{pred} = F(\mathbf{m})$ generally a nonlinear functional of the model $\mathbf{m}$, and $\mathbf{W}_d$ a weighting matrix accounting for estimated errors on the data. Assuming Gaussian errors on the observed data, minimization of equation 2 yields a maximum likelihood estimate of the model parameters (Menke, 1989). Additional prior information can be incorporated in the inversion via parameter bounds (e.g. positivity) or by constructing a model which has specified properties. In the latter case, the optimization problem can be solved by minimizing the norm (Oldenburg and Li, 2005)

$$\min \phi = \phi_d + \beta\phi_m \tag{3}$$

where the regularization parameter β controls the trade-off between data and model norms. The model norm ϕ_m is a regularizer that ensures that the recovered model has, for example, a minimum deviation from some prior reference model. In this work our regulariser is instead a smoothness constraint: we use a five point finite difference approximation to the second-derivative as ϕ_m. The smoothness constraint is applied to each of the six components of the non-diagonalized polarisation tensor matrix. We weight the smoothness constraint as $\sqrt{t_n}$, where t_n is the centre of the n-th time-channel: this has the effect of increasing the weighting given to the latter time-channels where the polarizabilities are much smaller than at early time. White noise that is log-gated decreases as $\frac{1}{t}$ and hence for the data we use a weight matrix that is proportional to t. For a linear forward modelling ($\mathbf{d}^{pred} = \mathbf{Gm}$) with fixed β, equation 5 is minimized by the solution of (Oldenburg and Li, 2005)

$$\left(\mathbf{G}^T\mathbf{W}_d^T\mathbf{W}_d\mathbf{G} + \beta\mathbf{W}_m^T\mathbf{W}_m\right)\mathbf{m} = \mathbf{G}^T\mathbf{W}_d^T\mathbf{W}_d\mathbf{d}^{obs}. \tag{4}$$

Here $\mathbf{W}_d$ and $\mathbf{W}_m$ are weighting matrices on the data and model, respectively. The regularisation parameter β can be chosen using a number of automated methods such as the L-curve method or Generalized Cross Validation, or alternatively can be set to achieve a target misfit dictated by the estimated noise (Farquharson and Oldenburg, 2004). For this application we found that the there was a wide range of parameter settings that produced

a relatively stable solution, and we settled on a single value of $\beta = 0.2$ for all the examples shown in this section. The right columns of figures 7 to 10 show polarizabilities extracted using this regularisation parameter over Cooper bombs with and without fins at 3 and 4 feet below the sensor. The polarizabilities are much smoother than the unregularized inversion and in all twelve cases the item is clearly revealed to be a Cooper bomb.

The advantage of regularized inversion over alternative methods of polarizability smoothing is illustrated in figure 11. We compare the regularized result with a fit to the raw polarizabilities using a sum of decaying exponentials. The latter approach does a decent job at denoising, but the secondary and tertiary smoothed polarizabilities can be strongly skewed when fitting late time raw polarizabilities. In all cases in figure 11 the regularized approach gives a lower misfit with respect to the reference polarizabilities than smoothing with an exponential fit.

Figures 12 and 13 compare unregularized and regularized inversions, respectively, for the case of an X-directed Cooper bomb with no fins at 4 feet. Close inspection of the observed versus fitted data reveals that the regularised inversion does not fit many of the spikes in the observed data indicating that the unregularized inversion overfits the data (i.e. the model converged to fit both the signal and noise in the observed data). In this respect, regularization is similar to robust inversion: both approaches diminish the effect of noisy data on the recovered model.

We also note in figure 13 that the regularised inversion did not produce a good fit to the RxY-TxX or RxX-TxY receiver-transmitter combinations indicating that those values can't easily be reproduced with a smooth polarisation tensor model. This tendency occurred for each of the other 11 examples of Cooper Bomb polarizabilities shown and presumably indicates systematic error in those receiver-transmitter combinations (e.g. inappropriate background estimate, systematic modeling error, etc).

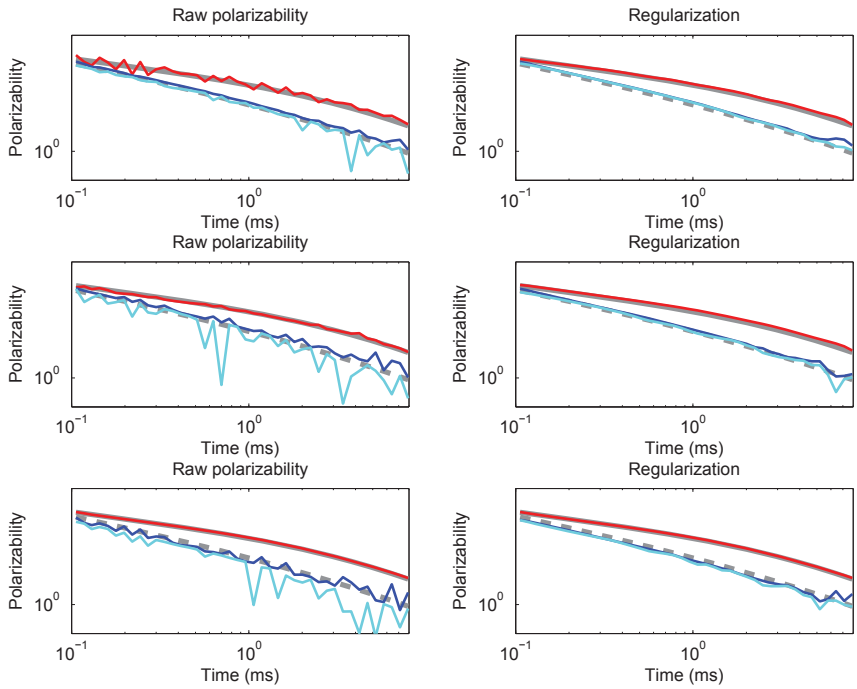

FIGURE 7. Polarizabilities extracted with no-regularisation (left column) and with regularisation (right column) for a Cooper bomb without fins 3 feet from the sensor and oriented along X (top row), Y(middle row) and Z (bottom row). The polarisability (obtained from high quality data) of a Cooper bomb without fins is show in grey.

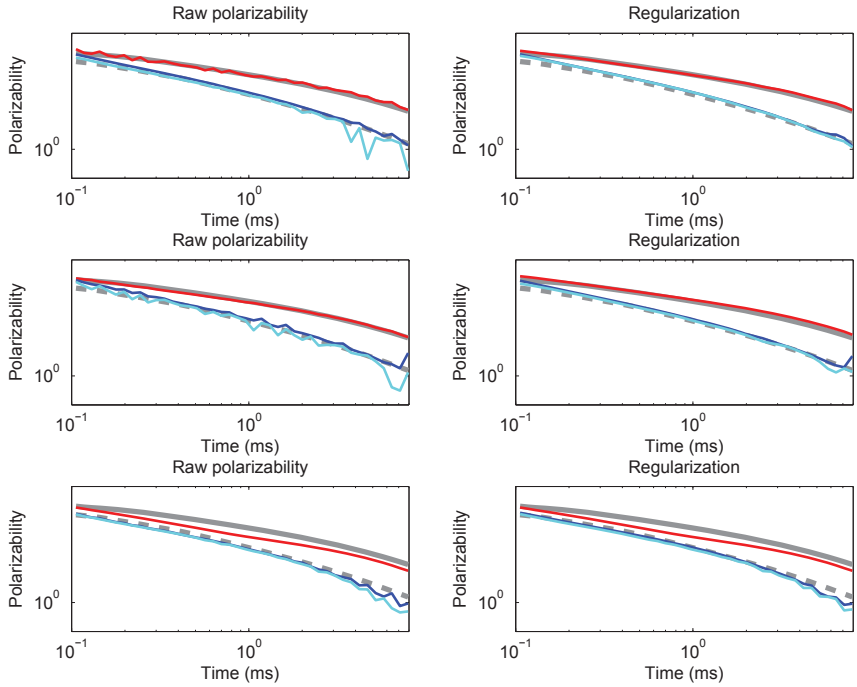

FIGURE 8. Polarizabilities extracted with no-regularisation (left column) and with regularisation (right column) for a Cooper bomb with fins 3 feet from the sensor and oriented along X (top row), Y(middle row) and Z (bottom row). The polarisability (obtained from high quality data) of a Cooper bomb with fins is show in grey.

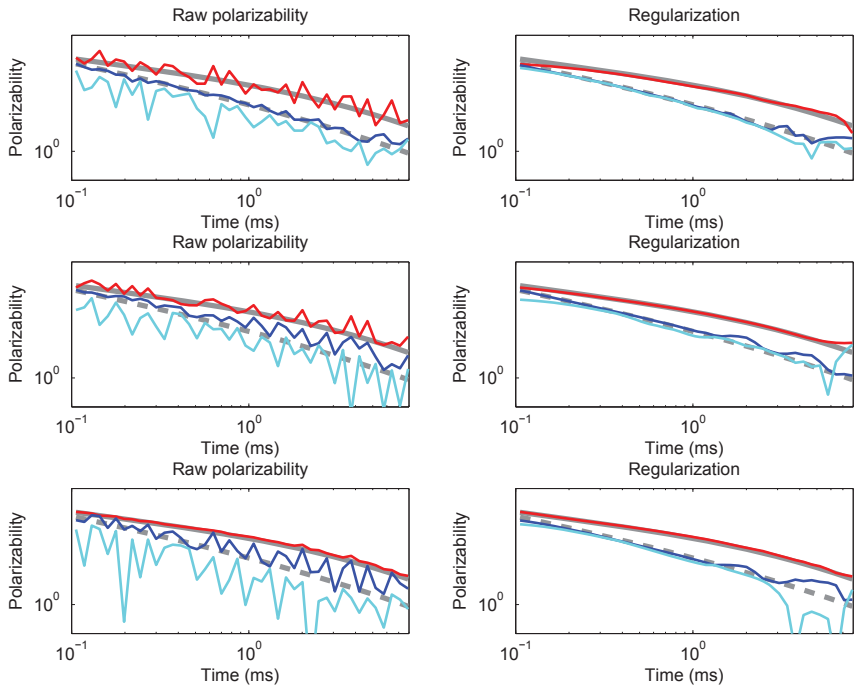

FIGURE 9. Polarizabilities extracted with no-regularisation (left column) and with regularisation (right column) for a Cooper bomb without fins 4 feet from the sensor and oriented along X (top row), Y(middle row) and Z (bottom row). The polarisability (obtained from high quality data) of a Cooper bomb without fins is show in grey.

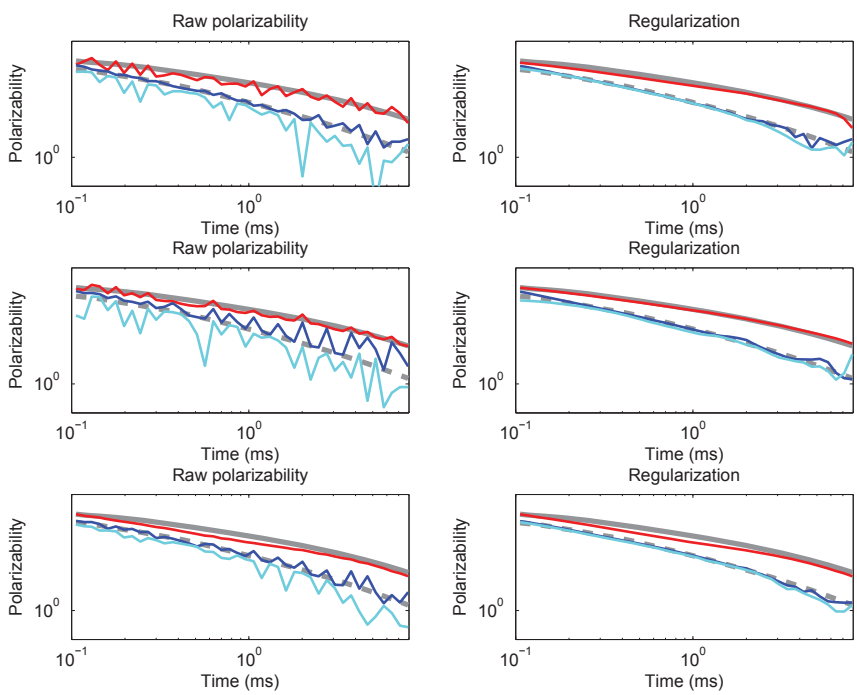

FIGURE 10. Polarizabilities extracted with no-regularisation (left column) and with regularisation (right column) for a Cooper bomb with fins 4 feet from the sensor and oriented along X (top row), Y(middle row) and Z (bottom row). The polarisability (obtained from high quality data) of a Cooper bomb with fins is show in grey.

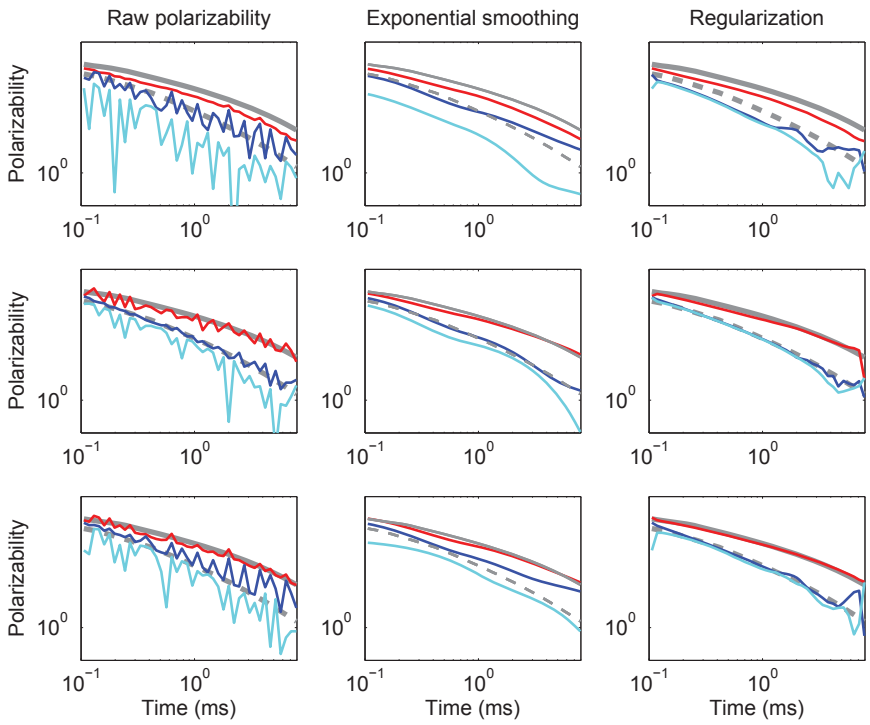

FIGURE 11. Comparison of raw polarizabilities (left) with polarizabilities estimated by fitting a sum of exponentials (middle), and regularization for smoothness (right).

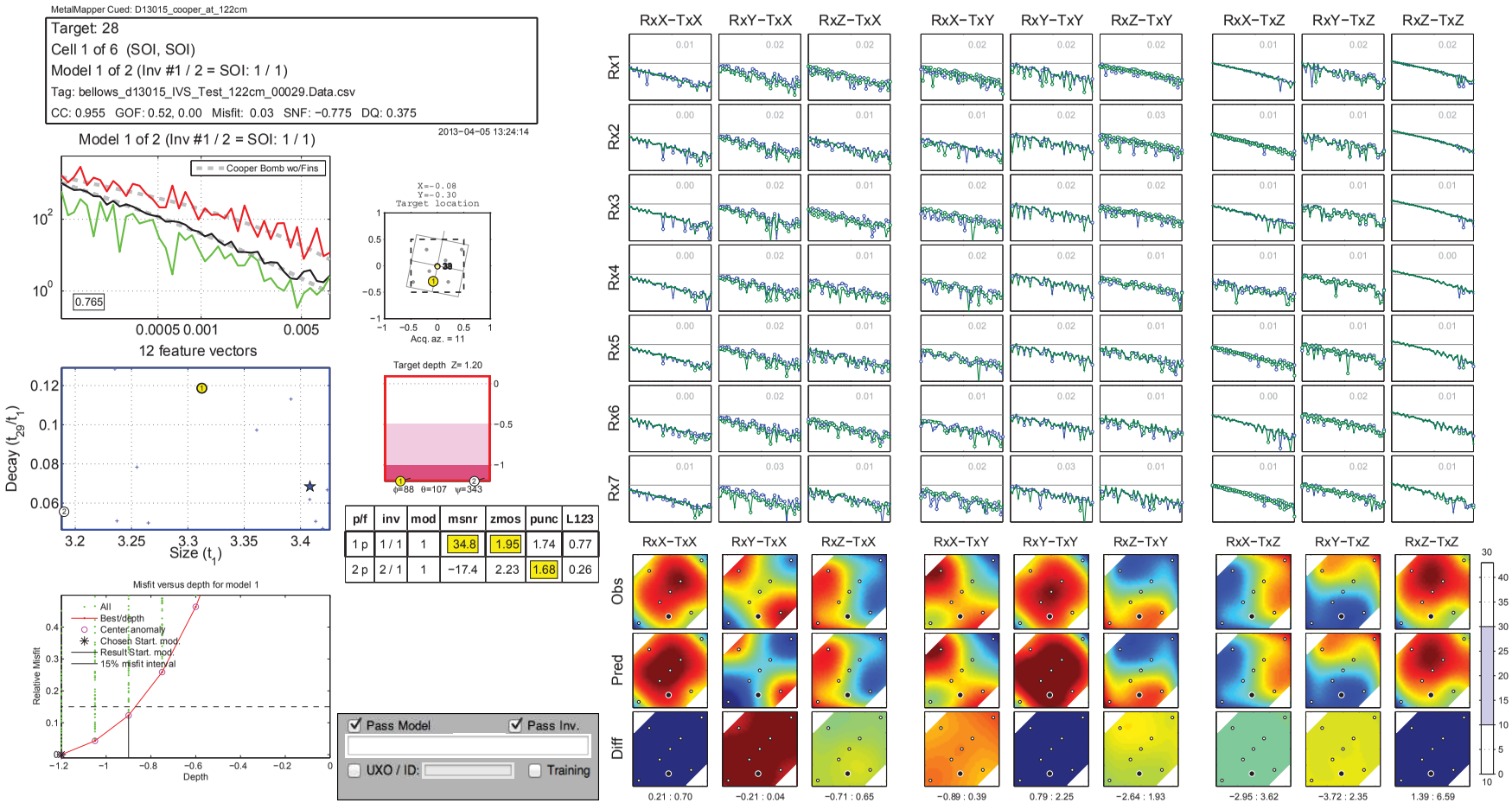

p/f	inv	mod	msnr	zmos	punc	L123
1 p	1 / 1	1	34.8	1.95	1.74	0.77
2 p	2 / 1	1	−17.4	2.23	1.68	0.26

FIGURE 12. QC tool output for unregularized inversion for the X-directed Cooper Bomb with no fins at 4 foot depth.

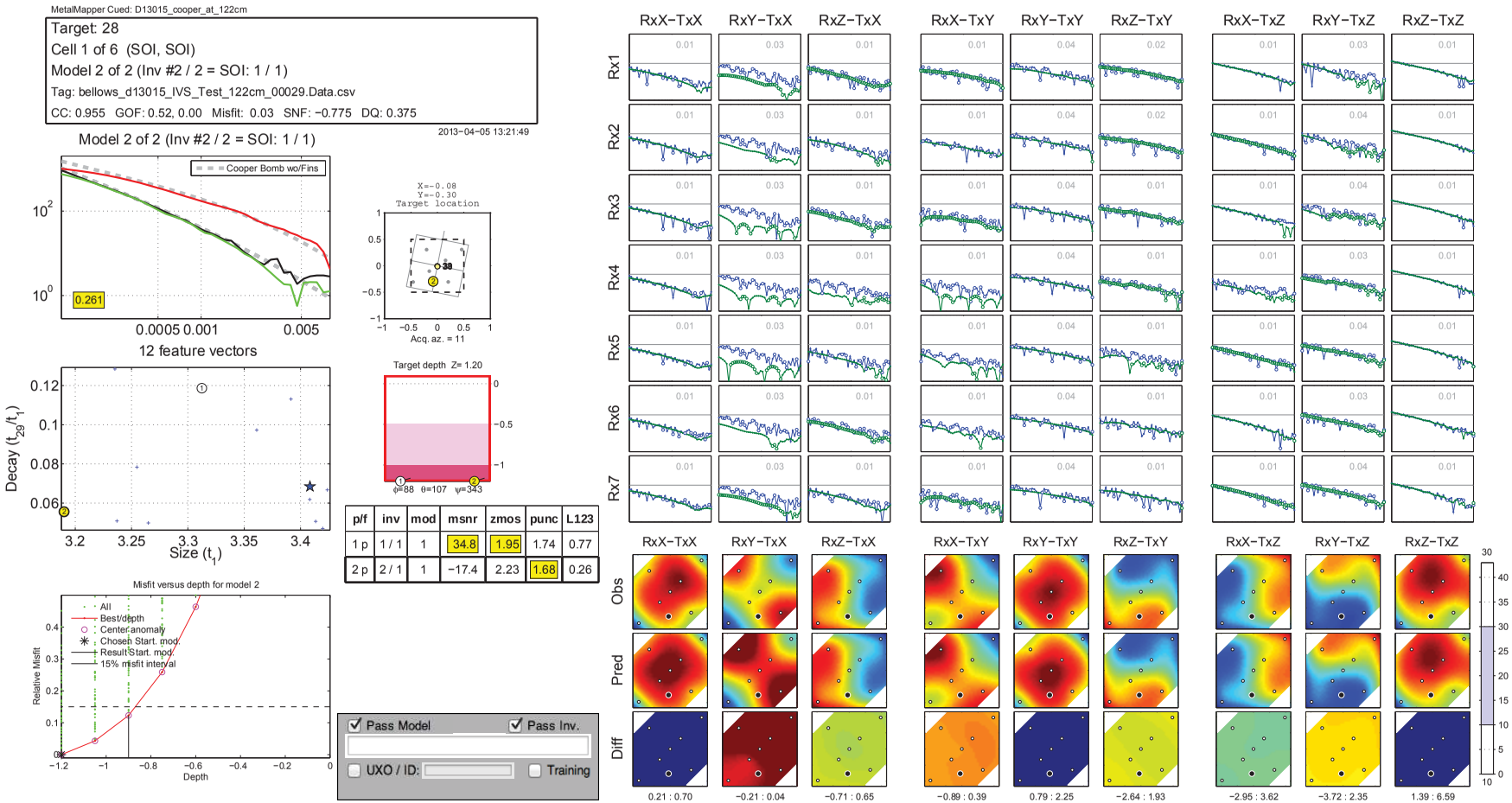

p/f	inv	mod	msnr	zmos	punc	L123
1 p	1 / 1	1	34.8	1.95	1.74	0.77
2 p	2 / 1	1	−17.4	2.23	1.68	0.26

FIGURE 13. QC tool output for regularised inversion of the X-directed Cooper Bomb with no fins at 4 foot depth.

4. Regularized location estimation

4.1. **Underdetermined location estimation.** Accurate recovery of target location is crucial to the success of UXO classification. This is because dipole polarizabilities are strongly correlated with estimated distance to the sensor, so that a small error in location can translate to a large error in the amplitude of polarizability estimates (Beran et al., 2011). These correlated errors will reduce the match with respect to reference polarizabilities and hence adversely affect classification performance. Perhaps the principal benefit of modern, multi-static TEM sensors has been improved target localization; it is this capability that has driven recent advances in classification performance.

Improved data has produced a commensurate improvement in inversion algorithms, and multi-source solvers are now routinely used to process field EMI data. Song et al. (2011) first estimate the location of N hypothesized dipole sources, followed by estimation of polarizabilities and orientations at fixed locations. Separating the problem in this way produces a linear inverse problem at the second step, and eliminates the problematic location/amplitude correlation that arises when all parameters are recovered simultaneously. However, the location estimation step is still nonlinear, owing to the approximate $1/r^6$ decay of the predicted fields. Some care must be taken with initializing the location search to avoid convergence to suboptimal local minima. Song addresses this by defining a regular grid of candidate locations and testing solutions on this grid. For even a two-source problem, an exhaustive search of all combinations is prohibitively expensive, and so a reduced set of randomized candidate locations are tested. This approach to multi-source inversion is now used in all BTG data processing. The results have been generally excellent, but we do note that in rare cases the algorithm does not produce repeatable results because of the random start model search (figure 14).

Miller et al. (2010) formulate dipole location estimation as a regularized inverse problem. As in Song et al. (2011), they define a regular grid of source locations. However, rather than assuming a pre-defined number of sources, they fit the observed data with *all* sources. The inverse problem in this formulation may be underdetermined, and so additional information must be incorporated in the form of model regularization. A sparse, L1 type norm that forces most source amplitudes to zero is appropriate. Miller's implementation with a sparse solver has been successfully demonstrated on real data sets. Since their method does not depend on randomized start models, convergence to local minima - as illustrated in figure 14 - may be avoided.

Here we pursue a direct comparison of overdetermined and sparse underdetermined approaches to multi-source dipole location estimation. To better understand the problem, we have developed our own implementations of underdetermined methods. In future work (e.g. SERDP MR-2318, "Strategies and Methods for Effective UXO Classification"), we plan to carry out a direct comparison of all available multi-source solvers, including Miller's implementation in UX-Analyze.

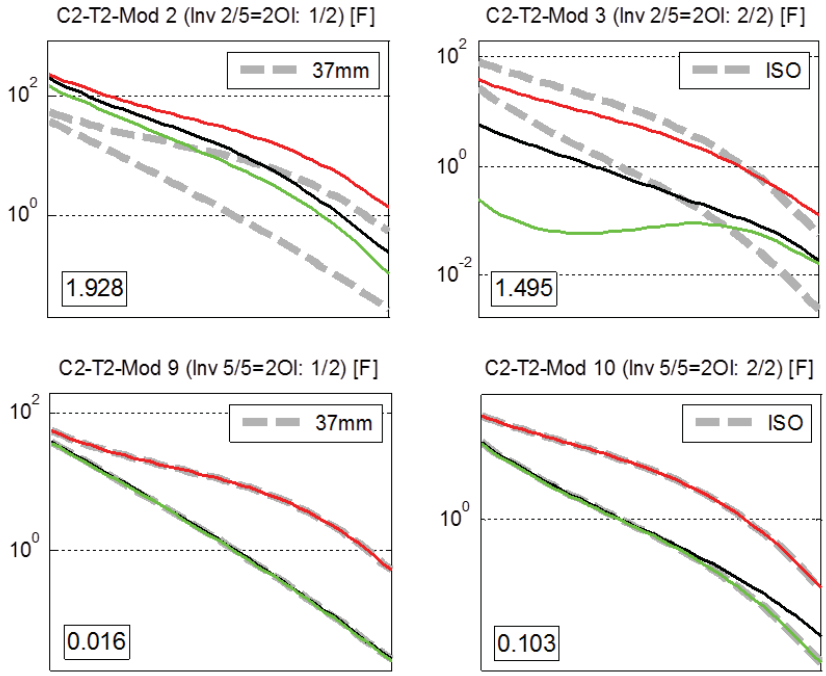

FIGURE 14. Example two-object inversion results for a cued MetalMapper sounding. Top row: recovered polarizabilities (solid lines) and best fitting reference polarizabilities (dashed lines). Bottom row: Inversion results for re-initialized two-object inversion, with the same settings as top result. In this example one of the two targets is in fact a 37mm projectile. Based on the match with the reference polarizabilities, we therefore conclude that the top row results from convergence to incorrect source locations at a local minimum of the data misfit.

For underdetermined source localization, we define a grid of sources arranged beneath the MetalMapper array (figure 15). We estimate the six unique elements of the polarizability tensor at all M points in the grid. To forward model N data $\mathbf{d}$ via the linear equation $\mathbf{d} = \mathbf{Gm}$, we therefore form an $N \times 6M$ forward matrix $\mathbf{G}$. For MetalMapper data we have $N = 63$ and so $N < 6M$ even for very coarse regular grids. Hence the inverse problem becomes non-unique and additional information (regularization) must be introduced to obtain useful estimates of source locations. As in section 3, we minimize the norm

$$\phi = \phi_d + \beta\phi_m. \tag{5}$$

The model norm (ϕ_m) restricts the space of feasible solutions and allows us to recover a model with specified properties. The most straightforward solution to the underdetermined problem uses an L2 model norm ($\phi_m = \|\mathbf{m}\|^2$). Figure 16 shows an example fit and recovered source model using the L2 model norm. In this case we have used a manually-selected regularization parameter β that produces a good fit to the data. In this figure and all similar plots in this section we shade source locations based upon the source amplitude, defined here as the trace of the recovered polarizability tensor at each location. L2 regularization favors a smoother solution and so the true source in this example is recovered as a diffuse distribution

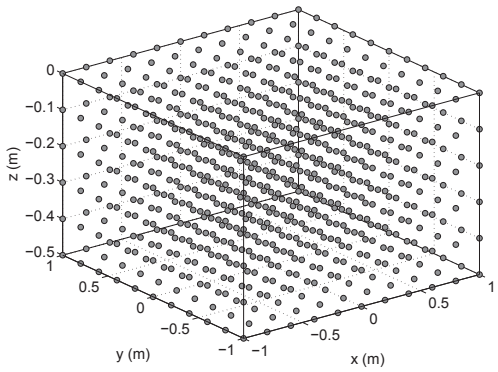

FIGURE 15. Source locations for underdetermined inversion of MetalMapper data

of sources. The smoothing effect of the L2 norm can be removed by regularizing with an L1 model norm ($\phi_m = |\mathbf{m}|$) , as in Miller et al. (2010). We use the "basis pursuit denoising" code of van den Berg and Friedlander (2008) to solve the problem

$$\min |\mathbf{W_m m}| \text{ subject to } \|\mathbf{d} - \mathbf{Gm}\|^2 < \tau \tag{6}$$

with τ functioning as a regularization parameter that controls the trade-off between fitting the data (small τ) and minimizing the model norm (large τ). We introduce the weighting matrix $\mathbf{W_m}$ into the model norm to compensate for the geometric decay of the sources as a function of distance from the sensor. This effect is manifested by the concentration of large amplitude sources near the surface in figure 16. For underdetermined inversion of magnetic data, Li and Oldenburg (1996) weight the model by $1/z^3$ to counteract a similar

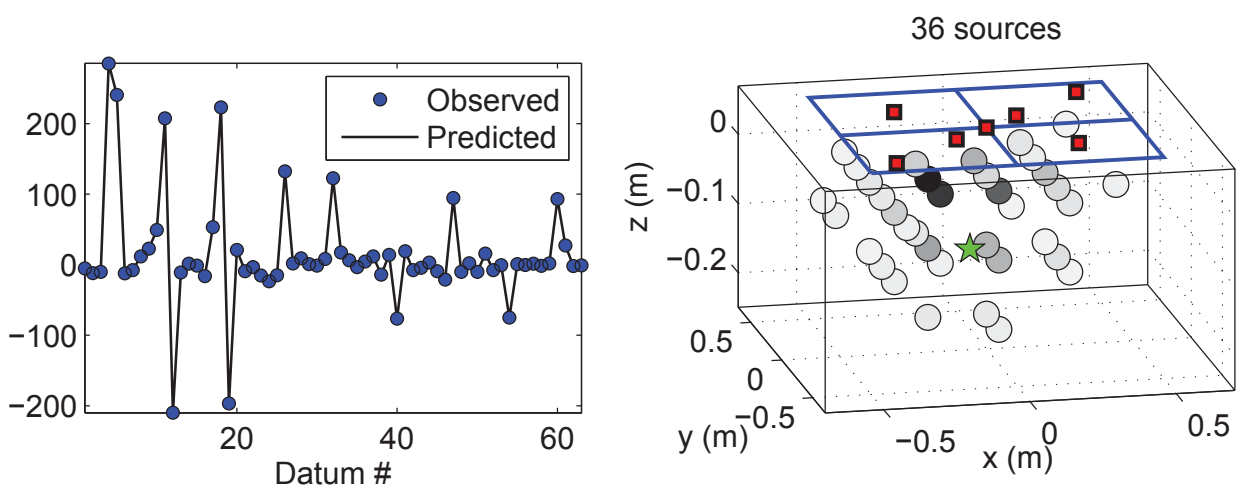

FIGURE 16. Regularized source localization with an L2 norm. Left: Synthetic observed data and data predicted with estimated source model. Right: Source locations are shaded by total polarizability amplitude (trace of the polarizability tensor). For clarity, in this example only locations with amplitude greater than 5 percent of the maximum amplitude are displayed. Darker circles indicate a greater source amplitude. Actual target location is indicated by a green star. MetalMapper transmitter and receiver locations are shown above source grid for reference.

concentration of high susceptibilities near the surface. In this problem, we can understand the decay of the secondary field by considering the amplitude of the kernel

$$g = \sqrt{\mathrm{diag}(\mathbf{G}^T\mathbf{G})} \tag{7}$$

as a function of distance to the sensor (figure 17). As expected, the decay of the secondary field asymptotes to $1/z^6$ in the far field. Closer to the sensor, however, the primary field falls off as $1/z$, resulting in an overall $1/z^4$ dependence. To account for this variable decay

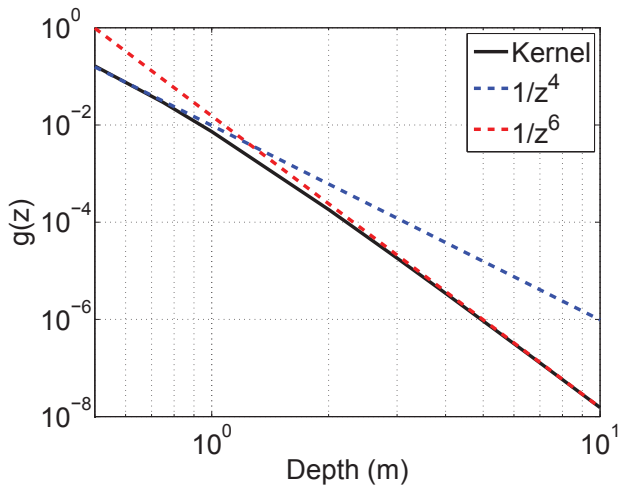

FIGURE 17. Decay of forward modeling matrix kernel g(z) as a function of source depth z.

rate, we define a diagonal weighting matrix with elements

$$W_{m_{ii}} = 1/g_i. \tag{8}$$

This boosts the contribution of deeper sources to the model norm and allows for recovery of larger amplitude sources at depth. A second form of the model weighting matrix couples the elements of the polarizability tensor at each location to ensure recovery of a physically-meaningful model. If the sparse inversion recovers a non-zero polarizability at a given location, then all 6 of the elements of the tensor at that location should be nonzero. We have achieved this constraint by creating a block diagonal weighting matrix

$$\mathbf{W_m} = \mathrm{diag}(\Omega_j)\ j{=}1{\ldots}M. \tag{9}$$

The 6×6 block corresponding to the jth source is

$$\Omega_j = V_j\sqrt{\mathrm{diag}(1/D_j)}V_j^T \tag{10}$$

where V_j and D_j are the eigenvector and eigenvalue matrices of the submatrix Γ_j

$$\begin{aligned} \Gamma_j &= (\mathbf{G}^T\mathbf{G})[k,l], \quad 6(j-1)+1 \le k,l \le 6(j-1)+6 \\ &= V_j D_j V_j^T. \end{aligned} \tag{11}$$

Figure 18 shows the effect of model weighting on the sparse inversion result. We see in 17(b) that the unweighted model places the strongest sources above the actual target location.

Using the diagonal weighting matrix in 18(c), forces the sources to the correct depth. The block diagonal weighting matrix in (d) produces a similar result as in (c), but with the correct number of non-zeroes for the number of recovered sources.

While figure 18 suggests that sparse underdetermined inversion coupled with proper model weighting is a feasible approach to source localization, further experiments have produced less promising results. Figure 19 shows underdetermined inversion results for a two object scenario with a large (105 mm) target at 40 cm depth and a small 37 mm projectile at 10 cm depth. In this figure we have varied the regularization parameter τ to illustrate the trade-off between fitting the data and obtaining a sparse model. There is no obvious inflection point on the Tikhonov (or Pareto) curve (leftmost plot in figure 19) and the two norms are not particularly smooth functions of τ. The sparsest recovered model (i.e. minimum model norm) places the strongest sources at depth, roughly at the location of the 105 mm item, but there is a halo of lower amplitude sources that preclude clear identification of the 37 mm projectile. Other recovered models in figure 19 require a large number of sources to produce better fits to the data; none of these models is very useful for recovering the true source locations. Regularization with an L1 norm can produce a well-posed inverse problem but seemingly cannot, in this example, recover a model that fits the data and reproduces the true source locations.

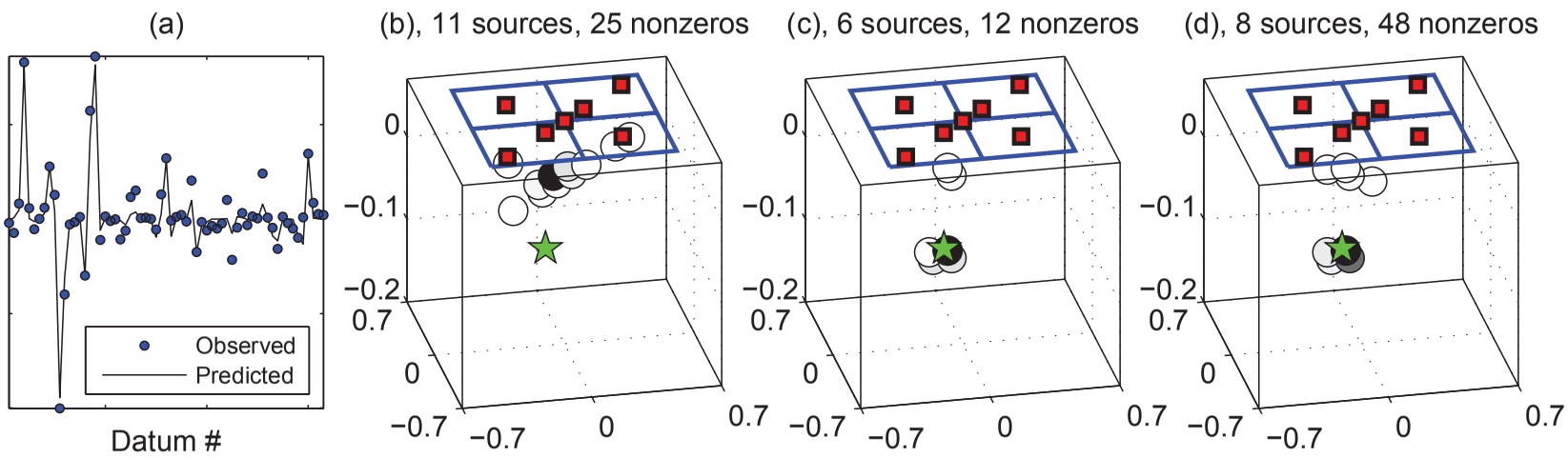

FIGURE 18. Effect of model weighting on sparse inversion. (a) Synthetic observed MetalMapper data and data predicted by sparse inversion models. All recovered models in this example produce the same fit to the data. (b) Non-zero source locations for unweighted sparse inversion. (c) Non-zero source locations for weighted sparse inversion with diagonal weighting matrix. (d) Non-zero source locations for weighted sparse inversion with block diagonal weighting matrix.

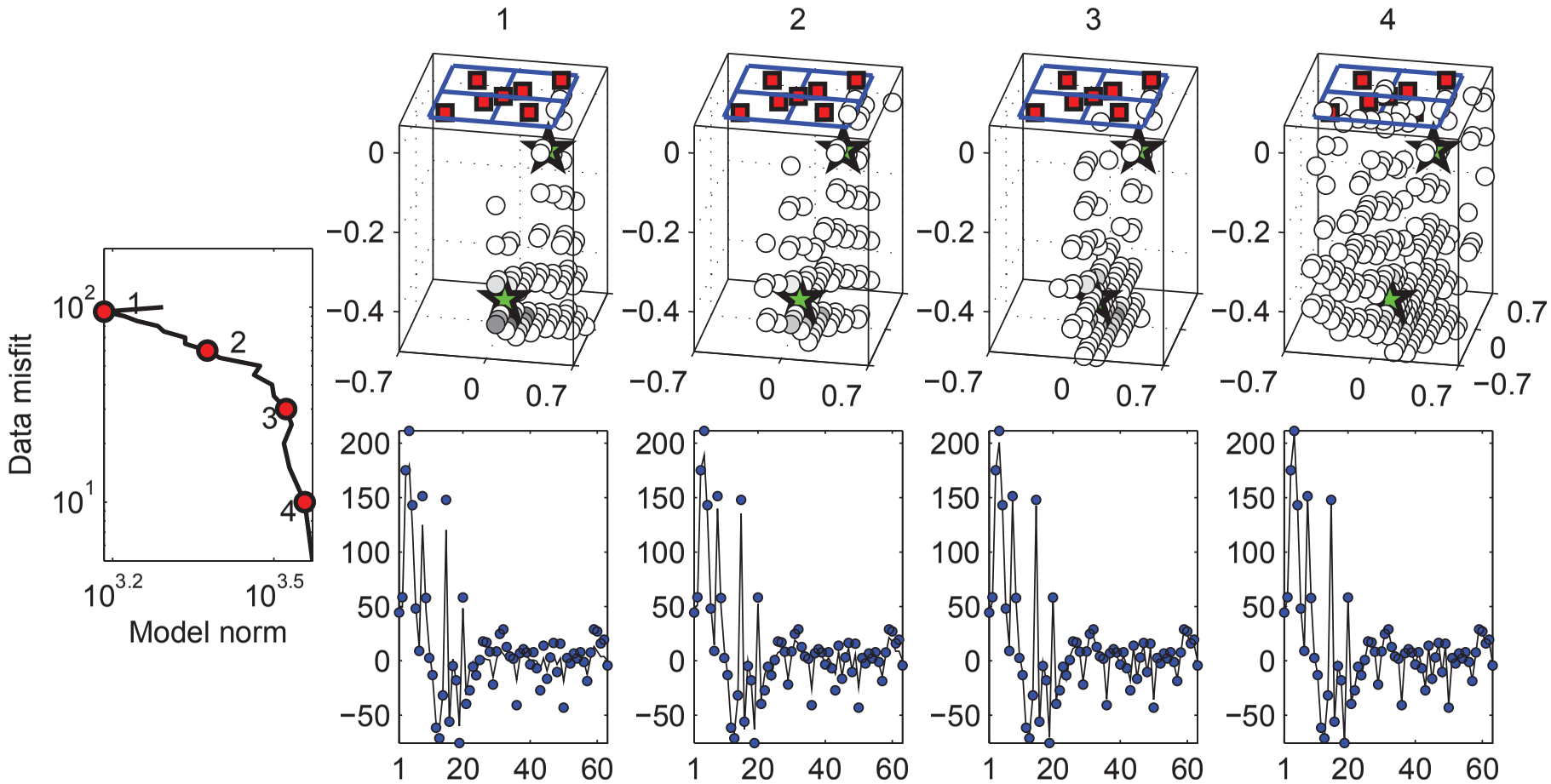

FIGURE 19. Synthetic two-object sparse inversion example. The two targets in this case are a 105mm projectile at [0, 0, −0.4] m, and a 37 mm projectile [0.3, 0.3, −0.1] m. The MetalMapper is at 0.07 m height. Leftmost plot shows data misfit and model norm for basis pursuit denoising of synthetic MetalMapper data with varying regularization parameter τ. Numbered points on the curve indicate recovered models shown in top row of plots. True source locations are indicated by large green stars. Bottom row of plots indicates fit (solid line) to observed data (markers) for each numbered model.

The example in figure 19 is a relatively simple two-object scenario that is readily recovered with the overdetermined method of Song et al. (2011) (figure 20). We therefore conclude that an underdetermined formulation has limited practical utility for dipole location estimation in multi-object scenarios.

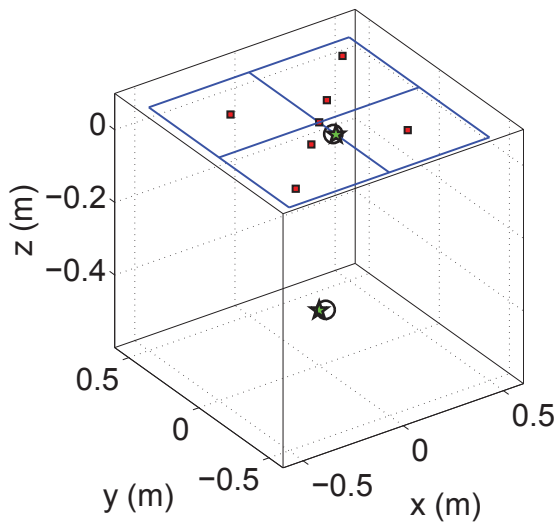

FIGURE 20. Two-object overdetermined inversion example. Synthetic data for this example are the same as in figure 19. True source locations are indicated by green stars. Open circles - nearly coincident with the true locations - are source locations estimated by nonlinear overdetermined inversion for two objects.

4.2. **Overdetermined location estimation.** We now turn to regularization of overdetermined location estimation. For the MetalMapper, we have $N = 63$ data at each time channel. If we again consider a predefined grid of source locations, then the (linear) inverse problem for the six polarizability tensor elements at all locations remains overdetermined for up to ten sources. This is obviously too coarse a grid to use for precise target localization, and so we must directly solve for source positions $\mathbf{r}$. The data now depend nonlinearly on the model

$$\mathbf{d}^{pred} = F(\mathbf{m}) = \mathbf{G}(\mathbf{r})\mathbf{G}^{\dagger}(\mathbf{r})\mathbf{d}^{obs} \tag{12}$$

with the model $\mathbf{m} = \mathbf{r}$. Miller et al. (2010) consolidate sources estimated via overdetermined sparse inversion with clustering algorithms. Alternatively, Song et al. (2011) specify the desired number of sources *a priori* and find the model $\mathbf{m}$ that produces the best fit to the data, as illustrated in figure 20.

We have developed an approach that clusters sources during an inversion by penalizing the total distance between sources

$$\phi_m = \sum_{i \neq j} \Delta_{ij}^2, \tag{13}$$

with Δ_{ij} the distance between sources i and j, as depicted in figure 21. Figure 22 summarizes

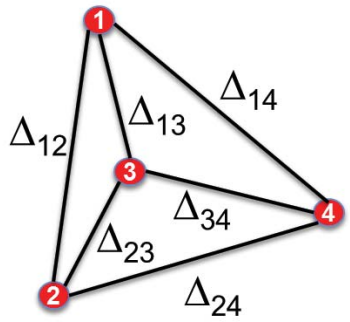

FIGURE 21. Computation of the total distance between sources.

the method. We start with an unregularized inversion, eliminate redundant sources based on their proximity, and then progressively increase the distance regularization (equation 13) to force sources to cluster together. When two or more sources are less than a specified distance Δ_{thresh} apart, they are merged into a single source.

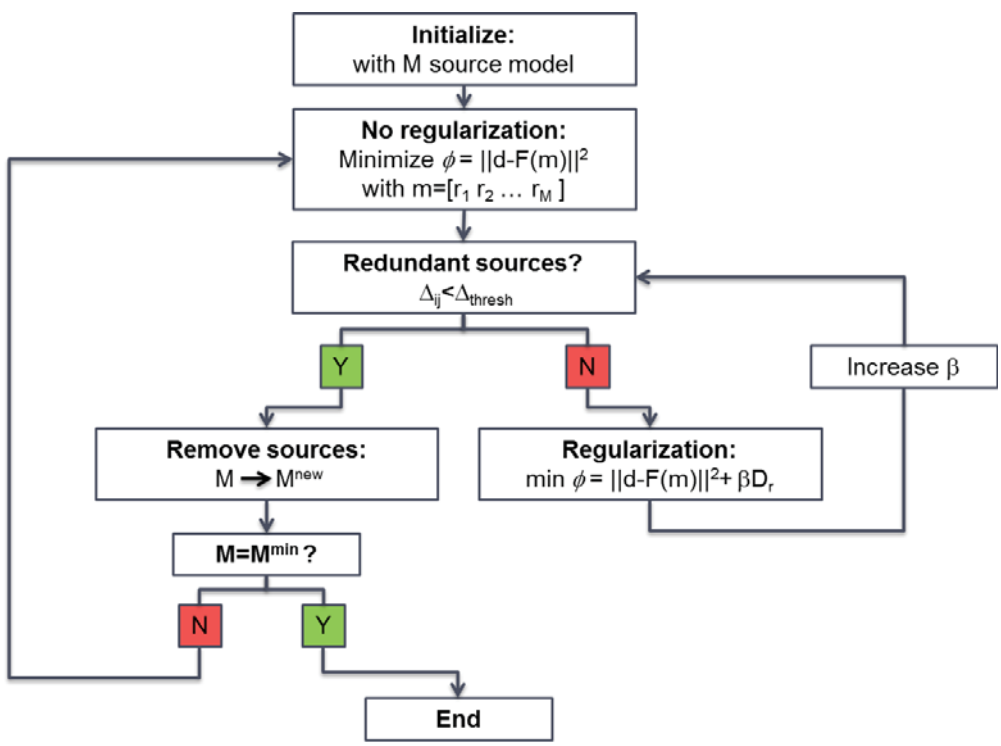

FIGURE 22. Flowchart for overdetermined inversion with distance regularization.

This algorithm incurs additional computational cost by requiring simultaneous forward modelling for multiple sources. A new implementation of the forward modelling reduces computation time by about an order of magnitude (figure 23) by eliminating repeated calculations. This somewhat alleviates the computational overhead of the regularized algorithm.

As shown in figure 24, the method produces a series of models with decreasing numbers of sources and increasing data misfit. When there are more sources than necessary (e.g.

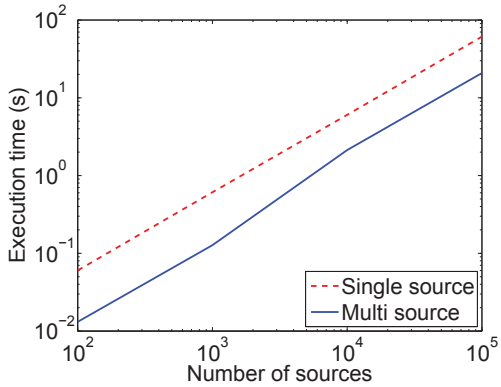

FIGURE 23. Comparison of execution times for single and multi-source implementations of forward modelling matrix **G**

$M = 9$ in figure 24), then the data can be fit quite closely by a tight spatial distribution of sources. It is only when redundant sources are eliminated (i.e. $M \leq 5$ that the model is forced to move sources apart in order to fit the data. In this example the true source locations are ultimately recovered by the algorithm when $M = 2$. The regularized result is not an improvement over Song's unregularized approach (figure 20) and the regularized algorithm is considerably slower since more model parameters must be estimated.

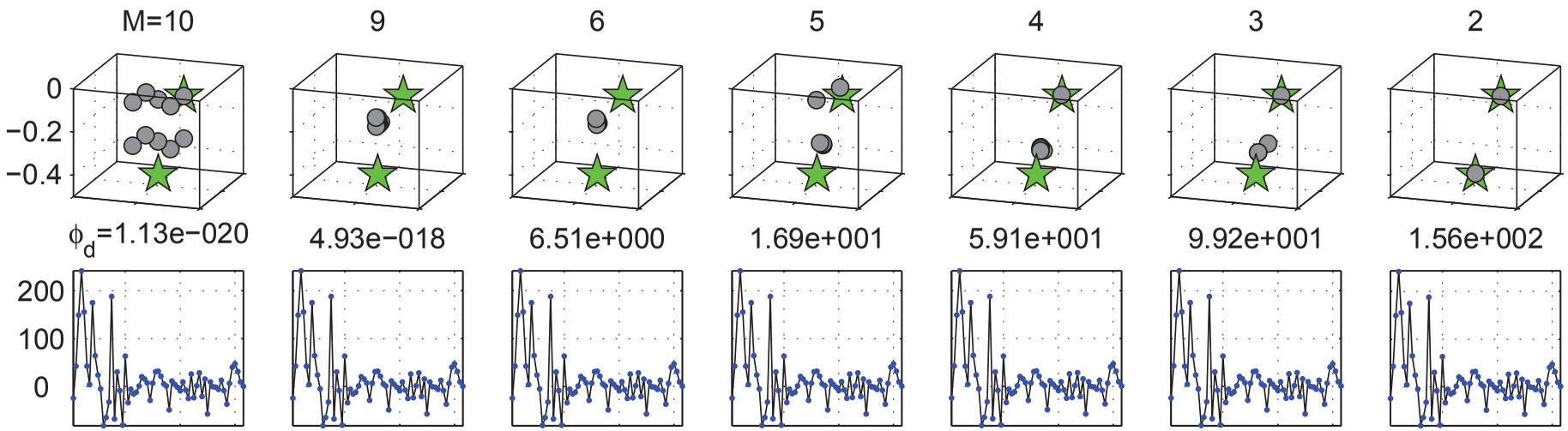

FIGURE 24. Location estimation with distance regularization. Top row: recovered models (circles). True source locations are indicated by green stars, true model in this case is the same as in figures 19 and 20. The number of unique sources M is displayed above each plot. Bottom row: Observed data (dots) and predicted data (solid line) for each model. The corresponding data misfit ϕ_d is displayed above each plot.

In numerical experiments we have found that the regularized location estimation algorithm identifies the same set of source locations as Song's multi-object code (figure 25). The former approach is about four times slower, but does not rely on randomized start models.

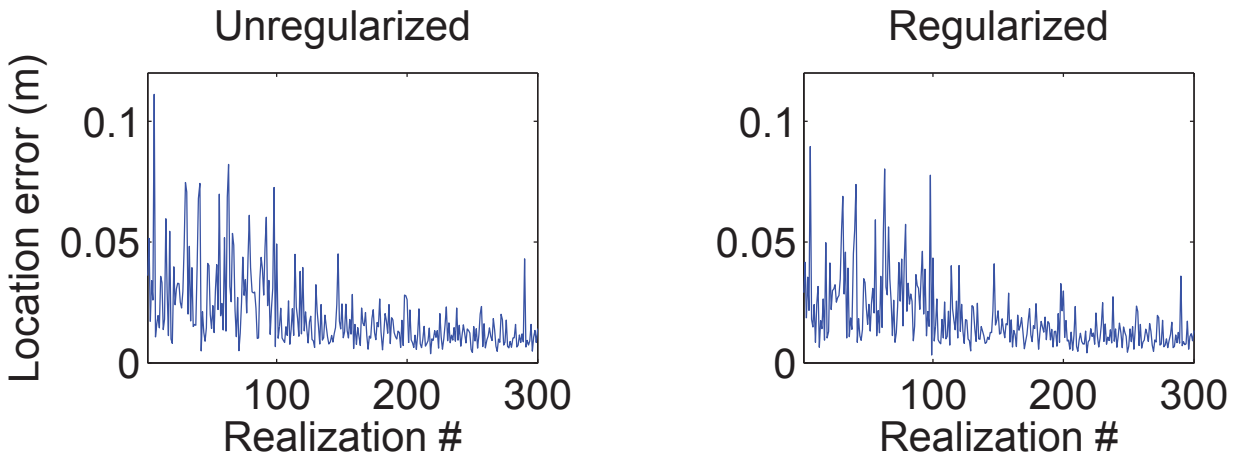

FIGURE 25. Comparison of error in estimated locations for inversion of synthetic data sets with unregularized and regularized algorithms. Data realizations are two source (37 mm and ISO) scenarios at a range of depths and separations.

In this section we have developed underdetermined and overdetermined regularized inversion algorithms for dipole location estimation. The latter has promise for practical application in production codes. Further testing and direct comparison with multi-object inversion codes in UX-Analyze will be pursued in SERDP MR-2318.

5. Conclusions and recommendations for future research

Under follow-on funding for MR-1629 we have developed improved algorithms for inversion of multi-static EMI data. Measured data from sensors such as the MetalMapper and TEMTADS ideally produce well-constrained polarizabilities that closely match reference polarizabilities. These hardware improvements have made some data processing techniques developed in the first phase of this project largely obsolete. For example, explicitly integrating over parameter uncertainty, as developed in Beran et al. (2011), produces negligible benefits for multi-static data. On the other hand, other techniques - e.g. using multiple models for classification - are now routinely used in UXO processing.

Additional data processing techniques presented here address identification of TOI with multi-static EMI sensors in difficult, low SNR scenarios. Robust inversion, regularization, and the TOPI method all attempt to mitigate the effects of noise on recovered polarizabilities. All of these methods produce a model that is a somewhat worse fit to the observed data than standard least squares inversion. The benefit of this reduced fit is often a polarizability model that is a better match to reference polarizabilities.

Similarly, multi-stage techniques for target classification try to identify noisy TOI polarizabilities by progressively reducing the dimensionality of the feature space. The Combined Classifier Ranking (CCR) developed here is a variant that uses all features simultaneously, thereby eliminating the need to switch between feature sets. We routinely use these approaches for classification of ESTCP data sets and have implemented them into our classification software.

We have not completely addressed all research that was proposed under MR-1629. Remaining topics are:

(1) *Robust statistical norms and multiple objects in the field of view.* This question has largely been addressed with TOPI and regularized multi-object inversion. As discussed above, these methods all try to balance the fit to the data with recovery of denoised polarizabilities.

(2) *Methods to determine when to stop digging.* This problem is being investigated under MR-2226, "Decision support tools for munitions response performance prediction and risk assessment." Under this project we have developed methods for assigning an objective numerical confidence to the stop dig point determined by an analyst.

(3) *Include positional uncertainty in the inversion algorithm.* The degraded positional accuracy of dynamic data motivated past work (Tarokh and Miller, 2007; Tantum et al., 2008) on this problem. While cued interrogation largely circumvents the requirement for accurate positioning, recent efforts to classify with dynamic multi-static data motivate further examination of positional uncertainties. Methods that mitigate the effects of positional errors will also be applicable to marine UXO classification. This topic will be studied under SERDP MR-2318, "Strategies and Methods for Effective UXO Classification."

References

L. Beran, B. Zelt, L. Pasion, S. Billings, K. Kingdon, N. Lhomme, L.-P. Song, and D. Oldenburg. Practical strategies for classification of unexploded ordnance. *Geophysics*, 78, 2012.

L. S. Beran, S. D. Billings, and D. W. Oldenburg. Incorporating uncertainty in unexploded ordnance discrimination. *Geoscience and Remote Sensing, IEEE Transactions on*, 49(8): 3071–3080, 2011.

L. S. Beran, S. D. Billings, and D. W Oldenburg. Regularizing dipole polarizabilities in time-domain electromagnetic inversion. *Journal of Applied Geophysics*, 85:59–67, 2012.

S.D. Billings, L. S. Beran, and D. W. Oldenburg. Final report: Robust statistics and regularization for feature extraction and UXO discrimination, SERDP Project MR-1629. Technical report, SERDP, 2011.

C. G. Farquharson and D. W. Oldenburg. A comparison of automatic techniques for estimating the regularization parameter in non-linear inverse problems. *Geophys. J. Int.*, 156: 411–425, 2004.

Y. Li and D.W. Oldenburg. 3-D inversion of magnetic data. *Geophysics*, 61:394–408, 1996.

W. Menke. *Geophysical Data Analysis: Discrete Inverse Theory*. Academic Press, 1989.

J. T. Miller, D. Keiswetter, J. Kingdon, T. Furuya, B. Barrow, and T. Bell. Source separation using sparse-solution linear solvers. In *Proc. SPIE 7664, Detection and Sensing of Mines, Explosive Objects, and Obscured Targets XV*, pages 766409–766409–8, 2010.

D.W. Oldenburg and Y. Li. *Investigations in Geophysics No.13: Near-surface*, chapter Inversion for applied geophysics: A tutorial, pages 89–150. Society of Exploration Geophysics, 2005.

L. P. Song, L. R. Pasion, S. D. Billings, and D. W. Oldenburg. Nonlinear inversion for multiple objects in transient electromagnetic induction sensing of unexploded ordnance: Technique and applications. *IEEE Trans. Geosci. Remote Sensing*, 49(10):4007 –4020, 2011.

S. L. Tantum, Y. Li, and L. M. Collins. Bayesian mitigation of sensor position errors to improve unexploded ordnance detection. *IEEE Geosci. Remote Sensing Letters*, 5:103–107, 2008.

A. B. Tarokh and E. L. Miller. Subsurface sensing under sensor positional uncertainty. *IEEE Trans. Geosci. Remote Sensing*, 45:675–688, 2007.

E. van den Berg and M. P. Friedlander. Probing the pareto frontier for basis pursuit solutions. *SIAM Journal on Scientific Computing*, 31(2):890–912, 2008.

Appendix A. Published articles

A.1. **Temporal Orthogonal Projection Inversion Technique for EMI Sensing of UXO.**

L. P. Song, D. W. Oldenburg, L. R. Pasion, S. D. Billings, and L. S. Beran (2013). Temporal Orthogonal Projection Inversion Technique for EMI Sensing of UXO. IEEE Transactions on Geoscience and Remote Sensing, in preparation.

Temporal Orthogonal Projection Inversion Technique for EMI Sensing of UXO

Lin-Ping Song, *Member, IEEE*, Douglas W. Oldenburg, L. R. Pasion, S. D. Billings, and L. Beran

Abstract

This paper presents a new inversion method that is based upon the singular value decomposition (SVD) analysis of multiple-time channel responses. First, we form the multi-channel EMI sensor data as a spatial-temporal response matrix (STRM). The rows of the STRM correspond to measurements sampled at different time channels from one sensor and the columns correspond to measurements sampled at the same time channel from different sensors. The SVD of the STRM produces the left and right singular vectors that are related to the sensor and the temporal spaces, respectively. If the effective rank of the STRM is r, then the first r left and right singular vectors span signal subspaces (SS). The remaining singular vectors span the noise subspaces. Next, we do a one-sided projection by right multiplying the STRM with the temporal signal subspace matrix and obtain a transformed response matrix whose r columns are termed as the SS temporal channels. This derives a temporal orthogonal projection inversion (TOPI) where the r SS projected temporal channels are used for source locations in the transformed system of equations and the target polarizabilties are solved as a linear optimization problem in the original data domain. The theoretical and numerical analysis based upon the magnetic dipole model is presented on the determination of r. The proposed approach is evaluated using the synthetic and real multi-static EMI (TEMTADS) data.

Index Terms

Electromagnetic induction, Unexploded ordnance, Magnetic dipole polarization, Orthogonal projection, Subspace, Nonlinear inversion

I. Introduction

Electromagnetic induction (EMI) sensing has been a major protocol in environmental remediation of unexploded ordnance (UXO) contamination [1] - [29]. Its effective use relies upon an inversion processing technique that is capable of extracting accurate target signatures (e.g., dipolar polarizabilities) from measured data for input to subsequent tasks of discriminating UXO from non-hazardous clutter [20]-[22].

EMI signal processing is generally cast as a nonlinear inversion problem where the location of an object and its principal polarizations are sought for best explaining data [6] -[8], [12]-[13], [23]-[29]. Modern EMI data are

This work was supported by a SERDP grant MR-1629

Lin-Ping Song and Douglas W. Oldenburg are with Department of Earth, Ocean and Atmospheric Sciences, University of British Columbia, E-mail: lpsong@eos.ubc.ca.

Leonard R. Pasion, Stephen D. Billings, and Laurens Beran are with the Black Tusk Geophysics Inc, Vancouver, Canada

acquired as a series of transient responses to a nearby object with an array of sensors. An inversion is typically carried out using the responses at a subset of the measured time channels. This involves in a process of pre-selecting time channels to be used. It might be done based upon a priori estimates of the unknown sensor noise. A usual rule of thumb is to choose responses above a pre-defined SNR threshold in order to avoid possible adverse effects of late time noisy measurement on the estimated source parameters. This channel selection method works reasonably well if a good a-priori estimate of sensor noise is available across data sets. If noisy data are included however, the quality of the inversion result is degraded.

In this paper, we present a method that is not so dependent upon a-priori noise estimates. We first define the spatial-temporal response matrix (STRM). This is the data matrix whose rows correspond to measurements at different time channels from one sensor (that is, a single transmitter-receiver pair), that is, each row is the time domain decay curve for a particular sensor. The columns of the STRM are measurements at all sensors at a single time. The SVD (Singular Value Decomposition) of this matrix provides a well defined set of vectors with which to expand the rows of the STRM. We project the time domain decay curves onto a small subspace by keeping only those vectors associated with larger singular values. A nonlinear inversion is then carried out in the transformed domain to find the source locations. The procedure, which we refer to as temporal orthogonal projection inversion (TOPI), has a number of benefits. Most importantly, the subspace projection has the potential for separating signal from additive Gaussian noise and thus higher quality and more robust solutions are obtained in the inverse problem. It also reduces the size of the inverse problem to be solved and this speeds up the process. Once good estimates are obtained for the locations of the targets, their polarizabilties are subsequently obtained by solving a linear optimization problem in the original data domain.

The remaining parts of this paper are organized as follows. In section II, the data model formulation are presented. Our existing nonlinear inversion algorithm is outlined for the development. In section III, we present the SVD analysis of the STRM that relates to the interested temporal basis and derive our projection inversion method. In section IV, we evaluate and discuss the technique using synthetic and real data recorded by the new-generation sensor array systems of TEMTADS [32]. Section V gives the conclusion.

II. Signal model

A. The polarizability tensor and formulation

In UXO surveys, where a target dimension is often small relative to the target-sensor distance, the transient scattering of a metallic object can be well described by an equivalent induced dipole [33], [34]. This dipolar dynamic property is characterized by a 3×3 symmetric magnetic polarizability tensor (MPT) $P(t)$ [1]-[12],

$$P(t) = \begin{bmatrix} p_{11}(t) & p_{12}(t) & p_{13}(t) \\ p_{12}(t) & p_{22}(t) & p_{23}(t) \\ p_{13}(t) & p_{23}(t) & p_{33}(t) \end{bmatrix}, \tag{1}$$

where each element $p_{ij}(t)$ represents a dipole component in the ith Cartesian direction due to a primary field in jth Cartesian direction and where t is time. This polarizability tensor $P(t)$ has an eigen-decomposition as

$$P(t) = \sum_{j=1}^{3} L_j(t)\mathbf{e}_j\mathbf{e}_j^T, \tag{2}$$

where $\mathbf{e}_j (j = 1, 2, 3)$ is the orthonormal eigenvector representing the jth principal direction of dipolar polarization with respect to a reference system, and $L_j(t)$ is the principal polarization strength that is a function of the geometry and material of a target. In other words, $P(t)$ contains the information regarding the geometry and material of a target as well as its orientation. Superscript T denotes a transpose operation.

For the ith measurement of M sensing Tx/Rx pairs, the secondary response d_i to an excited object might be written as an inner product form with respect to $P(t)$, [1] [12]

$$d_i(\mathbf{r}_{Rx_i}, t) = \mathbf{a}_i^T(\mathbf{r}, \mathbf{r}_{Rx_i}, \mathbf{r}_{Tx_i})\mathbf{q}(t), \tag{3}$$

where $\mathbf{a}_i(\mathbf{r}, \mathbf{r}_{Rx_i}, \mathbf{r}_{Tx_i})$ is 6×1 column vector representing spatial sensitivities of the ith sensor to the object located at $\mathbf{r}$, and $\mathbf{q}(t)$ a 6×1 column vector whose components are the elements of the polarizability tensor $P(t)$ of an object. They are given by [27]-[28]

$$\mathbf{a}_i(\mathbf{r}, \mathbf{r}_{Rx_i}, \mathbf{r}_{Tx_i}) = \begin{bmatrix} B_R^x B_T^x \\ B_R^x B_T^y + B_R^y B_T^x \\ B_R^x B_T^z + B_R^z B_T^x \\ B_R^y B_T^y \\ B_R^y B_T^z + B_R^z B_T^y \\ B_R^z B_T^z \end{bmatrix}, \mathbf{q}(t) = \begin{bmatrix} p_{11}(t) \\ p_{12}(t) \\ p_{13}(t) \\ p_{22}(t) \\ p_{23}(t) \\ p_{33}(t) \end{bmatrix}, \tag{4}$$

where $[B_R^x\ B_R^y\ B_R^z]^T$ and $[B_T^x\ B_T^y\ B_T^z]^T$ are the Cartesian components of field vectors $\mathbf{B}_R(\mathbf{r}, \mathbf{r}_{Rx_i})$ and $\mathbf{B}_T(\mathbf{r}, \mathbf{r}_{Tx_i})$ which are generated by the receiver and transmitter coils at a source location.

Assume that η objects are present in response to a given excitation. By neglecting EMI interaction between the objects [23] - [**?**], we model a measurement as a linear superposition of the signals from each object. That is, $d_i(\mathbf{r}_{Rx_i}, t) = \sum_{k=1}^{\eta} \mathbf{a}_i^T(\mathbf{r}_k, \mathbf{r}_{Rx_i}, \mathbf{r}_{Tx_i})\mathbf{q}_k(t)$ where $\mathbf{a}_i(\mathbf{r}_k, \mathbf{r}_{Rx_i}, \mathbf{r}_{Tx_i})$ defined in (4) are the spatial sensitivities of the ith senor to the kth object located at $\mathbf{r}_k$ with polarizations $\mathbf{q}_k(t)$. The observed EMI responses for M sensors, in the presence of noise, can be conveniently expressed in a vector-matrix notation

$$\mathbf{d}(t) = \sum_{k=1}^{\eta} A(\mathbf{r}_k)\mathbf{q}_k(t) + \mathbf{n}(t), \tag{5}$$

where $\mathbf{d}(t) = [d_1(t), \cdots, d_M(t)]^T$ is an $M \times 1$ measured data vector at time t, $\mathbf{n}(t)$ is the additive noise vector, and $A(\mathbf{r}_k)$ is an $M \times 6$ matrix denoting the sensitivities of the M sensors to the kth object located at $\mathbf{r}_k$. Its transpose is given by

$$A^T(\mathbf{r}_k) = \begin{bmatrix} \mathbf{a}_1(\mathbf{r}_k) & \ldots & \mathbf{a}_M(\mathbf{r}_k) \end{bmatrix}. \tag{6}$$

The position vectors of the sensor coils are suppressed in Eq. (5) for simplifying the notation. It is understood that the sensor information is a subscript-indexed in the recordings and in the sensitivity vectors. Eq. (5) is a generic dipole-based formulation for estimating and recovering the locations and polarizabilities of EMI anomalies.

B. Two-step Inversion

In this section, we briefly review the sequential inversion algorithm of TEM data [27], [28] for the later development.

In that algorithm, the model parameters are grouped into two parts: a nonlinear part consisting of source locations $\mathbf{r} = \mathrm{vec}[\mathbf{r}_1, \ \cdots, \ \mathbf{r}_\eta]$ and a linear part consisting of source polarizations $\mathbf{v}(t) = \mathrm{vec}[\mathbf{q}_1(t), \ \cdots, \ \mathbf{q}_\eta(t)]$ at time instant t. Here $\mathrm{vec}[\cdot]$ represents a vectorization operation, i.e., stacking all vectors into a single column. Since both parameter sets (see Eq. (5)) are separable where the matrix A is independent of source polarizations $\mathbf{q}_k(t)$, the algorithm treats finding source locations as a primary step in which estimating polarizations as an intermediate step.

For η objects and a given suite of starting or current locations $\mathbf{r}_c$, a nonlinear optimization is carried out to update the location by solving the following minimization problem:

$$\begin{aligned} &\tilde{\mathbf{r}} = \arg\min_{\mathbf{r}} \sum_{j=1}^{N_t} \left\| W_j(\mathbf{d}_{\mathrm{obs}}(t_j) - \tilde{\mathbf{d}}(\mathbf{r}_c, t_j) - J(\mathbf{r}_c)(\mathbf{r} - \mathbf{r}_c)) \right\|^2 \\ &\tilde{\mathbf{d}}(\mathbf{r}_c, t_j) = \sum_{k=1}^{\eta} A(\mathbf{r}_{c,k}) \tilde{\mathbf{q}}_k(t_j) \\ &\text{subject to } \|\mathbf{r} - \mathbf{r}_c\| < \Delta_{\mathbf{r}} \end{aligned} \quad , \tag{7}$$

where N_t is the number of time channels used during this nonlinear update, W_j is a diagonal data weighting matrix for the data at the selected time t_j and its diagonal entries correspond to the uncertainty for each datum. $J(\mathbf{r}_c)$ is the Jacobian for furnishing the descent direction in the local linearized search, $\tilde{\mathbf{d}}(\mathbf{r}_c, t_j)$ are the predicted data at $\mathbf{r}_c$, and $\Delta_{\mathbf{r}}$ is a positive scalar used to provide a local ball within which $\mathbf{r}$ is allowed to change w.r.t. $\mathbf{r}_c$. Computation of the predicted data $\tilde{\mathbf{d}}$ requires that $\tilde{\mathbf{q}}_k$ be evaluated. This is done as a nested process by solving the constrained least square problem at $\mathbf{r}_c$,

$$\begin{aligned} &\tilde{\mathbf{v}}(t_j) = \arg\min_{\mathbf{v}(t_j)} \|\mathbf{d}_{\mathrm{obs}}(t_j) - \sum_{k=1}^{\eta} A(\tilde{\mathbf{r}}_{c,k}) \mathbf{q}_{c,k}(t_j)\|^2 \\ &\text{s.t.} \\ &p_{k,ii}(t) \geq 0 \\ &|p_{k,ij}(t)| \leq \frac{1}{2}\left[p_{k,ii}(t) + p_{k,jj}(t)\right]. \end{aligned} \tag{8}$$

The constraints imposed in (8) arise from the symmetric positive definite matrix in Eq. (1) [35] - [36].

The iterations in (7) are continued until convergence criteria are satisfied. This yields a set of final locations $\tilde{\mathbf{r}}_k$ and polarizations $\tilde{\mathbf{q}}_k (k = 1, \cdots, \eta)$ are obtained by (8) for all time channels. The source orientations and principal polarizations can be simply obtained by the eigen-decomposition of the MPT at each time channel. It is observed

in Eq. (7) that an estimate of source locations is depends upon the response at N_t selected time channels. The issue of channel selection will be focused in the next.

III. Method

A. Spatial-temporal response matrix and its SVD

EMI data are generally acquired where an array of sensors is deployed above the surface to interrogate an object. Each sensor records a transient series, say, $t_1, \cdots, t_J$. Assuming M Tx/Rx pairs, we arrange data as

$$D = \begin{bmatrix} d_1(t_1) & \cdots & d_1(t_J) \\ \vdots & \vdots & \vdots \\ d_M(t_1) & \cdots & d_M(t_J) \end{bmatrix}. \tag{9}$$

We call this the spatial-temporal response matrix (STRM). Its row corresponds to responses sampled at different time channels from one transmitter/receiver pair and its column to measurements sampled at the same time channel from different transmitter/receiver combinations. The STRM can be formed for a static or a dynamic survey with mono-static or multi-static array configurations.

The singular value decomposition (SVD) [35], [36] of D in Eq. (9) is written as

$$D = U\Sigma V^T = \sum_{i=1}^{p} \sigma_{ii}\mathbf{u}_i\mathbf{v}_i^T, \tag{10}$$

where $p = \min(M, J)$, $U = [\mathbf{u}_1, \cdots, \mathbf{u}_M]$ is an $M \times M$ left orthonormal matrix and $V = [\mathbf{v}_1, \cdots, \mathbf{v}_J]$ is an $J \times J$ right orthonormal matrix, and Σ is an $M \times J$ singular value matrix with elements σ_{ii} along the diagonal and zeros everywhere else. If the singular values are ordered so that,

$$\sigma_{11} \geq \sigma_{22} \geq \cdots \sigma_{pp} \geq 0 \tag{11}$$

and if the matrix has a rank $r < p$, then the last singular values are equal to zero, and the SVD of D becomes

$$D = \sum_{i=1}^{r} \sigma_{ii}\mathbf{u}_i\mathbf{v}_i^T. \tag{12}$$

Next, we relate the triplet $\{\sigma_i, \mathbf{u}_i, \mathbf{v}_i\}$ of the STRM in Eq. (12) to field quantities A and $\mathbf{q}$.

To make the following derivation simple, we consider a single-object case. Recall that Eq. (3) represents a mathematical expression for the measured EMI response to a single object. Replacing each entry in Eq. (9) with Eq. (3), we have Eq. (9) as

$$D = A(\mathbf{r})Q^T, \tag{13}$$

where $A(\mathbf{r})$ is an $M \times 6$ array response matrix defined in Eq. (6). Q^T is a $6 \times J$ source matrix

$$Q^T = \begin{bmatrix} \mathbf{q}(t_1) & \cdots & \mathbf{q}(t_J) \end{bmatrix}, \tag{14}$$

whose column corresponds to one temporal component of the dynamic polarizability tensor.

To generate an SVD form of Eq. (13), we introduce the two symmetric matrices [35],

$$W_A = (A^T A)^{\frac{1}{2}}, \quad W_Q = (Q^T Q)^{\frac{1}{2}}. \tag{15}$$

Using W_A and W_Q, we transform D in Eq. (13)

$$D = AW_A^{-1}W_AW_Q(QW_Q^{-1})^T. \tag{16}$$

Set

$$U_A = AW_A^{-1}, \quad V_Q = QW_Q^{-1}, \quad X = W_AW_Q, \tag{17}$$

where $U_A^TU_A = I$ and $V_Q^TV_Q = I$. Taking the SVD of X as $X = U_X\Pi V_X^T$, we rewrite Eq. (16) as

$$D = (U_AU_X)\Pi(V_QV_X)^T. \tag{18}$$

This is an analytical form of SVD decomposition of D where the left singular vectors are the columns of U_AU_X and the right singular vectors are the columns of V_QV_X. The singular values of D are the diagonal entries of Π, i.e., the eigenvalues of the square matrix X. There is no an explicit connection of Π with the principal polarizabilities of L. In other words, the eigenvalues of an STRM cannot be simply interpreted as apparent principal polarizabilities as in the multi-static response (MRM) that has measurements taken at one location and requires a sufficient number of transmitters and receivers [30], [31].

SVD provides a unique decomposition and hence comparing (18) to (12) leads to,

$$U_AU_{X,i} = \mathbf{u}_i, \quad V_QV_{X,i} = \mathbf{v}_i, \quad i = 1, \cdots, r, \tag{19}$$

where $U_{X,i}$ and $V_{X,i}$ represent the ith column of U_X and V_X. Eq. (19) shows that for $\sigma_{ii} > 0$ the singular vectors $\mathbf{u}_i$ are the linear combinations of the orthornormalized array Green's function matrix U_A and form a set of orthornormal basis spanning the sensor-target location space, while the singular vectors $\mathbf{v}_i$ are linear combinations of the orthornormalized polarizability source matrix V_Q and form a set of orthornormal basis spanning the temporal space. Both left and right singular vectors contain information of the target location and polarizability. The former in principle can be used in MUSIC-like imaging to estimate target location [30]. However in this development, our scope is concentrated on the use of the latter as a basis to project original temporal responses for inversion.

B. Rank and the number of targets

For a data matrix D given in Eq. (9), its rank $r \leq p = \min(M, J)$. However, recalling $D = AQ^T$ as in Eq. (13), we know from the matrix analysis theory [35] that $\mathrm{rank}(D) = \mathrm{rank}(AQ^T) \leq \min[\mathrm{rank}(A),\ \mathrm{rank}(Q^T)]$. This restricts the maximum rank of D for a single object is 6 since both $\mathrm{rank}(A) \leq 6$ and $\mathrm{rank}(Q^T) \leq 6$. In fact, Q, which contains polarizabilities, is really controlled by 3 parameters L_j. Using Eq. (2), we can express Q^T as $Q^T = EL$, where E is a 6×3 matrix whose elements are related to the principal direction directors e_j and L is a $3 \times J$ matrix whose elements are the three principal polarizabilties in J time channels. By applying the rank inequality property, we have $\mathrm{rank}(Q^T) = \mathrm{rank}(EL) \leq \min[\mathrm{rank}(E),\ \mathrm{rank}(L)] \leq 3$. So the maximum rank of Q is three. As a result, the maximum rank of D, if the data are from a single object, is three. That rank can be reduced to two for a cylindrically symmetrical object that has two distinct principal polarizabilities, or to rank one for a sphere. Theoretically, if there are η objects contributing to the data then the maximum rank is 3η.

C. Temporal Orthogonal Projection and Inversion

Assuming that the matrix has a rank r, as described in Eq. (12), we group these SVD-constructed orthonormal vectors into the left and right signal subspaces (SS), i.e., $U_s = [\mathbf{u}_1, \cdots, \mathbf{u}_r]$ and $V_s = [\mathbf{v}_1, \cdots, \mathbf{v}_r]$. The remaining singular vectors, $U_n = [\mathbf{u}_{r+1}, \cdots, \mathbf{u}_M]$ and $V_n = [\mathbf{v}_{r+1}, \cdots, \mathbf{v}_M]$, are correspondingly grouped as the left and right orthonormal noise subspaces (NS).

We want is to project the data onto V_s. Right-multiplying Eq. (13) with sub-matrix V_s, we have

$$D_s = A(\mathbf{r})Q_s^T, \tag{20}$$

where

$$D_s = DV_s, \tag{21}$$

a projected data matrix of $M \times r$ and

$$Q_s^T = Q^T V_s, \tag{22}$$

a projected source matrix of $6 \times r$ for a single-object case. Eq. (20) is a temporal orthogonal projection equation where the original J time channels are converted into r SS temporal channels but the sensitivity matrix A remains unchanged. For numerical implementation of an inversion in the transformed domain, Eq. (20) might be rewritten as a matrix-vector form for each projected temporal channel i

$$\mathbf{d}_s(i) = \sum_{k=1}^{\eta} A(\mathbf{r}_k)\mathbf{q}_{s,k}(i) + \mathbf{n}_s(i), i = 1, \cdots, r, \tag{23}$$

where $\mathbf{d}_s(i) = [d_{s,1}(i), \cdots, d_{s,M}(i)]^T$ is an $M \times 1$ projected data vector at projected channel i, $\mathbf{n}_s(i)$ is the projected noise vector. Considering the decomposition of Eq. (12) and the orthonormality of vectors $\mathbf{v}_i$, we can see that projected data $\mathbf{d}_s(i) = \sigma_i \mathbf{u}_i$ and the size of σ_i controls the importance of the ith channel.

The transformed equation (23) as in the original domain equation (5) retains the feature that $\mathbf{d}_s$ is linear with respect to source parameter $\mathbf{q}_s$ and nonlinear with respect to the locations of objects. Therefore, the same solution strategy outlined in section II-B can be applied to Eq. (23) by replacing $\mathbf{d}$ and $\mathbf{q}$ with $\mathbf{d}_s$ and $\mathbf{q}_s$ in Eq. (7) and using an identity data weighting matrix. This is the temporal orthogonal projection inversion (TOPI) where the r SS projected temporal channels are used to localize sources via the nonlinear update. Once source locations are determined, the target polarizabilties are solved as a linear optimization problem in the original data domain via Eq. (8). The orientation of each object might be extracted from the polarizability tensors through an eigen-decomposition in Eq. (2).

IV. Experiments

An important question for the TOPI concerns the size of the subspace used and nature of the associated basis vectors. To illustrate the relationship between the rank and the polarizabilties of an object, division between signal and noise subspaces, we take experiments using synthetic and real TEMATDS data. TEMTADS [32] is a single-component multi-static system. It consists of a horizontally arranged coplanar array of 5×5 transmitters and receivers

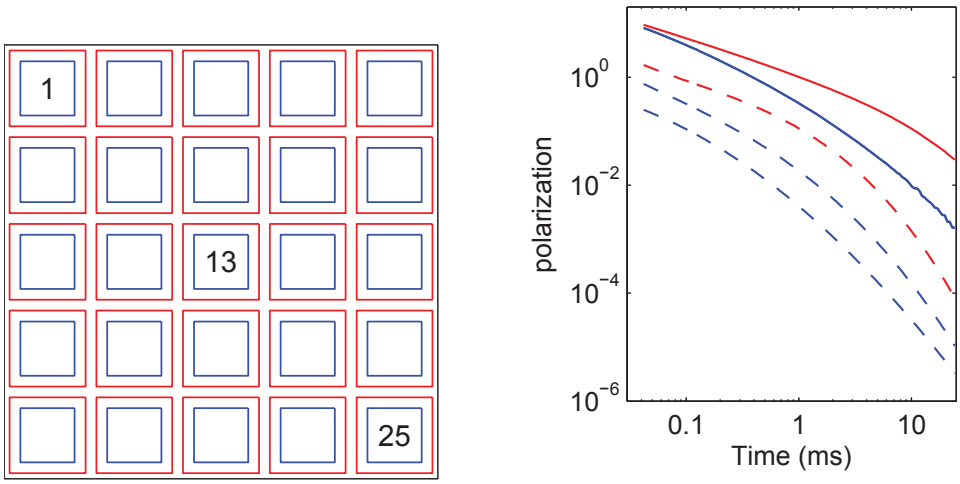

(a) (b)

Fig. 1: (a) TEMTADS: a single-component multi-static system consisting of a horizontally arranged coplanar array of 5×5 transmitters and receivers. Each transmitter is 35 cm $\times$ 35 cm and each receiver 25 cm $\times$ 25 cm. (b) Two sets of polarizabilties used for the numerical experiments. The solid and dashed curves represent polarizabilities of a 105 mm projectile and a scrap, respectively.

(Fig. 1 (a)). The sizes of its transmitters and receivers are 35 cm $\times$ 35 cm and 25 cm $\times$ 25 cm, respectively. It has 115 logarithmically spaced gates between 0.042 ms and 24.35 ms. For each transmitter excitation, TEMTADS records the response at all receivers. Thus it has spatial-temporal data of 625 $\times$ 115 for a static (cued) survey. Fig. 1 (b) shows the two sets of polarizabilties used for the numerical experiments. The solid and dashed curves represent polarizabilities of a 105 mm projectile and a scrap, respectively.

A. Synthetic single-object example

In a single-object experiment, we consider a 105 mm projectile buried at (0, 0, -0.60) m. Fig. 2 (a) is a plot of the singular values versus their indices for the noise-free case. One can see that there are two significant singular values that exactly are associated with the number of distinct polarizabilities of the cylindrical object. In the figure, we also show the singular values directly derived from the synthetic matrix D (marked as "Num.") and the singular values of Π in Eq. (18) (marked as "Ana."). Both agree well. To see how noise can have effect on singular values, we add 3%, 5%, and 10% Gaussian noise into the synthetic data. As shown in Fig. 2 (b)-(d), noise can amplify all small non-zeros singular values to a significant level that is comparable to signal singular values. In this example, it looks that signal singular values are still distinguishable with noise singular values for 10% noise case. We say that the rank of D is 2.

With respect to data subspace, its size is intimately related to the number of targets and their symmetry and strength in contributing to the observed data. From the SVD point of view, there are two factors to the determine

this: the first is the magnitude of the singular values as mentioned above; and the second is the nature of the singular vector or temporal eigenvectors (TEV) V. Figs. 2 (e) and (f) show the first 7 and the last two V for noise-free and 10% noise cases. One can observe that the first 2 singular vectors are smooth and progressively display zero crossing with their indices. These span the signal subspace with the dimension of 2. The remaining singular vectors have a random behavior associated with noise and span the noise subspace. Thus in principle it can be estimated that the maximal dimension of a signal subspace is the number of significant values or the number of smooth eigenvectors in V.

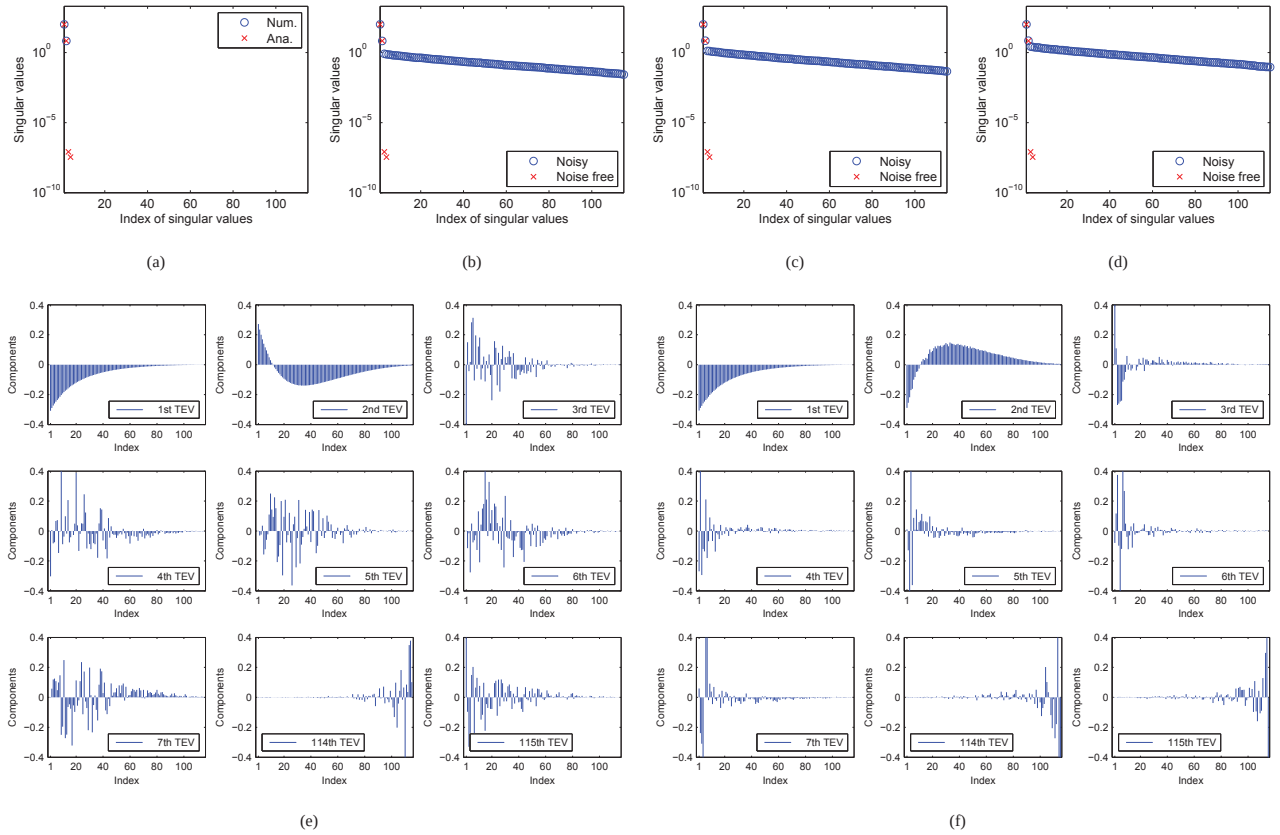

Fig. 2: Single-object case. Singular values: (a) Noise free; (b) 3% noise; (c) 5% noise; (d) 10% noise. Singular vectors: (e) Noise free; (f) 10% noise.

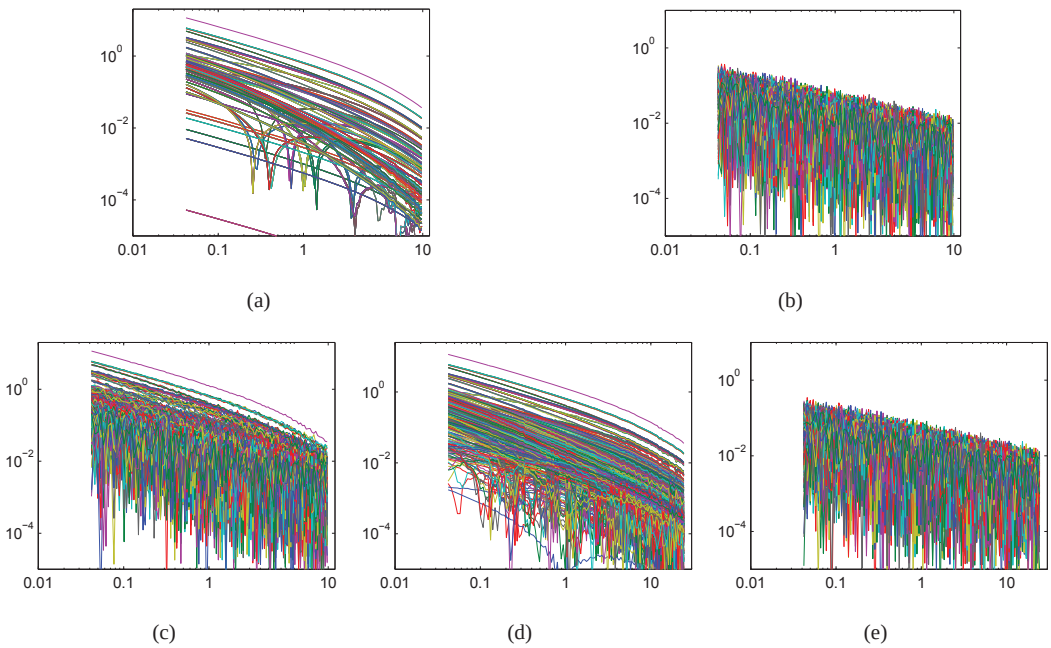

Fig. 3: Single-object case. (a) Signals. (b) Noise 10%. (c) Signals + noise. (d) Estimated signal. (e) Estimated noise.

To show the above definition of signal and noise subspaces, we do an experiment by working only within a subspace that contains smoothly decaying functions with a few oscillations. That is to reconstruct the data using $D = \sum_{i=1}^{2} \sigma_{ii} \mathbf{u}_i \mathbf{v}_i^T$ where the rank is 2. For noise, we might estimate as $N = \sum_{i=3}^{115} \sigma_{ii} \mathbf{u}_i \mathbf{v}_i^T$ where the remaining eigenvalues and vectors are used. In Fig. (3), we notice that the additive noise has been essentially eliminated when compared to noise-free signals in Fig. 3(a). Fig. 4 show the estimated signals ((a)-(d)) and noise ((e)-(h)) at different time channels. These results show that the subspace concept is a useful tool for separating signal from unwanted noise.

Notice that above signal eigenvectors are smooth and are with a few polarity changes and noise eigenvectors are oscillating. We experiment a temporal projection that is to project the data onto the space spanned by vectors V_s and V_n. The test is given in Fig. 5. It is observed that a few large values corresponding to the larger singular values and small random values thereafter. This character is easily understood. The first singular vector $\mathbf{v}_1$ is a smoothly decaying single polarity curve. It's character is similar to the data observed at many Tx/Rx pairs. Hence the inner product of that basis with the rows of D generates a large value. Inner products with other vectors that have additional zero crossings will yield smaller data values. Eventually inner products with highly variable vectors, and especially when those vectors have increasing amplitudes at larger times, produces projected data that contain little information and whose uncertainty greatly exceeds their values.

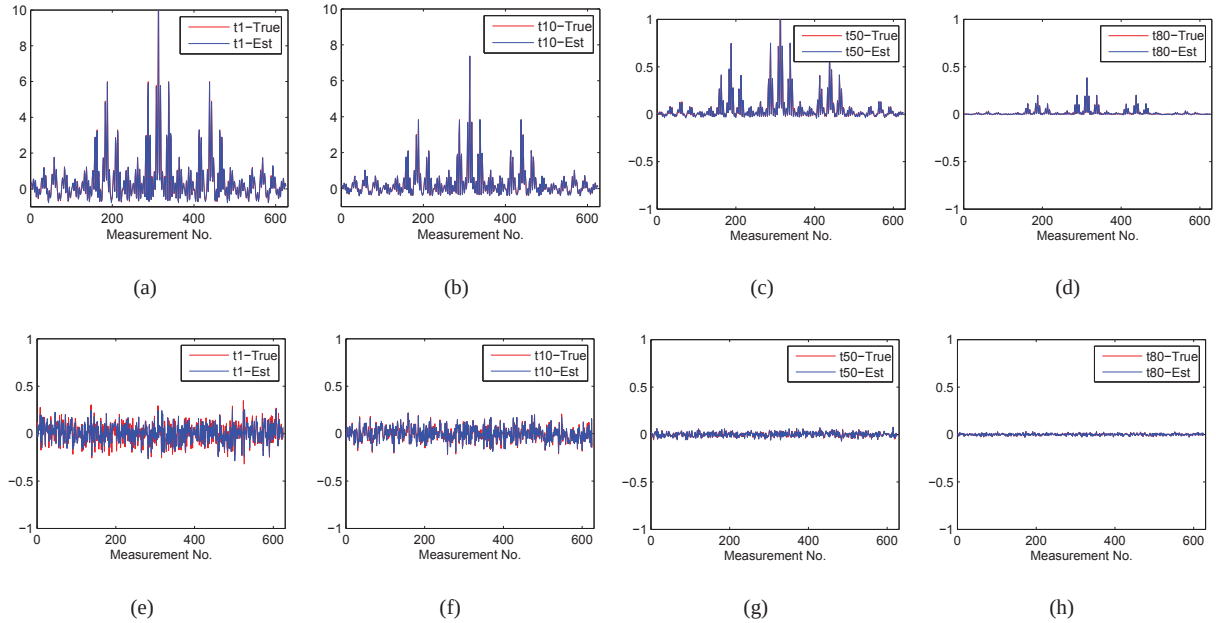

Fig. 4: Single-object case with 10% noise. (a) Recovered Signals (a)-(d). Noise estimated (e)-(h).

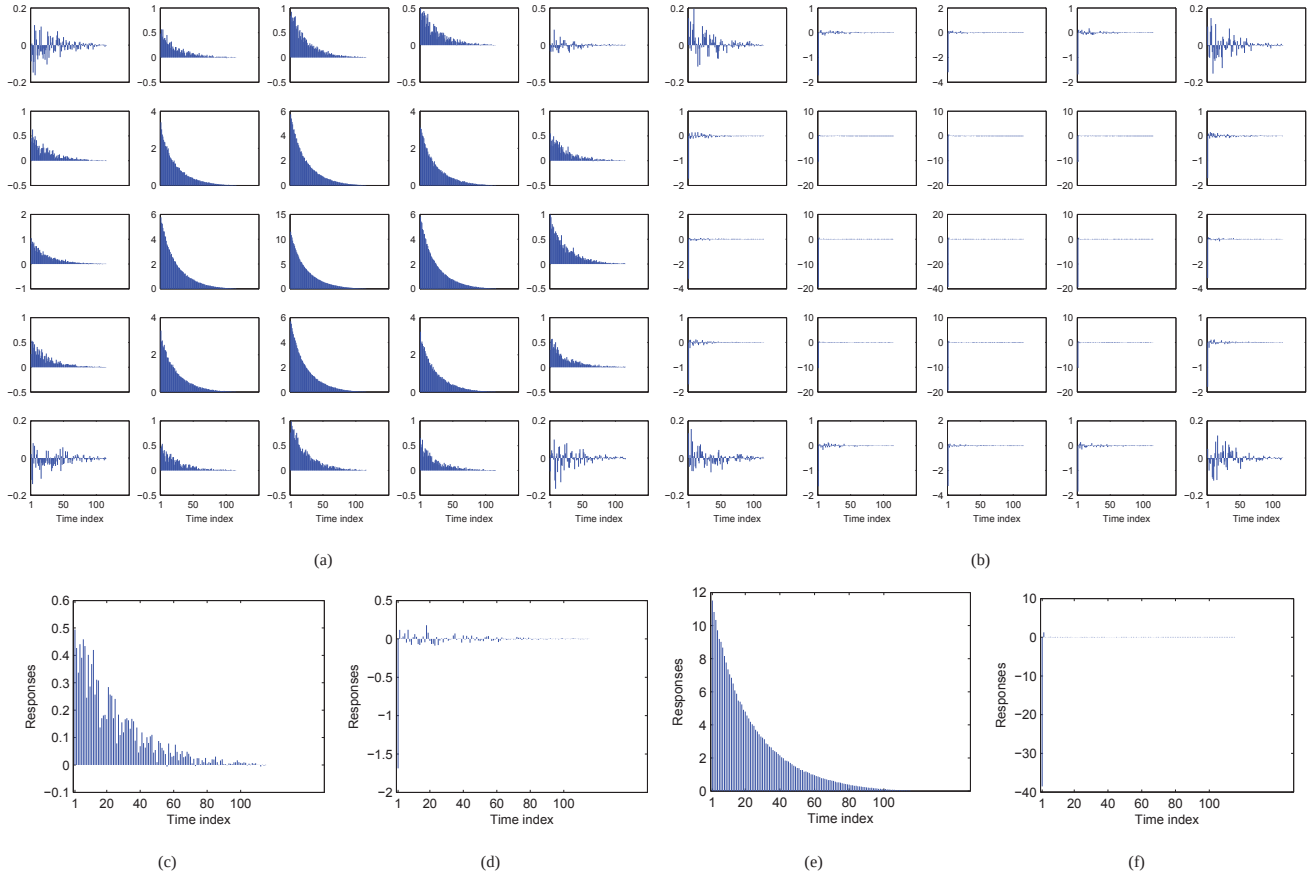

Fig. 5: Single-object case. 10% Noise. (a) Original data with Tx-13 excitation. (b) Projected data with Tx-13 excitation. (c)-(d) Original and projected data of Tx-13/Rx-4 pair. (e)-(f) Original and projected data of Tx-13/Rx-13 pair.

Turning to the TOPI based on Eq. (23), we carry out the inversion using 1, 2, 3, and 5 projected channels (e.g., for 5 projected channels using a subspace of $[\mathbf{v}_1, \cdots, \mathbf{v}_5]$ for the 10% noise case. All returned same exact results $\mathbf{r} = (0.00, -0.00, -0.60)$ m. To understand how these TEVs play a role in the inversion. We did the TOPI using the projected channel at $\mathbf{v}_2$ and obtain $\mathbf{r} = (0.00, -0.01, -0.60)$ m. This is almost the exact location as $\mathbf{v}_2$ is a signal eigenvector. However, the use of projected channel at $\mathbf{v}_3$ gives $\mathbf{r} = (0.61, 1.00, -1.20)$ m that is far from the exact one as it is noise vector. Removing $\mathbf{v}_1$, we conducted the TOPI using the two subspaces of $[\mathbf{v}_2, \mathbf{v}_3]$ and $[\mathbf{v}_2, \cdots, \mathbf{v}_5]$, respectively. Both delivered the location at $\mathbf{r} = (0.00, -0.01, -0.60)$ m. The experiments demonstrate that the TOPI is stable whenever signal vectors are used to project data.

B. Synthetic two-object example

For a two-object example, we set up a shallow object at $\mathbf{r}_2 = (0.03, -0.01, -0.09)$ and a deep object of 105 mm projectile at $\mathbf{r}_1 = (0, 0, -0.60)$ m. That shallow object represents a scrap whose polarizabilties (dashed curves) are shown in Fig. 1 (b). Again different level of Gaussian noise has been added to the data prior to input into the SVD. Fig. 6 shows the singular values. For an ideal noise-free case, we do see in Fig. 6 (a) that the number of larger singular values is 5, being the number of 5 distinct polarizabilties from a symmetric ordnance and a scrap. Also, the numerical singular values agree well with the analytical ones. In Fig. 6 (e), the first 5 singular vectors are smooth and progressively display more zero crossings and the other singular vectors behave randomly. Based upon these eigen characteristics, one can define that the maximal dimension of the signal subspace is 5 in this case. However, the ideal subspace can be distorted with some amount of noise. As shown in Figs. 6 (b)-(d), amount of $3\% \sim 10\%$ noise makes the noise singular values comparable or even larger than those smaller signal singular values. Correspondingly, the singular vectors in Fig. 6 (f) associated with the 3 small signal singular values become oscillatory and behave like noise eigenvectors. Therefore in these noisy examples, the effective rank or the reduced signal subspace of the data D is 2 in terms of the significant singular values and smooth eigenvectors. The experiment illustrates that one should be cautious to infer the number of objects using singular value spectrum in practice.

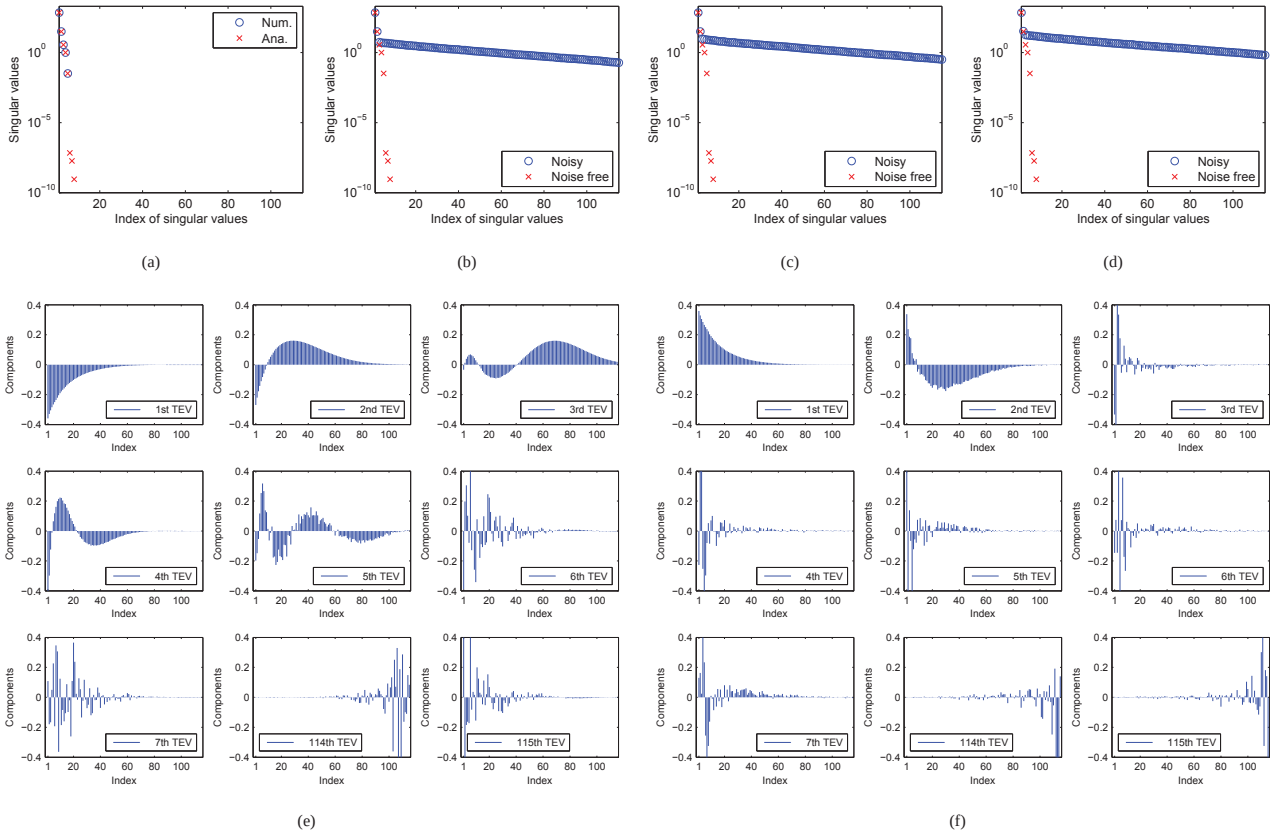

Fig. 6: Two-object case. Singular values: (a) Noise free; (b) 3% noise; (c) 5% noise; (d) 10% noise. Singular vectors: (e) Noise free; (f) 10% noise.

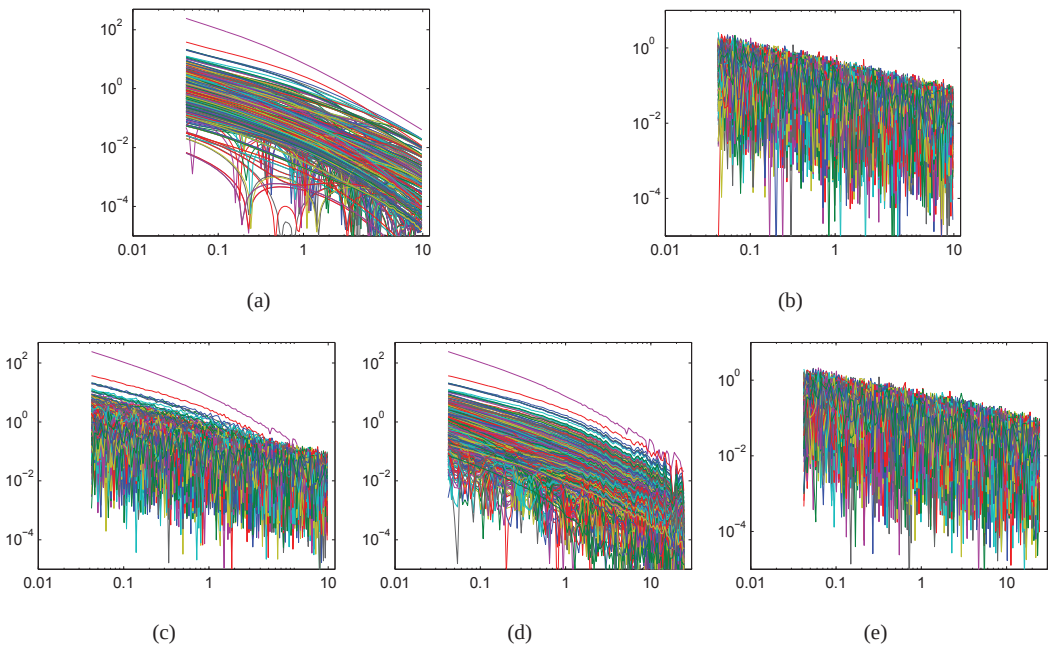

Fig. 7: Two-object case. (a) Signals. (b) Noise 10%. (c) Signals + noise. (d) Estimated signal. (e) Estimated noise.

Like a single-object case, using the effective rank of 2 we tested to reconstruct the data for the 10% noise case using $D = \sum_{i=1}^{2} \sigma_{ii} \mathbf{u}_i \mathbf{v}_i^T$ and estimate noise as $N = \sum_{i=3}^{115} \sigma_{ii} \mathbf{u}_i \mathbf{v}_i^T$ in Fig. (7). Comparing to noise-free signals in Fig. 7(a) with the reconstructed one in Fig. 7(d), we notice that the some amount of additive noise has been removed. When projecting the data onto the temporal base space, we observe the similar concentrated characteristics (Fig. 8) as in the single-object example.

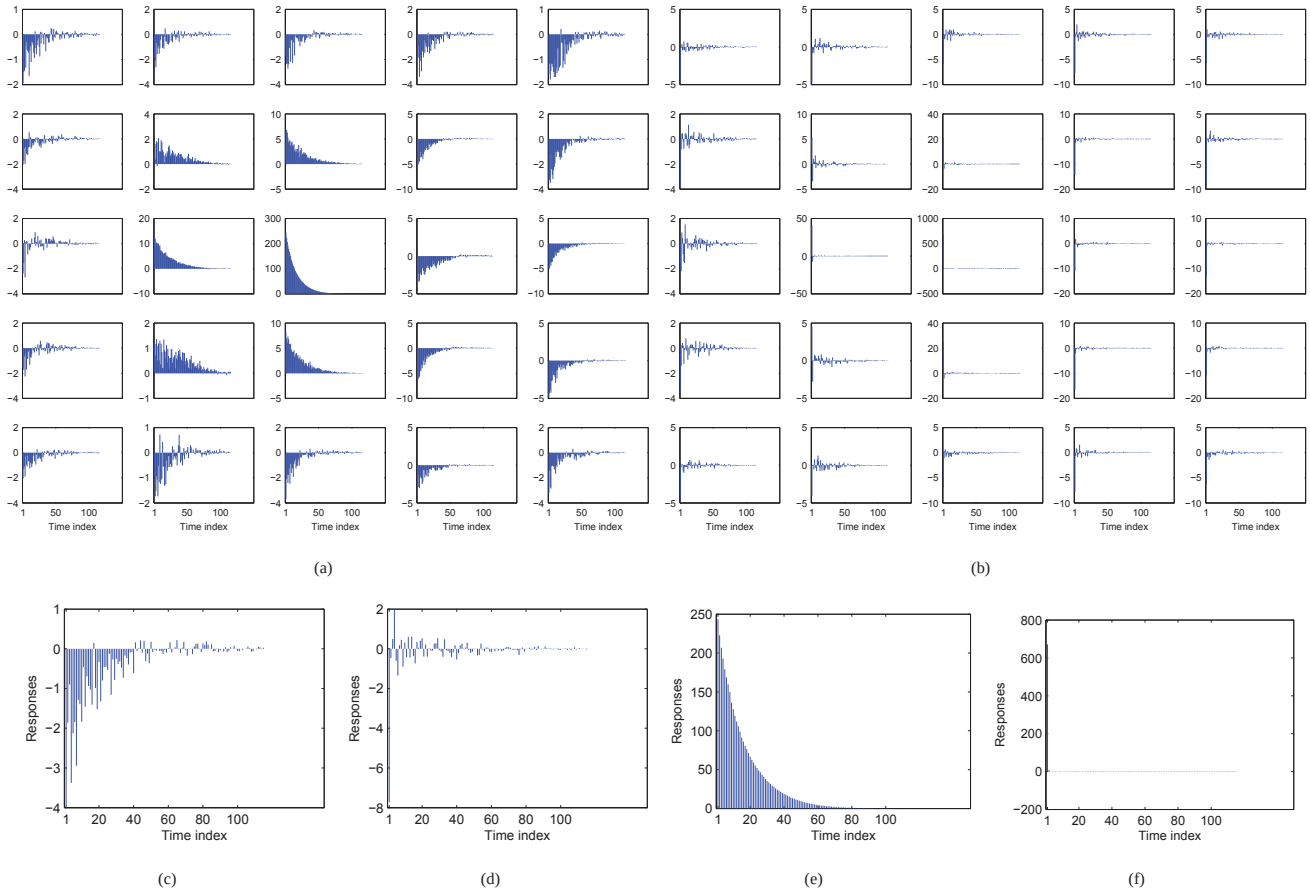

Fig. 8: Two-object case. 10% Noise. (a) Original data with Tx-13 excitation. (b) Projected data with Tx-13 excitation. (c)-(d) Original and projected data of Tx-13/Rx-4 pair. (e)-(f) Original and projected data of Tx-13/Rx-13 pair.

For testing the TOPI, we use 1, 2, 5, 10 TEVs vectors to project 10% noisy data, respectively. All inversions give the exact results at $\mathbf{r}_1 = (0.00, -0.00, -0.61)$ m and $\mathbf{r}_2 = (0.03, -0.01, -0.09)$ m. Referring to Fig. 6 (f), we test the TOPI using the projected channel at $\mathbf{v}_2$ and get $\mathbf{r}_1 = (0.02, 0.02, -0.61)$ m and $\mathbf{r}_2 = (0.04, -0.02, -0.08)$ m that is close to the true locations. When using $\mathbf{v}_3$ in the TOPI, we have $\mathbf{r}_1 = (0.43, -0.81, -0.72)$ m and $\mathbf{r}_2 = (0.43, -0.81, -0.72)$ m as expected since $\mathbf{v}_3$ is a severely contaminated signal vector.

For this noisy case, we run the inversion in original data with 39 channels. It took 1.20 minutes to get $\mathbf{r}_1 = (0.00, -0.01, -0.35)$ m and $\mathbf{r}_2 = (0.14, -0.01, -0.02)$ m, which are incorrect locations. We run the TOPI with the 39 projected channels. It took 0.13 minutes to obtain the exact locations at $\mathbf{r}_1 = (0.00, -0.00, -0.61)$ m and $\mathbf{r}_2 = (0.03, -0.01, -0.09)$ m. The experiment shows that the TOPI is potentially not only accurate but also fast.

With sufficient basic understanding of the technique, next we proceed with a real data example.

C. Real data example

For a real data example, we use the test-pit data acquired with a 105-HEAT. The object was oriented nose down and centered below the sensor array. The previous study [30] showed that this large, vertically oriented object is better represented by a two-object model.

Fig. 9 (a) shows the $\log \sigma_{ii}$ versus their index. There is a long tail of steadily decreasing singular values which are reflective of the noise. However in this practical case, the noise may not be purely Gaussian and its part may be due to an approximate modelling. Like in the synthetic noisy examples, a transition is smooth from large singular values to smaller ones. There is no clear gap between the large and long tail of small singular values. The question is to ask what the number of projected channels should be used if being based upon the analysis of that singular value spectrum .

Suppose we have two objects. Then the maximum r is 6 so there is no sense in exceeding that. Also, it is argued that there is an axis symmetric body and another body. That makes the maximum rank 5 like in the two-object synthetic example. There might be a numeric way to determine a value of r used in the projection. In a singular value-index space of Fig. 9 (a), we can roughly find a elbow point where singular values and their slopes start to change a pattern and take the correspondent index as r. In this example, $r = 7$ is found as marked with a cross in Fig. 9 (a). This number is slightly larger than $r = 5$, or 6 assumed using physics of the problem.

On the other hand, let us examine temporal eigenvectors. Fig. 9 (b) presents the first seven and the last two TEVs. Similar to the observation in synthetic cases, one sees that the TEVs become more oscillatory as the temporal index increases. For the first three TEVs, the number of their sign changes is exactly the number of indices 1, 2 and 3. The last two TEVs are only sensitive to components at late temporal index. The first TEV remains in a constant sign and the subsequent TEVs vary. This TEV behavior makes projected signals concentrated and boosted relative to the original data and those at large temporal index, as seen in Fig. 10. From the regularity of the TEVs picture we may infer the dimension of the reduced signal subspace is $r = 3$.

Fig. 10 (a) shows the original data when Tx-13 was fired (the center transmitter, see Fig. 1(a)). The data measured at those center receivers are smooth decay and the data at edge receivers behave fluctuated and noisy. From Fig. 10

(a), it seems not direct or clear where to cut off time channels for an inversion processing. To obtain the projected data, we project $D_{625\times 115}$ onto the temporal basses $V = [\mathbf{v}_1, \cdots, \mathbf{v}_{115}]$ (Eq. (21)). Fig. 10 (b) shows the projected data. As expected from our synthetic analysis the maximum amplitude data are associated with the first few singular vectors, and in particular, the first one. What one can observe is that (1) the projected data are highly compressed in the temporal base space; (2) The projected signals at very early temporal index are boosted and the projected signals at late temporal index are suppressed. To highlight the observation, we zoom in some data in Fig. 10 (c)-(e). Fig. 10 (c) is the recorded data at Rx-1 under Tx-13 excitation. The data are fluctuated and often the responses at some time channels are larger or comparable to the ones at their preceding channels. In contrast to the projected data in Fig. 10 (d), we see that the projected signal at the 1st temporal channel is roughly 3.1 times as large as the maximum amplitude of the original signals and is at least around 13 times as strong as the projected signals at subsequent temporal channels. The similar phenomena is seen at Fig. 10 (e)-(f) where show the recorded and projected data at Rx-13 under Tx-13. In this case, the projected signal at the 1st temporal channel is also about 3.1 times as large as the maximum amplitude of the original signals and is at least around 78 times strong as the projected signals at subsequent temporal channels. This suggests that inversion may be carried out using the projected signal at the first temporal channel. This is further evident if looking back at the singular value spectrum. The amplitudes of singular values contain the information about the importance of the eigenvectors. One notices that the first σ_{11} is around 18 times large as the second largest σ_{22} and dominates over other singular values.

Above, the determination of r was analyzed from a known physics of the problem, singular value distribution, smoothness of the temporal singular vectors, and the projected data. We test the TOPI and its sensitivity to different $r = 1, 2, 3, 5, 7, 10$ when localizing sources. For $r = 1$, we obtained $\mathbf{r}_1 = (0.02, -0.01, -0.61)$ m, $\mathbf{r}_2 = (0.03, -0.01, -0.27)$ m. For other r values, we obtained all identical locations of $\mathbf{r}_1 = (0.02, -0.01, -0.60)$ m, $\mathbf{r}_2 = (0.03, -0.01, -0.26)$ m. For this real data example, the TOPI is robust to the selection of projected channels. The recovered polarizabilities are given in Figs. 11 (a)-(b).

To understand the contribution of TEV to signals, we projected the data onto each individual vector of $\mathbf{v}_j, j = 2, 3, 4, 5, 6, 7$ and performed the TOPI. Table I lists the inverted locations. We see that starting $\mathbf{v}_3$ the location estimate is incorrect. We also conducted the TOPI using the following subspaces, $[\mathbf{v}_2, \mathbf{v}_3]$, $[\mathbf{v}_2, \cdots, \mathbf{v}_4]$, $[\mathbf{v}_2, \cdots, \mathbf{v}_5]$, and $[\mathbf{v}_2, \cdots, \mathbf{v}_7]$, and obtained all the same locations at $\mathbf{r}_1 = (0.03, -0.02, -0.58)$ m, $\mathbf{r}_2 = (0.04, -0.02, -0.20)$ m. Without using $\mathbf{v}_1$, it can have some impact on the location estimate.

Further without using the two major signal vectors $\mathbf{v}_1$ and $\mathbf{v}_2$, the TOPI was carried out with the subspaces $[\mathbf{v}_3, \mathbf{v}_4]$ and returned $\mathbf{r}_1 = (0.48, 0.36, -0.80)$ m, $\mathbf{r}_2 = (0.03, -0.03, -0.20)$ m; $[\mathbf{v}_3, \cdots, \mathbf{v}_5]$ and $\mathbf{r}_1 = (-0.09, -0.50, -1.2)$ m, $\mathbf{r}_2 = (0.04, -0.02, -0.20)$ m; $[\mathbf{v}_3, \cdots, \mathbf{v}_7]$ and $\mathbf{r}_1 = (-0.04, -0.50, -1.2)$ m, $\mathbf{r}_2 = (0.04, -0.02, -0.20)$ m. The experiment seems to show that $\mathbf{v}_3$ mainly contains some information about the location of $\mathbf{r}_2$ not $\mathbf{r}_1$.

Overall, the above tests show that the inclusion of the signal vectors $[\mathbf{v}_1, \mathbf{v}_2]$ is sufficient to recover the locations via the TOPI.

To test the inversion in the original data domain, we use several subsets of time channels with $N_t = 51, 16, 13$. Figs. 11 (c)-(e) present the associated inversion results of the recovered locations and polarizabilities. As one can

TABLE I: TOPI with single $\mathbf{v}_j$ in the real data example

TEV	(x_1, y_1, z_1) (m)	(x_2, y_2, z_2) (m)
$\mathbf{v}_1$	(0.02, -0.01, -0.61)	(0.03, -0.01, -0.27)
$\mathbf{v}_2$	(0.02, -0.02, -0.61)	(0.04, -0.02, -0.15)
$\mathbf{v}_3$	(0.04, -0.33, -0.85)	(0.03, -0.33, -0.21)
$\mathbf{v}_4$	(0.26, 0.26, -0.01)	(0.26, 0.26, -0.01)
$\mathbf{v}_5$	(-0.50, -0.48, -1.20)	(-0.44, -0.50, -1.20)
$\mathbf{v}_6$	(-0.47, -0.50, -1.01)	(-0.47, -0.50, -1.01)
$\mathbf{v}_7$	(0.50, 0.26, -1.20)	(0.08, 0.56, -1.20)

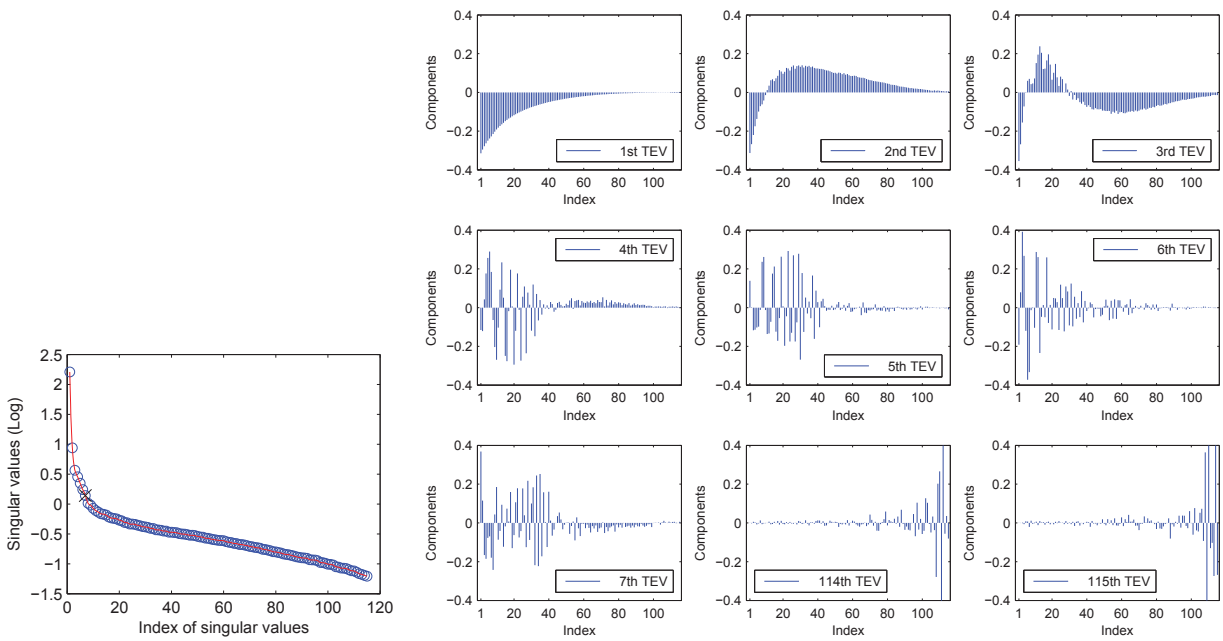

(a) (b)

Fig. 9: Test-pit data. (a) Singular values. (b) Temporal eigenvectors.

see that the inversion can be affected by an selection of channels. An inappropriate selection like $N_t = 16$ in Fig. 11 (d) can lead to some a less accurate result. In contrast, the TOPI offers a way to select the projected channels using signal vectors and was tolerant to the inclusion of noise vectors and was stable. Figs. 11 (a)-(b) shows that the recovered polarizabilities by the TOPI are similar to better than the ones in Figs. 11 (c)-(e).

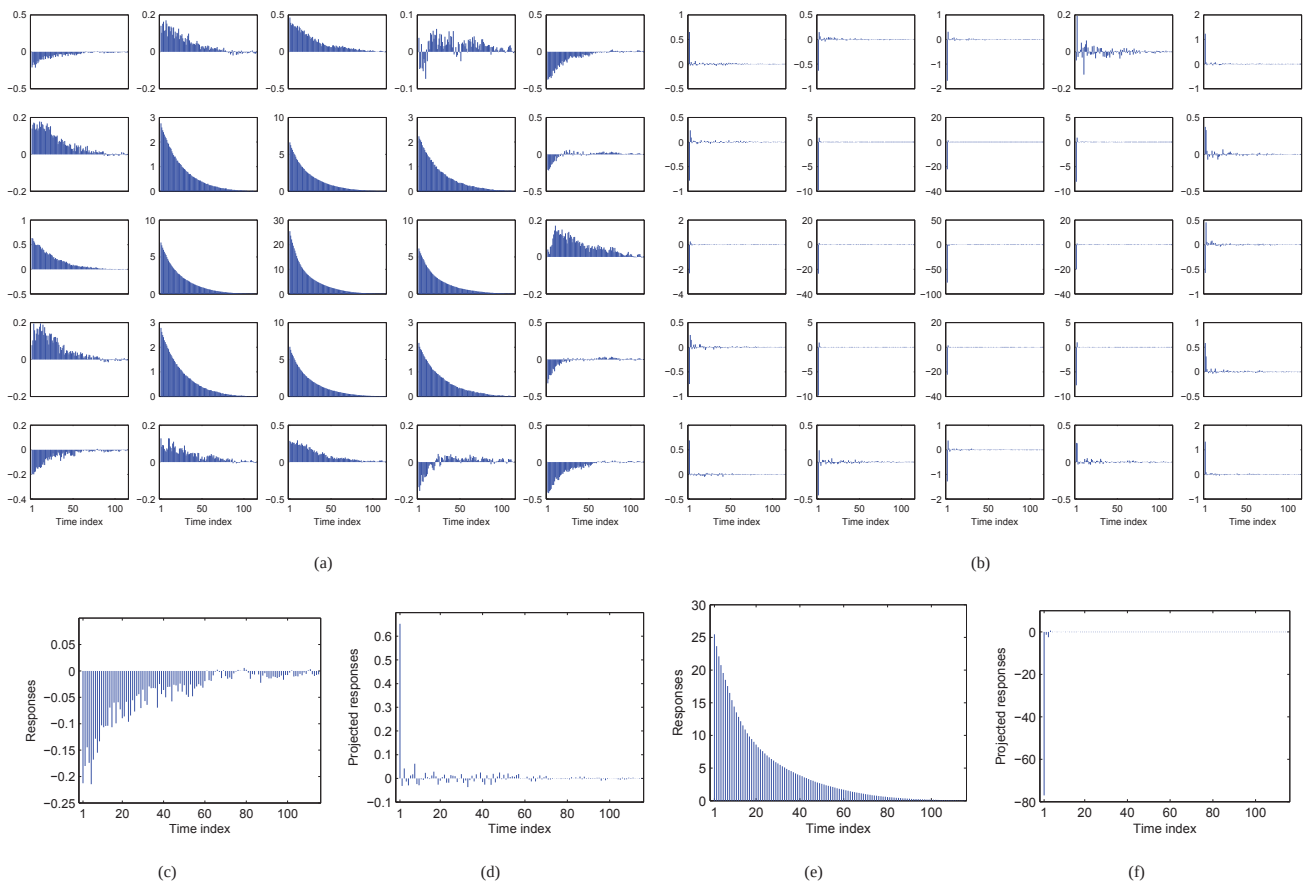

Fig. 10: Test-pit data. (a) Original data with Tx-13 excitation. (b) Projected data with Tx-13 excitation. (c)-(d) Original and projected data of Tx-13/Rx-1 pair. (e)-(f) Original and projected data of Tx-13/Rx-13 pair.

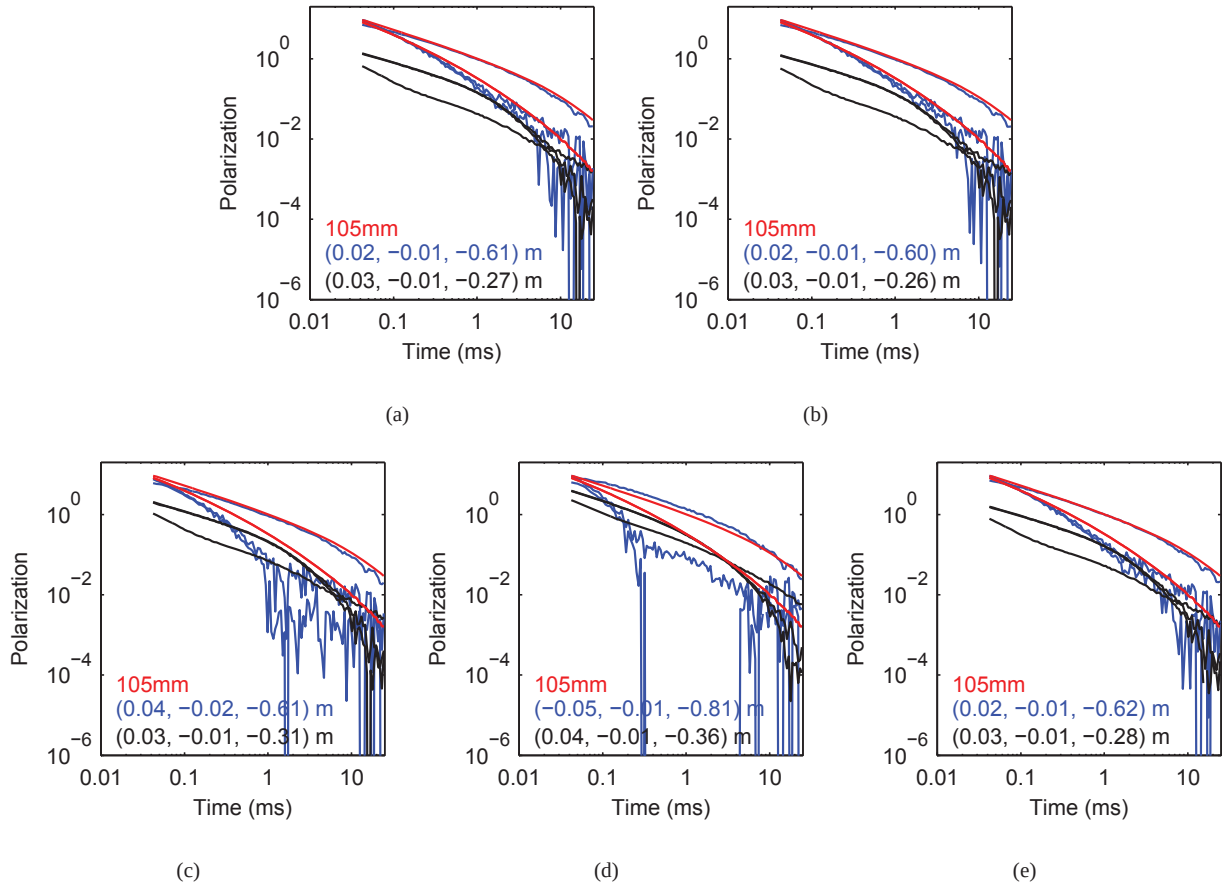

Fig. 11: Test-pit data. TOPI: (a) 1 TEV, (b) 7 TEVs. Inversion of original data: (c) 51, (d) 16, (e) 13. On the polarization plots, the red curves represent the known polarizabilities of 105mm projectile and the blue and black the recovered ones.

V. Conclusions

We have considered the problem of inverting multiple time channel TEM data. The test showed that the accuracy of source localization via a nonlinear inversion can be critically related to responses at selected time channels. An inappropriate channel selection may lead to a poor result.

To address this problem, we propose a temporal orthogonal projection inversion method that circumvents manual channel selection. Briefly, the method has four steps: 1) doing the singular value decomposition (SVD) of the spatial-temporal response matrix (STRM); 2) projecting the STRM onto the temporal signal subspace matrix for a transformed temporal response matrix; 3) carrying out source localizations in the projected temporal domain; 4) obtaining target polarizabilties in the original data domain. The central idea of the TOPI is to convert time channel selection into to a signal subspace problem. Therefore the key step in the method is to determine the number r of temporal signal vectors used for projection. Using synthetic and real TEMTADS data, we have conducted the

detailed analysis and evaluation on the determination of r from several aspects of the singular value spectrum, the temporal eigenvectors, the projected data, the physics of the problem. The most prominent feature we have found is that, owing to the oscillation properties of the TEVs with index, the projected TEM responses can concentrate around a few early temporal indices and the transformed responses are suppressed at subsequent channels. This highly compressed feature makes temporal channel selection easy in the transformed domain. We also tried a heuristic way to find r as the location of maximum curvature in the map of singular values versus their indices. The TOPI returns the almost the same result with either determined r. In other words, the TOPI is robust to the size of a signal subspace.

In comparison with the standard nonlinear inversion method implemented in original time-channel domain, the TOPI can be a potential practical tool that is not only computationally efficient but also is able to produces more accurate results since a substantial portion of the noise in the data is automatically winnowed from the analysis.

REFERENCES

[1] Y. Das, J. E. McFee, J. Toews, and G. C. Stuart, "Analysis of an electromagnetic induction detector for real-time localization of buried objects," *IEEE Trans. Geosci. Remote Sens.*, Vol. 28, 278-287, 1990.

[2] A. Sebak, L. Shafai, and Y. Das, "Near-zone fields scattered by three-dimensinal highly conducting permeable objects in the field of an arbitrary loop," *IEEE Trans. Geoscience and Remote Sensing*, 29, pp. 9-15, 1991.

[3] N. Geng, K. E. Baum, L. Carin, "On the low frequency natural responses of conducting and permeable target," *IEEE Trans. Geoscience and Remote Sensing*, Vol. 37, 347-359, 1999.

[4] B. Barrow and H. H. Nelson, "Model-based characterization of electromagnetic induction signatures obtained with the MTADS electromagnetic array,", *IEEE Trans. Geoscience and Remote Sensing*, Vol. 39, No. 6, 1279-1285, June 2001.

[5] J. T. Miller, T. Bell, J. Soukup, and D. Keiswetter, "Simple phenomenological models for wideband frequency-domain electromagnetic induction, " *IEEE Trans. Geoscience and Remote Sensing*, Vol. 39, No. 6., 1294-1298, 2001.

[6] T. H. Bell, B. J. Barrow, and J. T. Miller, "Subsurface discrimination using electromagnetic induction sensors," *IEEE Trans. Geosci. Remote Sens.*, Vol. 39, 1286-1293. 2001

[7] L. S. Riggs, , J. E. Mooney, and D. E. Lawrence, "Identification of metallic mine-like objects using low frequency magnetic fields," *IEEE Trans. Geosci. Remote Sens.*, Vol. 39, 56-66, 2001.

[8] L. R. Pasion and D.W Oldenburg, "A discrimination algorithm for UXO using time domain electromagnetics," *J. Eng. Environ. Geophys.*, vol. 28, pp. 91-102, 2001.

[9] L. Carin, Yu Haitao; Y. Dalichaouch, A.R. Perry, P.V. Czipott, and C.E. Baum, "On the wideband EMI response of a rotationally symmetric permeable and conducting target," *IEEE Trans. Geoscience and Remote Sensing*, Vol. 39, No. 6, pp. 1206-1213, 2001.

[10] H. Huang and I. J. Won, "Characterization of uxo-like targets using broadband electromagnetic induction sensors," *IEEE Trans. Geosci. Remote Sens.*, Vol. 41, 640-651, 2003.

[11] Y. Zhang, L. Collins, H. Yu, C. Baum, and L. Carin, "Sensing of unexploded ordnance with magnetometer and induction: theory and signal processing," *IEEE Trans. Geoscience and Remote Sensing*, Vol. 41, No. 5, pp. 1005-1015, May 2003.

[12] J. T. Smith and H. F. Morrison, "Estimating equivalent dipole polarizabilities for the inductive response of isolated conductive bodies," *IEEE Trans. Geoscience and Remote Sensing*, vol. 42, No. 6, pp. 1208 - 1214, 2004.

[13] D. D. Snyder, D.C. George, Scott C. MacInnes, and J. Torquil Smith "An assessment of three dipole-based programs for estimating UXO target parameters with induction EM," *SEG*, Las Vegas, 2008.

[14] S. L. Tantum and L. M. Collins, "A comparison of algorithms for subsurface target detection and identification using time-domain electromagnetic induction data," *IEEE Trans. Geosci. Remote Sens.*, Vol. 39, No. 6, 1299-1306, 2001.

[15] A. B. Tarokh, Miller, E. L., Won, I. J., and Huang, H., "Statistical classification of buried objects from spatially sampled time or frequency domain electromagnetic induction data," *Radio Sci*., Vol. 39, RS4S05, doi:10.1029/2003RS002951, 2004.

[16] L. R. Pasion, “Inversion of time domain electromagnetic data for the detection of unexploded ordnance,” Ph.D dissertation, The University of Bristish Columbia, 2007.

[17] A. Aliamiri, J. Stalnaker, E. L. Miller, “Statistical classification of buried unexploded ordnance using nonparametric prior models,” *IEEE Transactions On Geoscience And Remote Sensing*, Vol.45, No. 9, pp. 2794-2806, 2007.

[18] D. Williams, C. P. Wang, X. J. Liao, L. Carin, “Classification of unexploded ordnance using incomplete multisensor multiresolution data,” *IEEE Transactions On Geoscience And Remote Sensing*, Vol. 45, No. 7 pp. 2364-2373, 2007

[19] Q. H. Liu, X. J. Liao, L. Carin, “Detection of unexploded ordnance via efficient semisupervised and active learning,” *IEEE Transactions On Geoscience And Remote Sensing*, Vol. 46, No. 9, pp. 2558-2567, 2008.

[20] E. Gasperikova, and J. T. Smith, and Morrison, H.F. and Becker, A. and Kappler, K, “UXO detection and identification based on intrinsic target polarizabilities,”*Geophysics*, 74, B1-B9, 2009.

[21] S. D. Billings and L. R. Pasion and L. Beran and N. Lhomme and L.-P. Song and D. W. Oldenburg and K. Kingdon and D. Sinex, and J. Jacobson, “Unexploded ordnance discrimination using magnetic and electromagnetic sensors: Case study from a former military site,” *Geophysics*, 75, 3, B103-B114, 2010

[22] L. Beran, B. Zelt, L. R. Pasion, S. D. Billings, K. Kingdon, N. Lhomme, L.-P. Song, and D. W. Oldenburg, “Practical strategies for classification of unexploded ordnance,” *Geophysics*, 78(1), E41-E46, 2013.

[23] T. Bell, “Adaptive and iterative processing techniques for overlapping signatures,” AETC report, 1-16, Mar, 2006.

[24] F. Shubitidze, K. O’Neill K, B. E. Barrowes, I. Shamatava, J.P. Fernndez, K. Sun, K.D. Paulsen, “Application of the normalized surface magnetic charge model to UXO discrimination in cases with overlapping signals Journal of Applied Geophysics,” *Journal of Applied Geophysics*, Vol. 61, No.3-4, 292-303, 2007.

[25] Shubitidze F., D. Karkashadze, J. P. Fernndez, B. E. Barrowes, Kevin O’Neill, T. M. Grzegorczyk, I. Shamatava, “Applying a volume dipole distribution model to next-generation sensor data for multi-object data inversion and discrimination,” *Proceedings of the SPIE*, 7664,7664071-76640711, 2010.

[26] J. T. Miller, D. Keiswetter, J. Kingdon, T. Furuya, B. Barrow and T, Bell,“Source Separation using Sparse-Solution Linear Solvers,” *Proceedings of the SPIE*, 7664, 766409-1-766409-8, 2010.

[27] L.-P. Song, D. W. Oldenburg, L. R. Pasion, and S. D. Billings, “Transient electromagnetic inversion of multiple targets,” *SPIE*, Vol. 7303, pp. 73030R-73030R12, 2009.

[28] L.-P. Song, L. R. Pasion, S. D. Billings, D. W. Oldenburg, “Non-linear Inversion for Multiple Objects in Transient Electromagnetic Induction Sensing of Unexploded Ordnance: Technique and Applications,” *IEEE Trans. on Geosciences and Remote Sensing*, Vol. 49, No. 8, pp. 4007-4020, 2011.

[29] T.M. Grzegorczyk, B.E. Barrowes, F. Shubitidze, Fernndez, J.P., O’Neill, K., “Simultaneous identification of multiple unexploded ordnance using electromagnetic induction sensors,” *IEEE Transactions on Geoscience and Remote Sensing*, Vol. 49, 2507-2517, 2011.

[30] L.-P. Song, L. R. Pasion, and D. W. Oldenburg, “Estimating source locations of unexploded ordnance using the multiple signal classification algorithm,” *GEOPHYSICS*, VOL. 77, NO. 4, WB127-WB135, 2012.

[31] F. Shubitidze, J. P. Fernndez, I. Shamatava, B. E. Barrowes, and K. ONeill, “Joint diagonalization applied to the detection and discrimination of unexploded ordnance,” *GEOPHYSICS*, VOL. 77, NO. 4, WB149-WB160, 2012.

[32] Nelson, H. H., “EMI Array for Cued UXO Discrimination,” ESTCP MM-0601, May, 2008.

[33] F. S. Grant and G. F. West, *Interpretation Theory in Applied Geophysics*, section 6.5, McGraw-Hill Inc.,1965.

[34] J. D. Jackson, *Classical Electrodynamics*, pp.180-182, 2nd ed: New York: Wiley, 1975.

[35] R. A. Horn, C.R. Johnson, *Matrix Analysis*, pp.402-404, Cambridge University Press, 1985.

[36] G. H. Golub and C. F. Van Loan, *Matrix Computations*, pp.139-147, 2nd ed: Johns Hopkins Press, 1989.

A.2. **Detecting and classifying UXO.**

L. S. Beran, B. C. Zelt, S. D. Billings (2013). Detecting and classifying UXO. Journal of Explosive Remnants of War and Mine Action, 17.1, pp. 57-62.

Detecting and Classifying UXO

This article presents state-of-the-art unexploded ordnance detection and classification, including examples from recent field-demonstration studies. After reviewing sensor technologies, with a focus on magnetic and electromagnetic systems, the authors discuss advanced processing techniques that allow for reliable discrimination between hazardous ordnance and harmless metallic clutter. Finally, the article shows results from a large-scale field demonstration conducted in 2011. In this case study, electromagnetic data acquired with an advanced sensor is used to identify ordnance at the site, reducing the number of excavations required with conventional metal detectors by 85%.

by Laurens Beran [Black Tusk Geophysics Inc. and the University of British Columbia], Barry Zelt and Stephen Billings [Black Tusk Geophysics Inc.]

The extent of global unexploded ordnance contamination has motivated research into improved technologies for unexploded ordnance detection and classification. In particular, the U.S. Department of Defense's Environmental Science Technology Certification Program has funded the development of sensors and data-processing techniques specially designed to reliably identify buried UXO.

As part of this research effort, ESTCP conducted a series of field demonstrations to validate detection and classification technologies. The first demonstration, conducted in 2010 at Camp Sibert, Alabama (U.S.), required the discrimination of large 4.2-in mortars from metallic ordnance debris.[1] Subsequent demonstrations progressively increased in difficulty. For example, the 2011 Camp Beale demonstration (Marysville, California, U.S.) required the identification of small 37-mm projectiles and fuzes in rigorous terrain. Throughout the demonstration program, a number of participants achieved near-perfect UXO identification.[1,2,3,4]

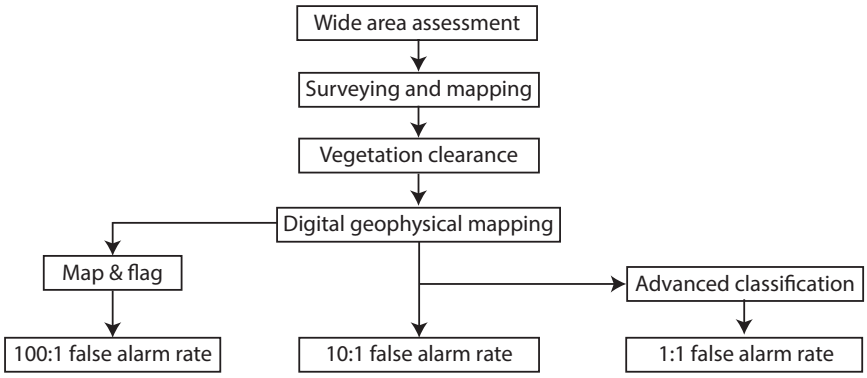

Figure 1. Flowchart for remediation of UXO. Wide area assessment identifies areas of likely UXO contamination at a site, followed by detailed mapping to delineate survey areas. Vegetation must also be cleared to allow deployment of sensors for detection of buried metal. Projected false-alarm rates for remediation strategies (mag and flag, digital geophysical mapping and advanced classification) are for typical munitions response sites within the United States. *All graphics courtesy of the authors.*

Detection

Figure 1 depicts paradigms for detection and classification of buried UXO. The conventional **mag-and-flag** approach uses metal detectors operated by expert technicians to identify targets, which are then flagged for subsequent digging. No digital data are recorded, and changes in an audio tone usually indicate detection. This method is not consistent because success depends upon the operator's skill. In addition, the mag-and-flag approach offers limited possibility for discrimination between hazardous ordnance and clutter. Although the projected cost of this approach is prohibitively high (Figure 1), the mag-and-flag approach will always have a role in UXO clearance—primarily to survey areas inaccessible to other sensors (e.g., around trees, in gullies) and as a first stage clearance of highly cluttered areas.

The second mode of UXO detection, **digital geophysical mapping**, uses geophysical sensors connected to a data-acquisition system to record digitized data acquired over a survey grid. DGM data are subsequently processed to identify high priority targets, which are likely to be buried ordnance. Simple processing techniques, such as digging detected targets based on the measured data's amplitude, can reduce the number of false responses to approximately 10 non-UXO per UXO excavated. Applying advanced classification methods to digital geophysical data further reduces the rate of these false responses and greatly increases confidence of successful ordnance clearance. In a technical report published by the U.S. Office of the Undersecretary of Defense for Acquisition, Technology and Logistics, Delaney and Etter estimate the cost of UXO remediation projects within the U.S. at US$52 billion with mag and flag, versus $16 billion with advanced classification.[5]

Magnetic and electromagnetic geophysical data types are most commonly acquired for UXO detection and discrimination. Magnetic instruments are used to measure distortions in the Earth's geomagnetic fields produced by magnetically susceptible materials (e.g., steel). Magnetic sensors deployed for UXO detection typically either measure the total magnetic field (scalar measurement) or the difference between two closely spaced magnetometers, measuring

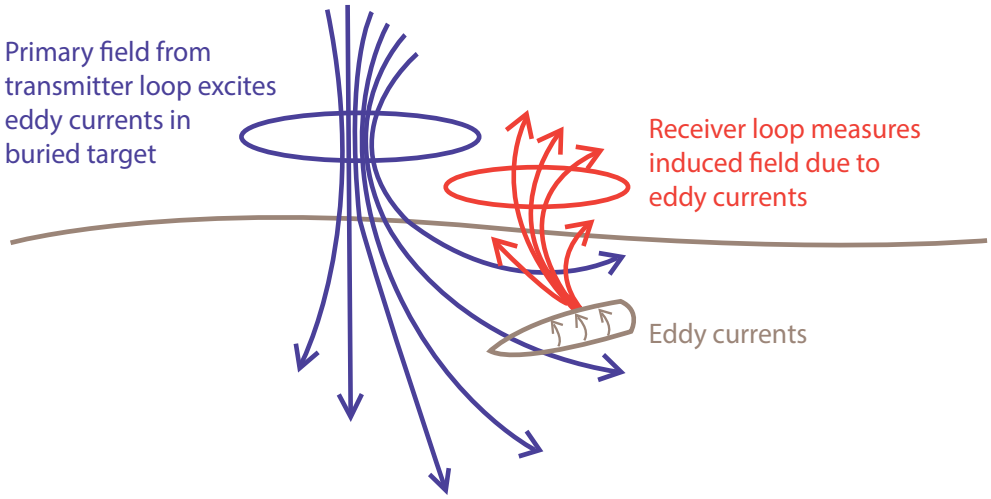

Figure 2. Electromagnetic induction survey. Eddy currents are induced in a buried target by a time-varying primary field. Decaying secondary fields radiated by the target are then measured by a receiver at the surface.

the vertical component of the magnetic field (gradiometer measurement). Magnetic-sensor arrays have been deployed for helicopter-borne surveys (**heli-mag**) in wide-area assessments.[6] Multiple magnetometers can also be arranged in arrays for ground-based surveying, using wider swaths to decrease the number of passes required to cover a given area. A significant background soil response, which can obscure identification of discrete targets in the measured signal, often complicates the processing of magnetic data. In addition, magnetic data can only provide limited information about intrinsic target properties (i.e., size and shape) and are rarely used to classify detected targets as UXO and non-UXO.[7] Therefore, the remainder of this article focuses on classification with electromagnetic data.

Processing of electromagnetic data produces a unique intrinsic response (or fingerprint) for each target, which can then be matched with responses for known ordnance types. As depicted in Figure 2, electromagnetic instruments actively transmit a time-varying, primary magnetic field that illuminates the Earth. The variation of the primary field induces currents in the ground, and these currents produce a secondary field that a receiver on the surface can measure. EM sensors measure the decay of these secondary fields after the primary field is switched off. The secondary fields, in turn, provide information regarding electrically conductive items in the ground.

EM sensors designed for UXO applications come in a wide variety of geometries, ranging from cart systems with multiple transmitters and receivers to single loop, man-portable systems. The Geonics EM-61, an ubiquitous time-domain instrument, transmits from a single horizontal coil. When the primary field is terminated, the EM-61 measures the decaying secondary field in a horizontal receiver loop at four discrete time channels. This instrument is robust, easy to use and consequently, popular for UXO detection and other environmental applications. However, the range of time channels is fairly short, and the paucity of receiver and transmitter combinations (relative to newer systems) limits this instrument's classification capability.

Table 1 shows EM sensors, which have been applied to UXO detection and classification problems. This is not a comprehensive list of EM sensors, but is intended to illustrate the recent evolution of sensors from few channels to many channels over a long period of time and the shift toward configurations with multiple transmitters and receivers.

Two types of surveys, or search patterns, are common with EM instruments.[6] A detection-mode survey passes the sensor over an area along closely spaced parallel lines, typically such that adjacent sensor passes are between 50 and 100 cm apart. Sometimes perpendicular lines are also acquired to maximize data coverage over targets and ensure their illumination from multiple angles. The data are acquired approximately every 10 cm along each line. Towed arrays of EM sensors can quickly cover large areas, while single-sensor pushcart systems are much slower. Pushcart or man-portable EM systems are therefore better suited to the cued-interrogation mode of surveying. In this mode, a DGM survey initially identifies anomalies, and high fidelity data are subsequently acquired over each target. Recently developed systems for stationary cued interrogation (e.g., MetalMapper and TEMTADS, Table 1) illuminate the target with multiple transmitters and receivers, thereby circumventing the requirement for accurate positioning of moving sensors.

Classification

Once a digital geophysical map with a ground-based sensor is acquired, a number of processing steps are required to produce a prioritized dig list of targets for excavation. Figure 3 shows the typical processing involved in advanced classification.

Target selection identifies anomalies in the digital geophysical map down to a pre-defined amplitude threshold. The threshold is usually based upon the minimum expected data amplitude for the smallest target of interest (i.e., UXO) at a site. All designated targets are then revisited to acquire cued-interrogation data from each one.

Each designated anomaly is characterized by estimating features from the cued data, which subsequently allows a data analyst to discern UXO from nonhazardous clutter. These features may directly relate to the observed data (e.g., anomaly amplitude at the first time channel), or they may be the parameters of a physical model. The former approach is appealing in its simplicity but is generally not an effective strategy for classification. An ordnance item at depth will produce a small anomaly amplitude and might be left in the ground with a dig list based solely upon anomaly amplitude. Most classification strategies therefore use physical modeling to resolve such ambiguities.

Bell et al., Pasion and Oldenburg, and Zhang et al. give detailed descriptions of the physical modeling used for processing EM data.[8,9,10] In the feature estimation stage, these models are fit to the observed EM data for each target anomaly. This fitting is analogous to fitting a straight line to data via least-squares regression. In that case the model is parameterized by slope and intercept; here the model is parameterized by target location,

Sensor	Geometry	Time channels
EM-61	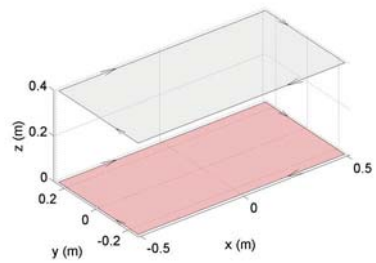	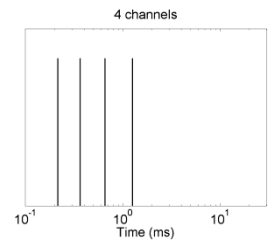
MetalMapper 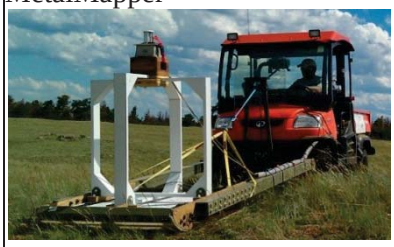	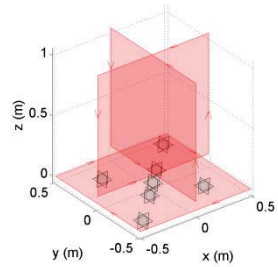	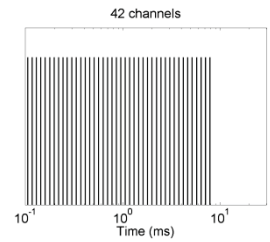
TEMTADS	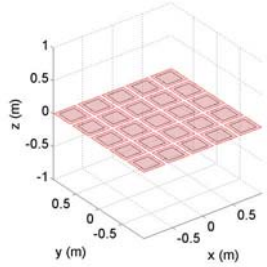	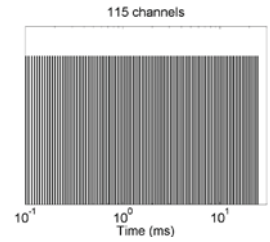
MPV	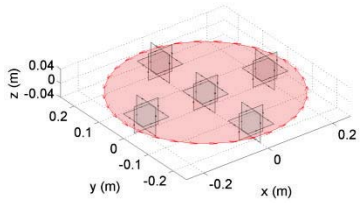	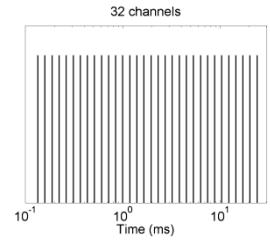
BUD	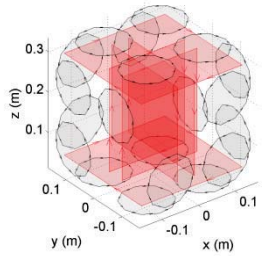	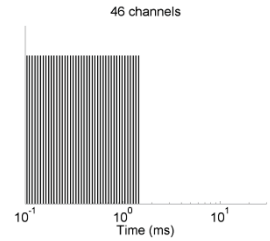

Table 1. Electromagnetic sensors used for UXO detection and classification. Red and black lines in the middle column indicate transmitters and receivers, respectively.

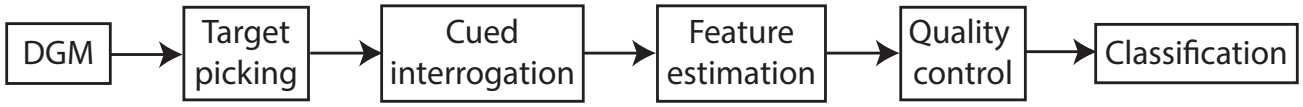

Figure 3. Processing steps for UXO classification.

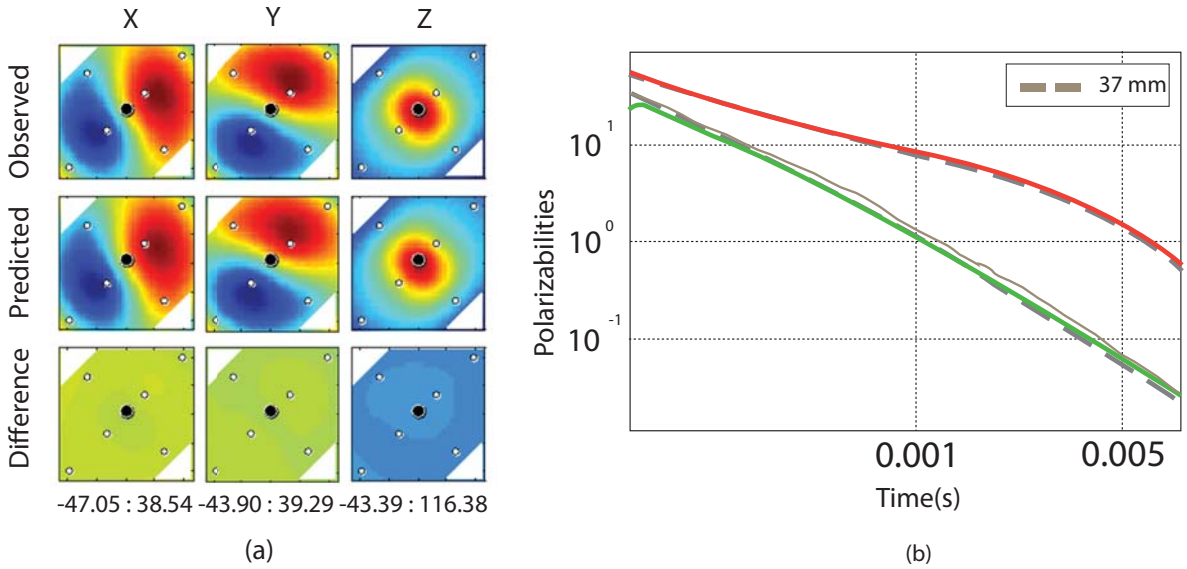

Figure 4. Fitting MetalMapper data. (a) Observed data (top row) and data predicted by fitting a physical model to the observed data (middle row). Bottom row shows the (negligible) difference between observed and predicted data. Each column shows the X, Y and Z components of the measured data, with MetalMapper receiver locations indicated by white circles. The black circle is the estimated location of the target. Numbers at the bottom of each column indicate the range of data values (in arbitrary units). Colored images map blue and red to low and high data values, respectively. (b) Estimated polarizabilities (colored lines) recovered via fitting, overlain on known polarizabilities for 37-mm projectiles. The excellent correspondence between recovered and reference polarizabilities indicates—with high confidence—that the detected target is a 37-mm item.

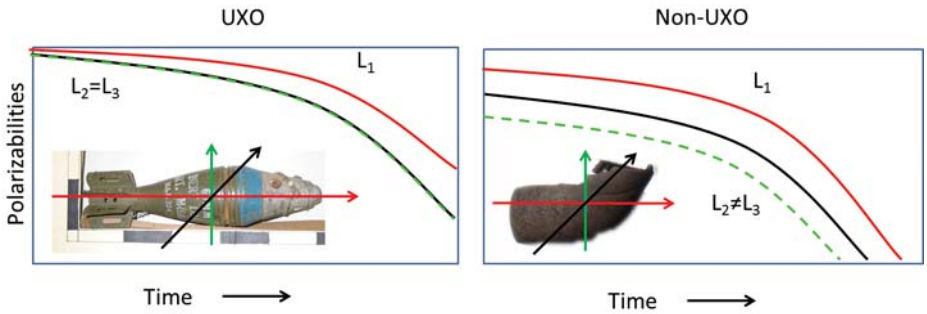

Figure 5. Comparison of representative polarizabilities for UXO and non-UXO items.

orientation and polarizabilities. The polarizabilities are intrinsic to each target and hence classification decisions can be made based on the match of the estimated values to those of known UXO types. Figure 4 shows an example of this fitting procedure and the recovered polarizabilities for MetalMapper data acquired over a 37-mm projectile.

Figure 5 compares typical polarizabilities for UXO and non-UXO items. The primary polarizability (L1) aligns with the long axis of the target. UXO generally have larger amplitude, slower decaying polarizabilities relative to small clutter. Shape information is encoded in secondary polarizabilities (L2 and L3). Most UXO have a circular cross section and will have L2 ≈ L3. In contrast, for irregularly shaped clutter, these parameters differ significantly. These differences in polarizabilities allow for distinction between buried UXO and clutter.

An important step in UXO data processing is visual quality control of the fit to each target. The example in Figure 4 represents the ideal case: a near-perfect fit to the data and an excellent correspondence between the estimated polarizabilities and expected values for the target's class. However, feature estimation is often complicated by neighboring target anomalies or low signal strength from small or deep (> 30-cm) targets. In these particular situations, noise will affect the fitting to the observed data, and may produce unreliable polarizabilities. An additional complication sometimes encountered in data processing can be a strong background soil response superimposed on the target response. Soil compensation algorithms can be applied to the EM data to remove these effects and recover reliable polarizability estimates.[11]

Careful inspection of all fits by expert data analysts is essential to ensure that the field data for each target anomaly can support classification decisions. When data quality is poor for individual targets, the data may be reacquired or, in the worst case, the target must be dug as a precaution. With newer sensor data and careful field practices, the number of anomalies that cannot be analyzed is usually negligible (less than 1% of the total).

Case Study: Pole Mountain

MetalMapper data were collected for an ESTCP demonstration of classification technologies at Pole Mountain, Wyoming (U.S.), in July 2011. The conditions at this site were relatively benign: Soil response was minimal, and little topography or vegetation impeded data collection. A total of 2,370 items were excavated at Pole Mountain, with 160 of these items identified as UXO. The UXO fell into six classes: Stokes mortars, 60-mm mortars, 75-mm, 57-mm and 37-mm projectiles, and small industry-standard objects (see representative photos in Figure 5). While ESTCP dug all targets, the identities of the objects were unknown to the analysts who needed to develop a classification strategy

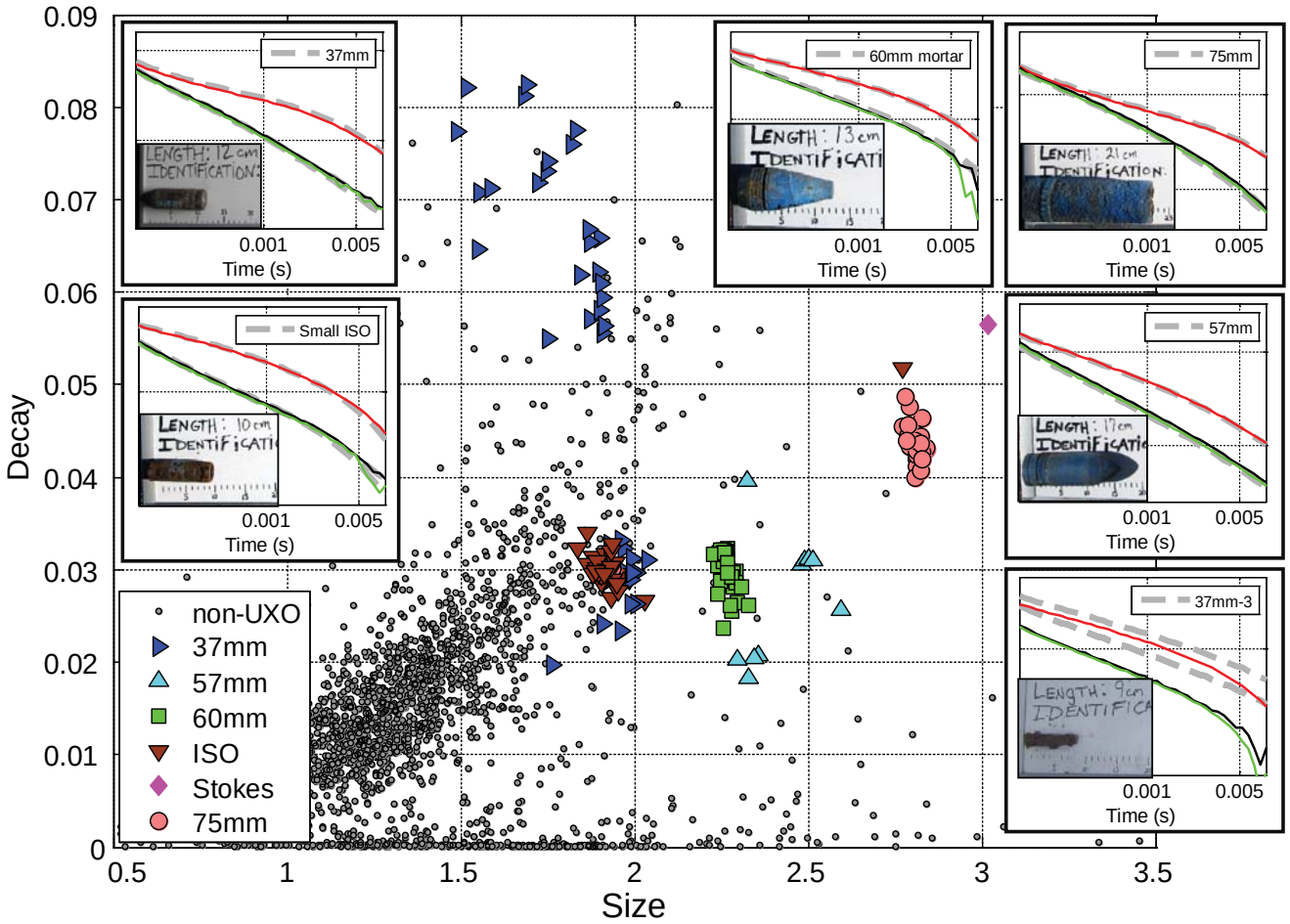

Figure 6. Decay versus size features space for Pole Mountain. Each point represents an individual target, with markers colored based on the similarity of the estimated polarizabilities to known UXO. Insets show estimated polarizabilities for selected targets, with heavy dashed lines indicating the expected reference polarizabilities for that item's class.

and decide which items were potentially hazardous UXO and which were harmless shrapnel or range debris.

Figure 6 shows a plot of size and decay parameters for all Pole Mountain targets. These parameters are computed from each target's estimated polarizabilities and provide a convenient way of visualizing the variability of target properties across the site. UXO are roughly characterized by large amplitude, slow-decaying polarizabilities and cluster in the upper right portion of Figure 6. Clutter items are generally smaller, fast-decaying and cluster near the origin. The degree of overlap between these two clusters dictates the difficulty of the classification task. The Pole Mountain data represents an easy classification task where UXO and non-UXO polarizabilities are readily distinguished. This is illustrated for selected items in Figure 6.

The end product of classification processing is an ordered list of targets prioritized by how well they match the polarizabilities of known UXO. The data analyst also specifies a **stop dig** point in this dig list at which all remaining targets are deemed nonhazardous clutter and can be safely left in the ground. Selecting the stop dig point is crucial to the success of remediation efforts at a site: The analyst must ensure all UXO are found while minimizing the number of unnecessary digs.

At Pole Mountain, a stop dig point that found all 160 UXO was easily chosen, resulting in only 153 non-UXO digs. Figure 7 shows the resulting reduction in digs relative to conventional data processing with the EM-61 instrument. These dramatic savings are typical of results obtained with next-generation sensors such as the MetalMapper, coupled with advanced classification techniques.

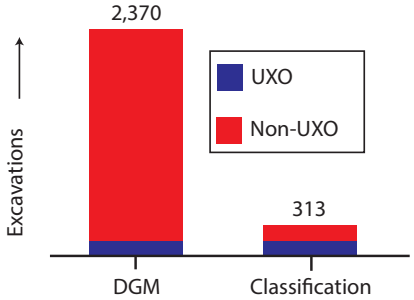

Figure 7. Comparison in total number of targets excavated in order to find all (160) UXO at Pole Mountain, for conventional data processing of a digital geophysical map acquired with the EM-61 and advanced classification with the Metal Mapper.

Conclusions

Sensor and data processing technologies developed under the ESTCP program have repeatedly achieved excellent classification performance in blind field demonstrations. Results depend on the difficulty of the classification task and the quality of the field data. However, improvements in field procedures, including real-time processing of acquired data, are expected to make results similar to those attained at Pole Mountain more routine.

The current ESTCP development emphasis is based on testing smaller, man-portable systems such as the Handheld Berkeley UXO Discriminator (BUDHH) and the Man-Portable Vector Sensor (Table 1 on page 59) and on deploying vehicular sensors to

increasingly challenging sites (higher clutter densities, more varied ordnance types). The man-portable systems can be deployed at challenging sites with variable topography or dense vegetation. Results from the 2011 demonstration at Beale Air Force Base indicate that these systems will provide similar improvements in classification as their larger antecedents.[12]

The large-scale field demonstrations ESTCP sponsored demonstrated the feasibility of significantly reducing the costs of UXO cleanup by deploying advanced sensor technologies coupled with classification algorithms. While the existing set of hardware tends to be heavy, bulky, power-hungry and relatively fragile, some systems have been transitioned to production companies undertaking large-scale UXO remediation projects. Another iteration in hardware development will be required before large numbers of field personnel possess rugged, lightweight and field-ready instrumentation. The future prospects for achieving significant reductions in the costs and time frames required for UXO remediation are extremely promising and worthy of future investment.

See endnotes page 67

The authors would like to acknowledge the Strategic Environmental Research and Development Program and Environmental Security Technology Certification Program for supporting the research and field studies described here. This paper was prepared using funding from SERDP Project MR-1629.

Laurens Beran completed his Master of Science and doctorate degrees in geophysics at the University of British Columbia in Vancouver, Canada. He is a geophysicist with Black Tusk Geophysics and a research associate at UBC. He specializes in development and application of statistical algorithms for UXO classification. Laurens is principal investigator on two Strategic Environmental Research and Development projects examining practical classification techniques.

Laurens Beran
Research Geophysicist
Black Tusk Geophysics
Suite 112A, 2386 East Mall
Vancouver, BC V6T 1Z3 / Canada
Email: laurens.beran@btgeophysics.com
Website:
http://www.btgeophysics.com

Barry Zelt received his Master of Science and doctorate in geophysics from the University of British Columbia. Until recently his world revolved around crustal-scale seismology, but since 2010 he has specialized in UXO detection and classification. He is the primary programmer of Black Tusk's interactive classification software. He is also an experienced user of the software as an analyst of several Environmental Science Technology Certification Program live-site demonstration datasets.

Barry Zelt
Research Geophysicist
Black Tusk Geophysics
Email: barry.zelt@btgeophysics.com

Stephen Billings has more than 16 years of experience working with geophysical-sensor data, including 10 years where he mostly concentrated on improving methods for UXO detection and characterization. He is the president of Black Tusk Geophysics, Inc. and an adjunct professor in Earth and Ocean Sciences at the University of British Columbia. He has been a principal investigator on 10 completed munitions detection-related projects sponsored by Strategic Environmental Research and Development and the Environmental Science Technology Certification Program. He is based in Brisbane, Australia.

Stephen Billings
President
Black Tusk Geophysics
Email:
stephenbillings@btgeophysics.com

Research and Development
CALL FOR PAPERS

The Journal of ERW and Mine Action is seeking submissions for publication in its peer-reviewed Research and Development section. All articles on new and current trends and concepts in R&D will be considered.

Please submit materials to:
Editor-in-Chief, *The Journal of ERW and Mine Action*
Email: cisreditor@gmail.com

For complete submission guidelines:
http://cisr.jmu.edu/journal/index/guidelines.htm

Research and Development Section Sponsored by

A.3. **Practical strategies for classification of unexploded ordnance.**

L. S. Beran, B. C. Zelt, L. R Pasion, S. D. Billings, K. A. Kingdon, N. Lhomme, L. Song, D. W. Oldenburg (2012). Practical strategies for classification of unexploded ordnance. Geophysics, 78, pp. E41 – E46.

Practical strategies for classification of unexploded ordnance

Laurens Beran[*†], *Barry Zelt*[*], *Leonard Pasion*[*], *Stephen Billings*[*], *Kevin Kingdon*[*], *Nicolas Lhomme*[*], *Lin-Ping Song*[†], *Doug Oldenburg*[†]

ABSTRACT

We present practical strategies for discriminating between buried unexploded ordnance (UXO) and metallic clutter. These methods are applicable to time-domain electromagnetic data acquired with multi-static, multi-component sensors designed for UXO classification. Each detected target is characterized by dipole polarizabilities estimated via inversion of the observed sensor data. The polarizabilities are intrinsic target features and so are used to distinguish between UXO and clutter. We illustrate this processing with four data sets from recent field demonstrations, with each data set characterized by a number of metrics of data and model quality. We then develop techniques for building a representative training data set and show how the variable quality of estimated features affects overall classification performance. Finally, we demonstrate a technique to optimize classification performance by adapting features during target prioritization.

INTRODUCTION

Since 2009, the Environmental Science Technology Certification Program (ESTCP) has conducted a series of field demonstrations to test technologies for detection and classification of unexploded ordnance (UXO). Beginning with a relatively simple classification task (identification of large 4.2" mortars at Camp Sibert, Billings et al. (2010)), the demonstrations have progressively increased in difficulty. Most recently, the 2011 Camp Beale demonstration required classification of small items (37 mm projectiles and fuzes) in challenging terrain. Throughout the demonstration program, advanced classification technologies have significantly outperformed conventional approaches (Prouty et al. (2011), Shubitidze et al. (2011), Steinhurst et al. (2010), Billings et al. (2010)). For example, standard classification with Geonics EM-61 sensor data at Camp Beale required excavation of 56% of non-UXO in order to find all UXO (Pasion et al., 2012). In contrast, a typical advanced classification result identified the same set of UXO with only 20% of non-UXO dug. This reduction in false alarm rate results in significant cost savings during site remediation. These successes rely upon:

1. Multi-static, multi-component time-domain electromagnetic (TEM) sensor data. Figure 1 shows the MetalMapper sensor, developed under ESTCP for UXO classification. The sensor is comprised of three orthogonal transmitters and seven receiver cubes measuring the EMF induced by the decaying secondary magnetic field radiated by a buried conductive target (Prouty et al., 2011). Other "next generation" TEM systems designed for UXO classification include: the Time-domain Electro-Magnetic Multi-sensor Towed Array Detection System (TEMTADS, Steinhurst et al. (2010)),

Figure 1: Metalmapper sensor. Left: deployment at Pole Mountain. Right: sensor geometry. Transmitters and receivers are indicated by dashed and solid lines, respectively.

the One-Pass TEM array (OPTEMA, Billings (2011)), the hand-held Berkeley UXO Detector (BUDHH, Gasperikova et al. (2011), and the Man-Portable Vector sensor (MPV, Lhomme (2012)). All of these sensors rely upon multi-static geometries to ensure diverse excitation of the target response.

Most multi-static platforms are deployed in a cued mode: targets identified in an initial detection survey are re-visited and interrogated with a few soundings. For example, the MetalMapper acquires cued data for each target at a single location, ideally directly on top of that target.

2. Advanced processing algorithms to extract intrinsic target parameters from observed TEM sensor data. Most commonly, the TEM dipole model is used to parameterize the response of a confined conductor. The rate of change of the secondary magnetic field ($\mathbf{B_s}$) measured by a sensor is computed as

$$\frac{\partial \mathbf{B_s}}{\partial t}(\mathbf{r}, t) = \frac{p(t)}{r^3}\left(3(\hat{\mathbf{p}}(t)\cdot\hat{\mathbf{r}})\hat{\mathbf{r}} - \hat{\mathbf{p}}(t)\right) \tag{1}$$

with $\mathbf{r} = r\hat{\mathbf{r}}$ the separation between target and observation location, and $\mathbf{p}(t) = p\hat{\mathbf{p}}$ a time-varying dipole moment

$$\mathbf{p}(t) = \frac{1}{\mu_o}\mathbf{P}(t)\cdot\mathbf{B_o}. \tag{2}$$

The induced dipole is the projection of the primary field $\mathbf{B_o}$ onto the target's polarizability tensor $\mathbf{P}(t)$ (Bell et al., 2001). The positive eigenvalues $L_i(t)$ $(i = 1, 2, 3)$ of $\mathbf{P}(t)$ are termed the principal polarizabilities. They are intrinsic to the target and so can be used to make classification decisions.

Estimation of dipole model parameters via nonlinear inversion of observed sensor data is critical to successful classification. Inversion algorithms that handle multi-object scenarios (Bell (2006), Song et al. (2011)) and magnetic soil response (Pasion, 2007) are required to handle the complications encountered in real data. In particular, data acquired over a detected anomaly are always processed with, at a minimum, single and two-object inversions.

The dipole polarizabilities from *all* models are then fed into the subsequent classification stage.

We emphasize that quality control (QC) via careful visual inspection of data fits is necessary to ensure that recovered parameters are reliable. Guided by data and model quality metrics (see table 1), we look for problematic cases where low SNR, neighboring targets, or faulty receivers adversely affect parameter estimation. If an expert analyst decides that no reliable model can be recovered from the observed data, the detected target is labeled as "can't analyze" and must be dug. With good quality data and advanced processing techniques, these cases typically comprise a small proportion ($< 1\%$) of the total number of detected targets.

Classification decisions are made using features derived from estimated dipole polarizabilities. The total polarizability

$$L_{total}(t_j) = \sum_{i=1}^{3} L_i(t_j) \tag{3}$$

can be useful when secondary and tertiary ($L_2,\ L_3$) polarizabilities are poorly constrained. A simple representation in terms of size and decay parameters is similarly useful for visualizing the variability of target features and can give good classification results. These parameters are computed as

$$\begin{aligned} \text{size} &= \log_{10}\left(\sum_{j=1}^{N} L_{total}(t_j)\right) \\ \text{decay}(t_k, t_j) &= \frac{L_{total}(t_k)}{L_{total}(t_j)}, \end{aligned} \tag{4}$$

with N the number of time channels. The decay parameter is usually computed with $t_k > t_j$, so that a smaller value of decay is diagnostic of a faster decaying total polarizability. A logarithmic transformation is applied in the computation of the size parameter to account for the exponential variability of the polarizabilities. In moving from using polarizability features to using only size and decay features, useful classification information may be lost. For example, two targets that are very close in size/decay space may have very different polarizability features. However, as will be demonstrated, a reduced feature set can still provide good classification performance in difficult scenarios where some polarizabilities may be poorly constrained.

Given estimated features, a wide variety of algorithms can be used to classify detected targets. An intuitive, rule-based approach is to rank targets based upon the match of polarizability estimates to a pre-defined library of UXO responses (e.g. Shubitidze et al. (2011)). Alternatively, statistical classifiers can be used to design a decision rule that is some (generally nonlinear) combination of input features (Lee et al. (2007), Benavides et al. (2009), Zhang et al. (2008), Liu et al. (2008)). Regardless of the classification approach, the output of any classifier is a continuous decision statistic that is used to rank targets in the dig list. Note that in the classification stage UXO are often referred to as "targets of interest" (TOI), while metallic clutter is termed non-TOI.

In this paper we examine how estimated dipole polarizabilities can be used to discriminate between UXO and harmless metallic clutter. Inversion and quality control are important prerequisites to this discussion, and detailed presentations of relevant algorithms can be

found in Shubitidze et al. (2011) and Song et al. (2012). Our emphasis here will be on practical and objective classification techniques that have been developed and tested through the course of the ESTCP demonstration program. For brevity we restrict our presentation to MetalMapper data sets from recent ESTCP demonstrations. However, the techniques presented here are generally applicable to classification with dipole polarizabilities derived from arbitrary TEM sensor data.

The remainder of this paper is organized as follows. We first introduce MetalMapper data sets acquired for recent ESTCP demonstrations. We then develop methods for selecting a representative training data set of targets with known ground truth. The training data set is subsequently used to classify the remaining, unlabeled targets. Finally, we explore how the choice of features affects classification performance.

ESTCP METALMAPPER DATA SETS

Table 1 summarizes four MetalMapper data sets acquired for ESTCP demonstrations conducted in 2010 and 2011. For each data set we compute a number of data and model quality metrics:

(a) DS is median data shoddiness - an ad hoc measure of data/model inferiority. DS combines several different measures: (1) data misfit (residual divided by observed); (2) correlation between observed and predicted data; (3) jitter (point-to-point difference) in the observed data; (4) fraction of data above the standard deviation; and (5) size of the difference between secondary and tertiary polarizabilities (L_2 and L_3). Lower values of DS are better.

(b) MSNR is median model signal-to-noise ratio calculated using predicted and residual data - higher values are better.

(c) Pol. Qual. is median polarizability quality - an ad hoc measure of polarizability smoothness and shape - higher values are better.

(d) L123 Msft is the median minimum misfit with all reference items calculated using all three polarizabilities (L1, L2 and L3) - lower values are better.

Decay versus size feature space plots with ground truth information for all data sets are shown in figure 2.

Camp Beale

MetalMapper data were collected at the Camp Beale (California) live site demo (July 2011) by two different production groups: (1) Parsons (P); and (2) CH2M Hill (C). The two groups used the same instrument and, as far as is known, acquisition parameters. Differences in the two data sets should be due primarily to field practices which could, for example, affect the accuracy with which the instrument was centered over an anomaly, or processing approach (such as selection of appropriate background files for background noise subtraction). Total number of anomalies in the Beale data set is 1438 with 131 of these being UXO. The UXO

Dataset	**N (All)**	**N (UXO)**	**DS (All)**	**DS (UXO)**	**MSNR (All)**	**MSNR (UXO)**	**Pol. Qual. (UXO)**	**L123 Msft (UXO)**
Beale P	1438	131	1.42	0.30	40.60	157.00	3.48	0.25
Beale C	1438	131	***1.68***	***0.48***	***17.30***	***146.00***	3.15	0.32
Butner	2304	171	1.20	0.07	60.10	192.00	***2.64***	***0.41***
Pole	2370	160	**0.66**	**-0.69**	**146.00**	**250.00**	**6.78**	**0.12**

Table 1: Data and model quality metrics for MetalMapper ESTCP demonstration data sets. Metrics are described in more detail in the text. All/UXO refers to all anomalies and UXO anomalies, respectively. N is the number of anomalies. Larger font values displayed in **bold** and ***italics*** correspond to the best/worst values for each measure, respectively. Beale P refers to data collected by Parsons at Camp Beale; Beale C refers to data collected by CH2M Hill at Camp Beale using the same instrument.

fall into five classes: (105mm, 81mm, 60mm, 37mm and a small "industry standard object", or ISO). Smaller items such as fuzes are treated as clutter in these data.

By most measures of data and model quality, the Parsons MetalMapper data is slightly better than the CH2M Hill data set (table 1). Even for UXO with the poorest quality data the recovered primary polarizabilities using Parsons data are reasonably accurate with respect to the polarizabilities of the known item based on ground truth. For the CH2M Hill data, however, there are 2 UXO for which the recovered primary polarizabilities do not closely match any reference polarizability.

The generally good separation between UXO and non-UXO in figure 2a suggests that classification should be relatively straightforward for the Beale P data set. For the Beale C data (figure 2b) the separation of TOI from non-TOI items is similar to the Beale P data set, but there are a few challenging TOI that are quite distant from their expected location in feature space.

Camp Butner

The Former Camp Butner (North Carolina) cued MetalMapper data set was collected in September 2010. Two different MetalMapper sensors were used to collect data. About 60 percent of the anomalies were collected with an older instrument that produced measurably poorer quality data than the newer instrument, in part because some of the receiver/transmitter components tended to malfunction. A fairly large number of the anomalies (15 percent) were recollected. Total number of anomalies in the Butner data set is 2304 with 171 of these being UXO. The UXO fall into three classes: (105mm, 37mm and large M48 fuzes). By some objective measures the Butner data are better than the Beale data, but the recovered models for UXO tend to be poorer in quality, resulting in larger misfits with respect to reference items (table 1). Relative to the Beale data sets, some of the UXO in figure 2c (fuzes and fast-decaying 37mm projectiles) overlap the main cluster of non-UXO, suggesting that classification will be more challenging.

Pole Mountain

Finally, the Pole Mountain (Wyoming) cued MetalMapper data set was collected in July-August 2011. By any objective measure, the quality of this data set is excellent and is superior to both the Beale and Butner data sets (table 1). The good separation between UXO and non-UXO and tight clustering of the UXO in figure 2d attest to the high quality of the data set, and suggest that classification should not be too difficult, especially compared to the more difficult Butner data set. The total number of anomalies in the Pole Mountain data set is 2370 with 160 of these being UXO. The UXO fall into six classes: (Stokes mortar, 75mm, 60mm mortar, 57mm, 37mm and small ISO). In the original analysis this data set was divided into two parts, representing a 2 year study. For the purposes of this retrospective study, we use the combined data set.

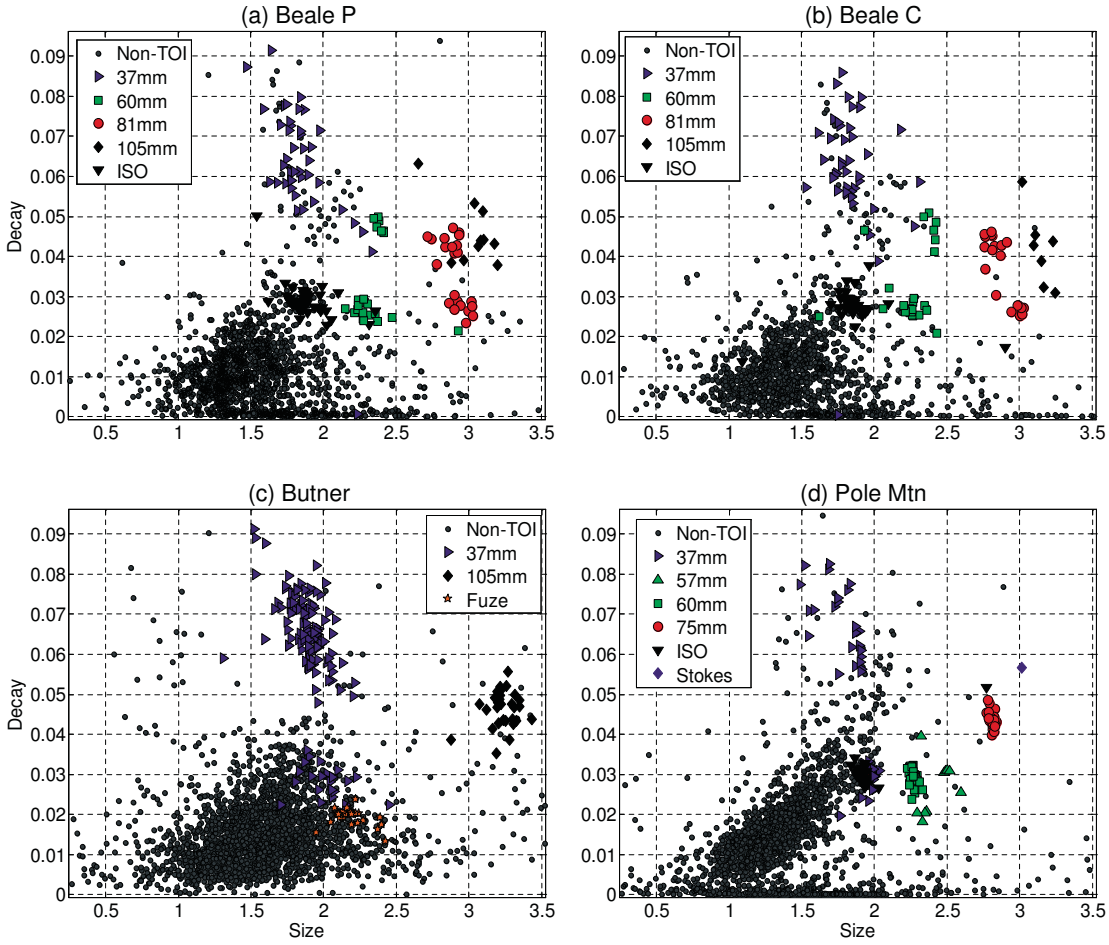

Figure 2: Estimated MetalMapper size/decay features for ESTCP demonstration data sets. Displayed variables are dimensionless.

DEFINING THE TRAINING DATA

Successful classification with rule-based or statistical algorithms depends upon a training data set that is a representative sample of the (unlabeled) test data. Once data have been acquired and inverted, estimated features for all targets must be carefully inspected and selected items labeled (dug) to identify novel UXO types that have not yet been encountered in the ground truth, or to identify outliers to known UXO classes. Liu et al. (2008) take an information-theoretic approach to this problem: they iteratively label targets to reduce the overall uncertainty in the parameters of their classifier.

We use an intuitive approach to build the training data set. During quality control of data fits, we carry out a "supervised" analysis by manually identifying targets that closely correspond to known TOI polarizabilities. We then define polygonal regions of interest in size/decay feature space, as shown in figure 3. Within each region of interest we carry out a cluster analysis of the test data polarizabilities as follows:

(a) We compute a (symmetric) misfit matrix $\mathbf{M}$ with elements

$$M_{jk} = \sum_{i=1}^{N} \Big(\log(L^j(i)) - \log(L^k(i)) \Big)^2 , \tag{5}$$

with $L^j(i)$ the polarizability for the jth target at the ith time channel. For each test item we therefore compute the misfit of its log-transformed polarizabilities with all other test items. The misfit can be computed over all polarizabilities, or with the total polarizability.

(b) We identify clusters of targets with self-similar polarizabilities. Our criteria for defining a cluster is a set of at least $N_{cluster}$ (usually ≥ 3) targets for which the maximum mutual misfit is less than a specified threshold. The misfit threshold acts as a regularization parameter: a lower threshold specifies fewer clusters with fewer members, but with greater self-similarity of the members

(c) We merge clusters from the unsupervised analysis with targets identified by the supervised analysis: if any target in a cluster was manually identified as a TOI, then all targets in that cluster are considered TOI.

(d) Finally, we request ground truth for selected targets within each cluster. For clusters which are not associated with known TOI, we request a small number (~ 3) of representative targets, e.g. defined by the smallest mutual misfits within the cluster. In the case of clusters associated with known TOI, our aim is to identify the maximum extent of the cluster in polarizability space. This queries the region of feature space corresponding to the greatest overlap between TOI and non-TOI and guards against outlying TOI that may appear similar to clutter.

FEATURE SELECTION

The choice of classification features is dictated by the quality of the recovered polarizabilities. As illustrated in figure 4a, in the ideal case there is a close match between the estimated

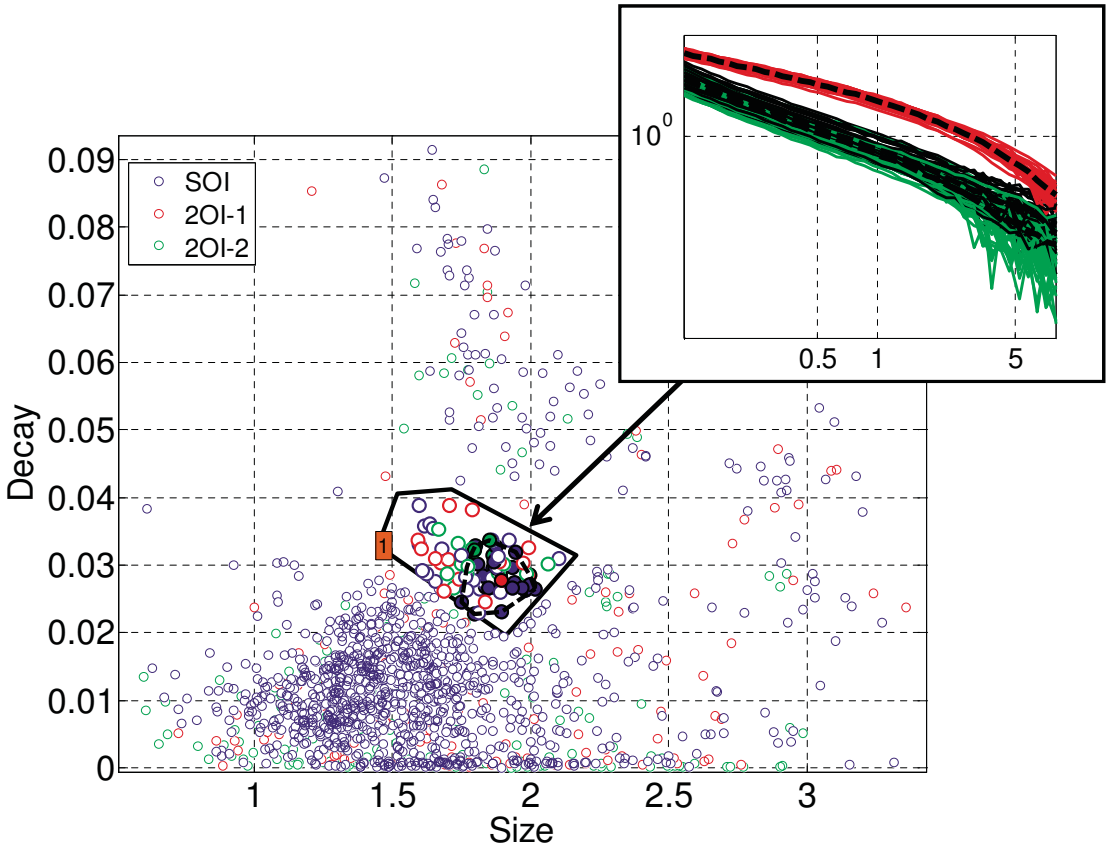

Figure 3: Clustering Beale P features to identify TOI. Feature vectors within a user-defined polygon (solid black) are clustered based upon their polarizability misfit (equation 5). Vectors within a pre-defined misfit threshold of their closest neighbor are assigned to the cluster and are displayed with a solid color in the size-decay space, with a black dashed line defining the extent of the cluster. Inset plot shows corresponding polarizability features for clustered targets, with the dashed line median polarizabilities of the cluster members. SOI and 2OI denote vectors from single and two-object inversions, respectively.

polarizabilities for a UXO and the library polarizabilities for that item's class. This is the usual situation for the majority ($\sim$ 95%) of UXO encountered in ESTCP demonstration data sets. When a multi-static sensor is properly centered over an isolated target, near perfect recovery of polarizabilities is expected.

In more challenging scenarios however, some of the estimated polarizabilities can deviate from the expected, reference values, as shown in 4b. The secondary and tertiary polarizabilities, in particular, are sometimes poorly constrained. This is because these parameters are sensitive to low SNR data that may arise, for example, when the sensor is poorly positioned, the target is near its maximum detectable depth, or an incorrect background correction is used in processing. In addition, background geologic response or overlapping target signatures that are not properly accounted for in the inversion can act as significant noise sources. If the SNR remains sufficiently high, we may still be able to recover a reli-

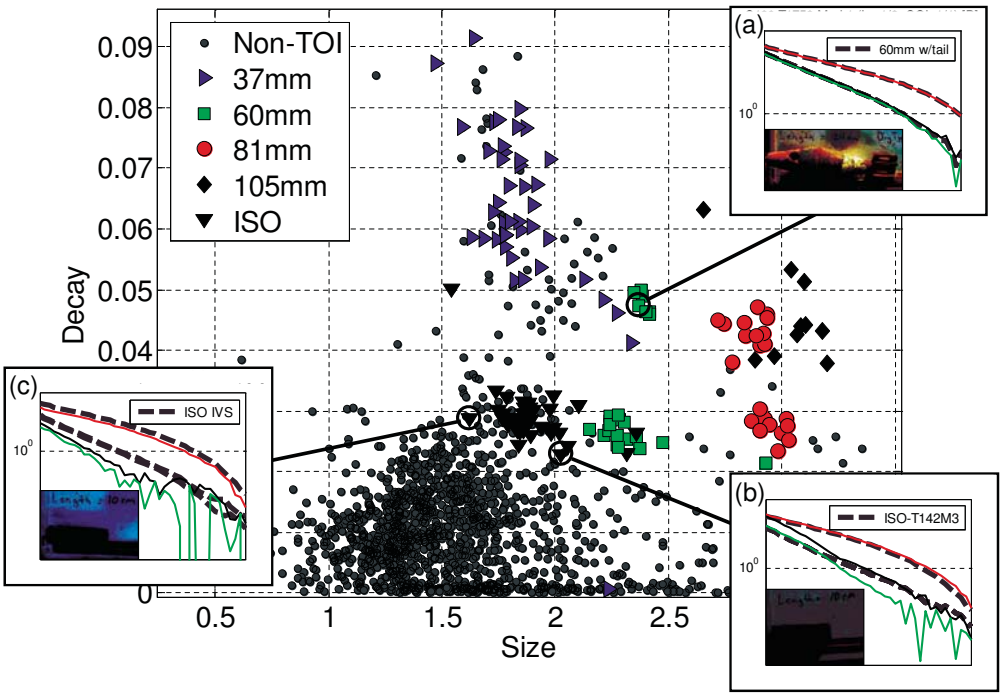

Figure 4: Example polarizability estimates for three targets (a-c) from the Beale P data set. Insets show polarizability estimates (solid lines), reference polarizabilities (dashed lines), and ground truth photos corresponding to indicated size/decay features.

able primary, or total, polarizability, as in b. In the worst case (figure 4c), all estimated polarizabilities will be poorly constrained and a classification strategy that relies solely on polarizability matching may fail to find these difficult UXO. The simplest representation in size/decay space may help to identify these outliers sooner than a strategy that relies on polarizabilities throughout classification. We also remark that a rule-based approach that prioritizes larger, slow-decaying items (on the basis of size/decay parameters) may identify novel UXO that are not in our polarizability library (e.g. the Stokes mortar in the Pole Mountain data set, figure 2d)

Figure 5 compares receiver operating characteristics (ROCs) for rule-based classifiers trained on the following features:

(a) L123: library matching using all polarizabilities

(b) L1: library matching using primary polarizability

(c) Ltot: library matching using total polarizability

(d) Size/decay: threshold on linear combination of size/decay features.

Within each data set all classifiers used the same set of labeled targets, generated via the clustering procedure outlined in the previous section.

We remark that overall data and model quality metrics in table 1 are generally predictive of classification performance. In the best case (Pole Mountain), excellent performance is obtained using all feature sets. The optimal performance at Pole Mountain is obtained using a classifier that uses all polarizabilities. However, for mediocre data sets (Beale P and Butner) classifying with all polarizabilities produces good initial performance but later has difficulty finding targets with poorly constrained L_2 and L_3. This results in a high false alarm rate. More conservative feature sets (i.e. size/decay, L1) produce much lower false alarm rates for these data sets. Finally, for the most challenging data set (Beale C) the size/decay and L1 features still provide an improvement over using all polarizabilities, but no objective classification strategy can find the outlying UXO in this case.

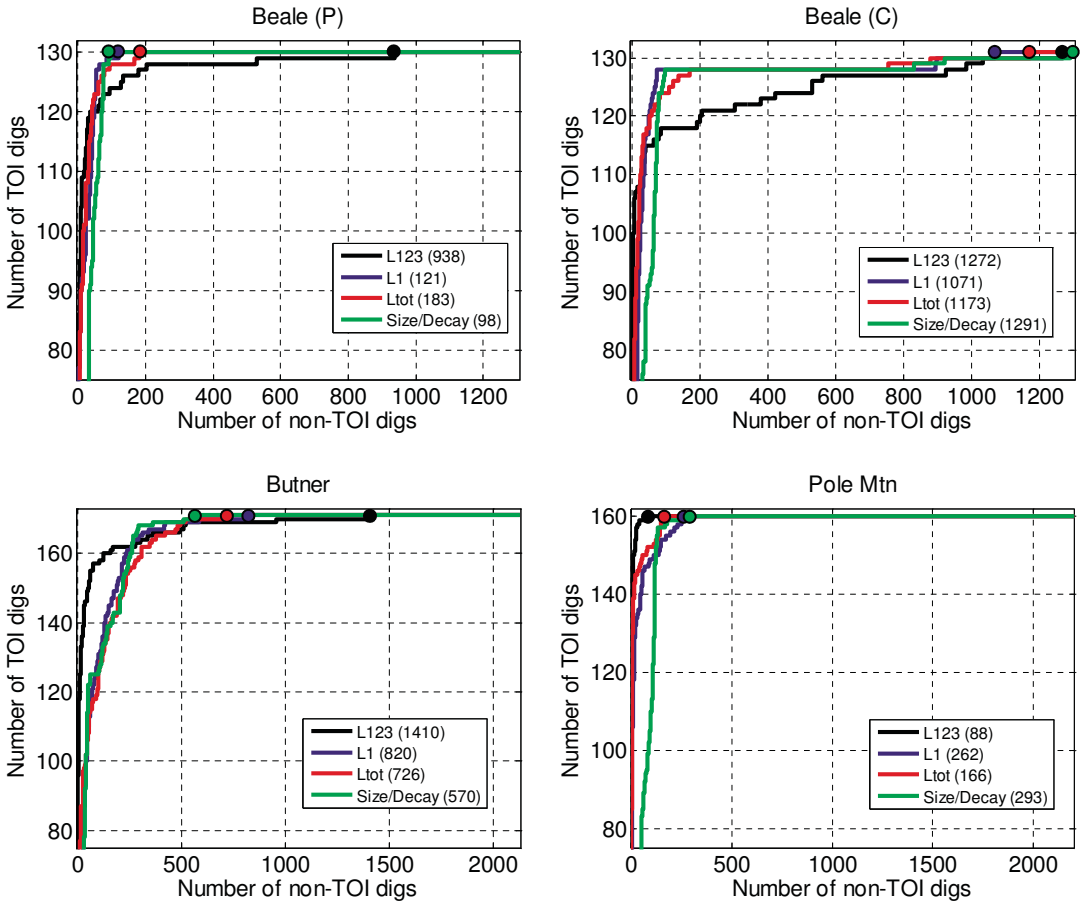

Figure 5: Receiver operating characteristics for classification strategies applied to ESTCP MetalMapper data sets. Markers indicate the point on each ROC at which all UXO are found. Bracketed numbers in legends indicate the required number of non-TOI digs for each method.

The variable quality of polarizability features within a given data set suggests a classification strategy that adapts features as digging proceeds. Figure 6 shows one possible approach: we initially dig using all polarizabilities and then switch to a more conservative

feature set - in this case L_{total}. The point at which to switch can be identified on a plot of the sorted decision statistic. In this context the decision statistic is based on the minimum misfit of the estimated polarizabilities with library polarizabilities. Analogous to a Tikhonov curve (Oldenburg and Li, 2005), we select the point on the (normalized) decision statistic curve closest to the origin as the point to switch between feature sets. This produces an ROC intermediate to classification with the individual feature sets: with the two-stage classifier we get good initial performance using all polarizabilities and the same false alarm rate as when we use L_{total} throughout.

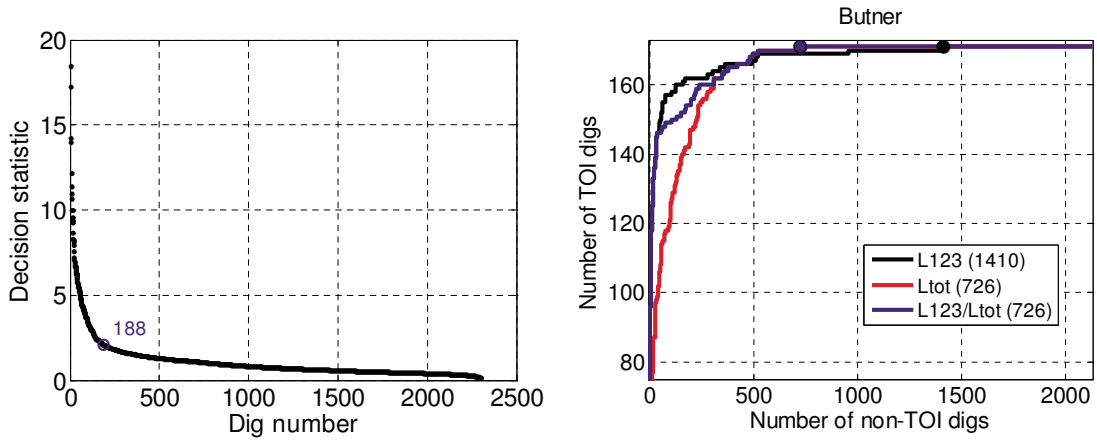

Figure 6: Two-stage classification. Left: plot of the sorted decision statistic for first stage (all polarizabilities) classifier. Blue circle indicates automatically-selected point at which we switch to classification with total polarizabilities. Right: comparison of ROCs for classifiers applied to Butner data set. Two stage classifier is denoted L123/Ltot. Two stage classifier and classifier trained on total polarizability only (Ltot) achieve the same false alarm rate.

CONCLUSIONS

While data from multi-static, multi-component TEM sensors such as the MetalMapper generally support reliable classification, care is still required in the analysis of each data set. As exemplified by the the Beale C and P data sets, different operators using the same sensor at the same site can strongly affect data quality. The challenge for the data analyst is then to recognize problems with the data and adapt the classification strategy accordingly.

When requesting training data, we use a combination of manual identification of likely TOI during quality control and user-guided clustering to determine the extents of the distributions of TOI and to identify novel target classes. This has produced good performance on the demonstration data sets considered here. This approach may fail if there are small, unique targets of interest (e.g. fuze components) hidden within the clutter "cloud" in feature space. Developing objective and reliable criteria to find these items is an ongoing research challenge.

Practical experience with ESTCP demonstration data sets has shown that feature selection is critical to successful classification. While information is lost when the feature space is reduced to the primary (or total) polarizability or size/decay features, these parameters retain sufficient information to produce good classification performance while preventing

outlying TOI from occurring late in the dig list.

ACKNOWLEDGEMENTS

This work was funded by Strategic Environmental Research and Development Program (SERDP) projects MR-1629 and MR-1657, and ESTCP project MR-1004.

REFERENCES

Bell, T., 2006, Adaptive and iterative processing techniques for overlapping signatures: Technical summary report, ESTCP project MM-200415: Technical report, ESTCP.

Bell, T., B. Barrow, and J. T. Miller, 2001, Subsurface discrimination using electromagnetic induction sensors: IEEE Trans. Geosci. Remote Sensing, **39**, 1286–1293.

Benavides, A., M. Everett, and C. Pierce, 2009, Unexploded ordnance discrimination using time-domain electromagnetic induction and self-organizing maps: Stochastic Environmental Research and Risk Assessment, **23**, no. 2, 169–179.

Billings, S., 2011, Next generation data collection system for one-pass detection and discrimination, ESTCP Project MR-200908: Technical report, ESTCP.

Billings, S. D., L. R. Pasion, L. Beran, N. Lhomme, L. Song, D. W. Oldenburg, K. Kingdon, D. Sinex, and J. Jacobson, 2010, Unexploded ordnance discrimination using magnetic and electromagnetic sensors: Case study from a former military site: Geophysics, **75**, B103–B114.

Gasperikova, E., V. Vytla, L. Kennedy, T. Jobe, and X. Zhu, 2011, Cued survey with a handheld UXO discriminator at Camp Beale, CA: Presented at the Partners in Environmental Technology Technical Symposium and Workshop, Washington D.C.

Lee, W. H., P. D. Gader, and J. N. Wilson, 2007, Optimizing the area under a receiver operating characteristic curve with application to landmine detection: IEEE Trans. Geosci. Remote Sensing, **45**, 389–397.

Lhomme, N., 2012, Man-Portable Vector EMI Sensor for Full UXO Characterization, ESTCP Project MR-201005: Technical report, ESTCP.

Liu, Q., X. Liao, and L. Carin, 2008, Detection of unexploded ordnance via efficient semi-supervised and active learning: IEEE Trans. Geosci. Remote Sensing, **46**, 2558–2567.

Oldenburg, D., and Y. Li, 2005, Inversion for applied geophysics: A tutorial, *in* Investigations in Geophysics No.13: Near-surface: Society of Exploration Geophysics, 89–150.

Pasion, L. R., 2007, Inversion of time-domain electromagnetic data for the detection of unexploded ordnance: PhD thesis, University of British Columbia.

Pasion, L. R., B. C. Zelt, K. A. Kingdon, and L. S. Beran, 2012, Feature Extraction and Classification of EMI Data, Camp Beale, CA, ESTCP Project MR-201004: Technical report, ESTCP.

Prouty, M., D. C. George, and D. D. Snyder, 2011, MetalMapper: A Multi-Sensor TEM System for UXO Detection and Classification, ESTCP Project MR-200603: Technical report, ESTCP.

Shubitidze, F., B. Barrowes, I. Shamatava, J. P. Fernandez, and K. O'Neill, 2011, The orthonormalized volume magnetic source technique applied to live-site UXO data: Inversion and classification studies: SEG Technical Program Expanded Abstracts, **30**, 3766–3770.

Song, L.-P., D. W. Oldenburg, and L. R. Pasion, 2012, Estimating source locations of

unexploded ordnance using the multiple signal classification algorithm: Geophysics, **77**, WB127–WB135.

Song, L. P., L. R. Pasion, S. D. Billings, and D. W. Oldenburg, 2011, Nonlinear inversion for multiple objects in transient electromagnetic induction sensing of unexploded ordnance: Technique and applications: IEEE Trans. Geosci. Remote Sensing, **49**, 4007 –4020.

Steinhurst, D. A., G. R. Harbaugh, J. B. Kingdon, T. Furuya, D. A. Keiswetter, and D. C. George, 2010, EMI Array for Cued UXO Discrimination, ESTCP Project MM-0601: Technical report, ESTCP.

Zhang, B., K. ONeill, J. Kong, and T. Grzegorczyk, 2008, Support vector machine and neural network classification of metallic objects using coefficients of the spheroidal MQS response modes: IEEE Trans. Geosci. Remote Sensing, **46**, 159–171.